Nanoscale Mechanisms of Hydrogen Segregation and Diffusion in Metals

by

Xiao Zhou

Department of Mining and Materials Engineering

McGill University, Montréal

April 2018

A thesis submitted to McGill University in partial fulfillment of the requirements of the degree of Doctor of Philosophy

To my Wife- Ruirui Liu and my Family

Abstract

Hydrogen embrittlement (HE), a phenomenon known as hydrogen deteriorating mechanical properties of structural metals to cause premature failure, continues to haunt the industry in the design and application of structural metals since its first discovery more than one century ago. Despite continuous research effort on HE, there remains no consensus on the exact mechanism underlying the occurrence of HE. However, it is widely recognized that HE is microstructure-sensitive, namely microstructural heterogeneities play a vital role in determining the material's susceptibility to HE. This thesis represents a body of research studies dedicated to understanding the key mechanistic aspects underlying the interplay between microstructures and hydrogen in structural metals, in order to provide insights towards developing effective microstructure engineering routes to moderate or prevent HE. Focusing on two main categories of microstructural entities in structural metals, dislocations and grain boundaries, the thesis systematically investigated the interactions between hydrogen and microstructures at the atomic scale, employing comprehensive molecular dynamics simulations, first principles calculations and Kinetic Monte Carlo simulations. The simulation results were then interpreted in the framework of continuum mechanics to develop physics-based predictive models to reveal the structure-property relationships underlying energetics and kinetic behaviors of hydrogen at dislocations and grain boundaries.

This thesis is in the manuscript-based format, composed of four articles shown in Chapter 4-7, including predictive assessments of hydrogen energetics and segregation at grain boundaries

(Chapter 4), quantifications of the dual role of grain boundaries in hydrogen diffusion behaviors (Chapter 5), clarification of the effects of hydrogen on dislocation nucleation under nanoindentation (Chapter 6) and clarification of hydrogen short-circuit and pipe diffusion at dislocations (Chapter 7). In particular, Chapter 4 determined the energy spectrum of hydrogen staying at different examined grain boundaries. Chapter 5 examined the kinetics of hydrogen at grain boundaries. Chapter 6 quantified the role of hydrogen on dislocation nucleation and Chapter 7 studied the hydrogen trapping and diffusion at dislocations.

Résumé

Depuis la découverte par William Johnson il y a un siècle de l'effet néfaste de l'hydrogène sur la détérioration des propriétés mécaniques des matériaux, appelée la fragilisation par l'hydrogène, ce sujet conserve un intérêt continu depuis de nombreuses années. Malgré la recherche constante dans ce domaine, l'interprétation et les mécanismes responsables de la fragilisation de l'hydrogène sont loin d'être acceptés. Par contre, il est bien connu que la microstructure est sensible à la fragilisation de l'hydrogène et que les hétérogénéités microstructurales jouent un rôle essentiel afin de déterminer la susceptibilité de ce phénomène. Plus particulièrement, les dislocations et les joints de grain sont les hétérogénéités les plus fréquentes parmi les métaux et les alliages. L'interaction entre l'hydrogène et les dislocations (ou les joints de grain) est considéré comme étant un aspect extrêmement important affectant la rupture prématurée induite par l'hydrogène dans les métaux.

Afin de mieux comprendre l'origine et les mécanismes reliés à la fragilisation de l'hydrogène, les interactions entre l'hydrogène et les défauts à l'échelle atomique furent investigués systématiquement dans cette thèse, en focussant principalement sur les limites de gain et les dislocations dans les métaux. Plus spécifiquement, l'énergie et la cinétique de l'hydrogène dans les joints de grains et les dislocations furent entièrement examinés par des simulations de dynamique moléculaire, des calculs utilisant le premier principe et des simulations cinétiques de Monte Carlo (Kinetic Monte Carlo). De plus, des modèles mécaniques

ont été proposés dans le but d’évaluer l’énergie et la cinétique de l’hydrogène dans les joints de grain et les dislocations.

Cette thèse est présentée sous forme de manuscrit composé de quatre articles introduits dans les chapitres 4 à 7. Dans le chapitre 4, le spectre d’énergie de l’hydrogène demeurant à différents joints de grains examinés fut déterminé. Le chapitre 5 s’intéresse à la cinétique de l’hydrogène aux joints de grains. Dans le chapitre 6, le rôle de l’hydrogène sur la nucléation des dislocations est expliqué, et le chapitre 7 traite sur le piégeage et la diffusion de l’hydrogène dans les dislocations. Ces articles ont non seulement fourni une compréhension de l’énergie et de la cinétique de l’hydrogène dans les hétérogénéités microstructurales, mais ont également approfondi la compréhension mécanistique de la fragilisation de l’hydrogène.

Acknowledgements

This doctoral thesis would not be successfully accomplished without the encouragement and support from many people. I am so fortunate to have many people who have given the contributions to my research work in their own particular way.

First of all, I would like to convey my sincerest gratitude to my advisor, Professor Jun Song who has provided the invaluable space and freedom during my journey of doctoral study. His unremitting support and encouragement stimulated me to continually innovate in my research. Most importantly, his passion and scientific gratitude taught me how to become a real scientist, which is the valuable treasure in my lifetime.

I would like to thank my important coauthors, Professor Ting Zhu and Professor David McDowell at Georgia Institute of Technology, Professor William Curtin at École Polytechnique Fédérale de Lausanne and Professor Normand Mousseau at Université de Montréal for their important suggestions and critical comments to my research work.

I would also like to acknowledge my group members for their help in my research. Special thank goes to Mr. Daniel Marchand and Mr. Bin Ouyang who have assisted me a lot during the initial stage of my research work.

I would like to thank the financial support from Natural Science and Engineering Research Council (NSERC), McGill Engineering Doctoral Award (MEDA) and China Scholarship Council (CSC). I also acknowledge the computing power from Supercomputer Consortium Laval and McGill High Performing Center.

Last but not least, I am indebted to my parents for their unconditional support during these years. Special and earnest thanks go to my wife, Ruirui Liu for her endless support and love, for her understanding and patience, and for looking after our beloved son Kenneth who is always my source of pride.

Preface and Contributions of Authors

This thesis is manuscript-based format and four research articles shown in Chapter4-7 are listed below (* stands for corresponding author):

1. **Chemomechanical origin of hydrogen trapping at grain boundaries in FCC metals**, Xiao Zhou, Daniel Marchand, David L. McDowell, Ting Zhu, and Jun Song*, *Physical Reviews Letters* 2016; 116(7): 075502.

2. **The role of grain boundaries in hydrogen diffusion: atomistic origin and mechanistic modeling**, Xiao Zhou, W.A. Curtin, Jun Song*, to be submitted.

3. **Atomistic investigation of the influence of hydrogen on dislocation nucleation during nanoindentation in Ni and Pd**, Xiao Zhou, Bin Ouyang, W.A. Curtin, Jun Song*, *Acta Materialia* 2016; 116: 364-369.

4. **Atomistic investigation of hydrogen diffusion at dislocations in structural metals**, Xiao Zhou, Normand Mousseau, W.A. Curtin, Jun Song*, to be submitted.

Author contributions: For all listed articles, XZ and JS developed the idea; XZ carried out all simulations, mechanistic model construction and data collection with the guidance of JS. XZ prepared the manuscript and discussed with JS. For article 1, DM helped the model construction, DM and TZ discussed the results and edited the manuscript. For article 2, WC discussed the results. For article 3, BO helped the model construction, WC discussed the results. For article 4, NM helped the simulation setup and discussed the results, WC discussed the results.

Table of Contents

List of Figures

List of Tables

Chapter 1: Introduction

Nowadays, the global energy crisis and the striking risk of climate change resulted from the emission of greenhouse gas due to the use of fossil fuels are becoming increasingly critical problems for humankind, which are calling for new technologies to provide solutions. Among various approaches to tackle the above global challenge, two effective routes are (*i*) innovation in high-strength materials and (*ii*) alternative energy sources. Regarding the first route, high-strength metals and alloys are direct path towards achieving high energy efficiency. However, high-strength metals and alloys, prevailing used as load-carrying components, can be greatly affected by their service environment to suffer mechanical degradation, rendering their reliability questionable. Among different types of degradation, one of them is the loss of ductility and brittle fracture caused by hydrogen, known as hydrogen embrittlement (HE) [1], which significantly hinders the design and development of high-strength metals. For the second route, hydrogen has been considered as a promising alternative energy source for the fossil fuels given its abundance in the universe and capability to avoid greenhouse gases emission [2]. However, extensive usage of hydrogen as a fuel faces many bottlenecks such as complicatedness of storage and distribution [3]. In particular, the afore-mentioned problem of HE remains to be a concern when it comes to the hydrogen delivery infrastructure (largely being constructed from structural metals) under aggressive hydrogen service conditions because of the risk of catastrophic premature failures induced by hydrogen.

The HE phenomenon, a long-standing industrial headache, despite enormous research efforts on it for over one century [1, 4-8], remains largely a myth to-date. Despite numerous proposed models, the precise mechanism(s) of hydrogen embrittlement remains elusive, rendering accurate quantitative predictions of HE impossible. One key factor underlying hydrogen embrittlement resides in the interplay between hydrogen and microstructural heterogeneities, such as vacancies, dislocations and grain boundaries in materials. However, this interaction is not fully understood at the atomic-level due to the difficulty of experimental observation of H atoms on such a small scale [9]. Nonetheless, with the rocketing development of computing capacity and power, atomistic simulations provide a feasible way to study hydrogen-microstructure interactions at the atomic scale, enabling the direct probing of the fundamental physical origin and mechanisms behind HE [10].

In this thesis, we employ state-of-the-art computational tools to investigate the interaction of hydrogen with two major microstructural heterogeneities (namely, grain boundaries and dislocations) in metals, with particular focus on the atomistic mechanisms of microstructure-mediated hydrogen trapping and diffusion. The main objectives of this thesis are as follows:

A. Develop an efficient algorithm to accurately characterize grain boundaries and identify interstitial sites for hydrogen adsorption therein;

B. Evaluate hydrogen energetics at grain boundaries and develop chemomechanical model to predictively assess hydrogen segregation at grain boundaries;

C. Investigate hydrogen kinetics at grain boundaries and develop micromechanical model to predictively assess hydrogen diffusion behaviors at grain boundaries;

D. Examine the effects of hydrogen on dislocation nucleation in nanoindentation;

E. Study and clarify hydrogen short-circuit and pipe diffusion at dislocations;

The results obtained from the aforementioned objectives are presented in Chapters 4-7 in detail. Chapter 4 proposed a novel method based on space tessellation that permits robust characterization of local atomic structures and accurate identification of hydrogen adsorption sites at grain boundaries. Then, this space tessellation method, in combination with first-principles calculations, enables efficient analysis of hydrogen segregation at grain boundaries. Finally, one chemomechanical model was developed to predictively evaluate hydrogen adsorption energies at grain boundaries. Chapter 5 systematically studied hydrogen kinetics at grain boundaries using first principles calculations and Kinetics Monte Carlo simulations. The dual role of grain boundaries in hydrogen kinetics (i.e., fast diffusion and trapping) was identified, attributed to local atomic configurations of grain boundaries. One micromechanical model was proposed to quantify the distinct diffusion behaviors and the transition in hydrogen diffusion. Chapter 6 examined the effects of hydrogen on dislocation nucleation during plastic response in nanoindentation. It was found the threshold load regarding the onset of plasticity (reflected by pop-in load in nanoindentation) can be reduced by hydrogen, which stems from the local dilation resulted from hydrogen. Chapter 7 quantified hydrogen energetics and kinetics at dislocations. Short-circuit and pipe diffusion were also clarified by Kinetic Monte Carlo simulations over long timescales.

1.1 References

[1] Johnson WH. On Some Remarkable Changes Produced in Iron and Steel by the Action of Hydrogen and Acids Proceedings of the Royal Society of London 1874;23:12.
[2] Abas N, Kalair A, Khan N. Review of fossil fuels and future energy technologies. Futures 2015;69:31-49.
[3] Gupta R, Basile A, Veziroglu TN. Compendium of Hydrogen Energy: Hydrogen Storage, Distribution and Infrastructure: Woodhead Publishing; 2016.
[4] Hobson JDH, J. the effect of hydrogen on the tensile proerties of steel. Journal of Iron Steel Institute 1953;173:9.
[5] Oriani RA. A mechanistic theory of hydrogen embrittlement of steels. Berichte der Bunsengesellschaft für physikalische Chemie 1972;76:848-57.
[6] Gangloff RP, Wei RP. Gaseous hydrogen embrittlement of high strength steels. MTA 1977;8:1043-53.
[7] Oriani RA. Hydrogen Embrittlement of Steels. Annual review of materials research 1978;8:30.
[8] Lynch SP. A fractographic study of gaseous hydrogen embrittlement and liquid-metal embrittlement in a tempered-martensitic steel. Acta Metallurgica 1984;32:79-90.
[9] Koyama M, Rohwerder M, Tasan CC, Bashir A, Akiyama E, Takai K, et al. Recent progress in microstructural hydrogen mapping in steels: quantification, kinetic analysis, and multi-scale characterisation. Materials Science and Technology 2017;33:1481-96.
[10] Völkl J, Alefeld G. Diffusion of hydrogen in metals. Hydrogen in metals I: Springer; 1978. p. 321-48.

Chapter 2: Literature Review

This chapter provides an overview of important experimental, theoretical and simulation studies focusing on the microstructural aspects of hydrogen embrittlement (HE) in metals and alloys. The current state of research progress and scientific challenges in understanding HE are discussed within this section. The contents of this chapter are organized as follows: First, the ingress of hydrogen into metals is described. Then, important experimental and atomistic studies pertaining to hydrogen-microstructure interactions are reviewed. Finally, the related mechanisms proposed to explain the experimental observations are described and discussed.

2.1 Ingress of hydrogen into metals

The step prior to the occurrence of HE is apparently the presence of hydrogen and its entrance into metals. This procedure is intricate because it can be affected by various external factors. In general, hydrogen may come from the gaseous and aqueous media surrounding metals. With respect to gaseous media, hydrogen ingress takes place predominantly via two main processes: physisorption, chemisorption followed by absorption [1]. During the physisorption process, when hydrogen gaseous phase approaches the metal surface, hydrogen will be attached to the surface to form buffer gaseous layers due to van der Waals forces. In the chemisorption process, hydrogen molecules react with metal atoms at the surface within the surface monolayer, this step is slow but driven by the chemical short-range force between hydrogen molecules and metal atoms that is drastically stronger than the van der Waals force in the physisorption step.

Finally, absorption occurs and the hydrogen molecule will be dissociated into individual hydrogen atoms [2, 3], which then will diffuse into the bulk metal lattice.

On the other hand, there exist many electrochemical processes that can introduce hydrogen in aqueous media. For instance, during the surface cleaning process of steel and metallic alloys, the use of strong acids, alkaline and saline solutions may lead to pronounced introduction of aqueous hydrogen and subsequent ingress of hydrogen into bulk metallic structure. Unlike hydrogen from the gaseous phase, hydrogen in aqueous media mainly comes from hydrogen evolution reactions. The reactions can have different forms depending on the pH condition:

$$2\,H_3O^+ + 2\,e^- \rightarrow H_2 + 2\,H_2O \tag{2.1}$$

$$2\,H_2O + 2\,e^- \rightarrow H_2 + 2\,OH^- \tag{2.2}$$

where Eq. 2.1 and 2.2 are typical hydrogen evolution reactions for acid and alkaline solutions respectively [4, 5]. However, even a simple hydrogen evolution reaction may also contain many successive steps [6, 7] as shown in Figure 2.1. For example, in acidic condition, hydrated protons (i.e., H_3O^+) will combine with one electron at the metal surface to generate water molecules and adsorbed hydrogen:

$$H_3O^+ + e^- \rightarrow H_{ads} + H_2O \tag{2.3}$$

while in alkaline solutions, water molecule will get one electron to form adsorbed hydrogen:

$$H_2O + e^- \rightarrow H_{ads} + OH^- \tag{2.4}$$

Once adsorbed hydrogen atoms are produced by means of Eq. 2.3 or 2.4, they can recombine together to form hydrogen molecules or be absorbed as atomic hydrogen into the metal:

$$H_{ads} + H_{ads} \rightarrow H_2 \tag{2.5}$$

$$H_{ads} \rightarrow H_{abs} \tag{2.6}$$

The competition between hydrogen recombination and absorption is largely determined by the occupation of adsorbed hydrogen on the metal surface. A hydrogen-saturated metal surface would favor the recombination while otherwise the adsorbed hydrogen would transform to absorbed hydrogen to get into the metal matrix [8].

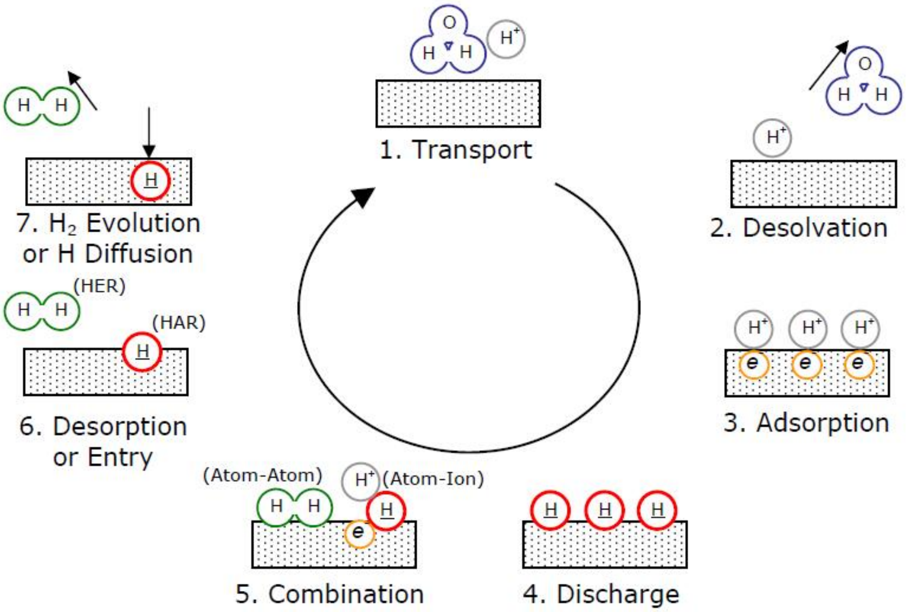

Figure 2.1. Schematic illustration of the hydrogen evolution reaction with multiple successive steps [8]. [Figure adapted with permissions]

Due to the significance of hydrogen entrance to HE, many strategies were proposed so as to attenuate hydrogen ingress and prevent structural metals from hydrogen attack. One of the most common and effective way is sacrificial metallic coatings. Many studies have proved that sacrificial metallic coatings such as Zn, Cd and Zn-Ni, can not only alleviate HE, but also can effectively suppress wear corrosion and tribocorrosion [9, 10].

2.2 Interactions between hydrogen and microstructures in metals

Following the absorption, hydrogen can quickly diffuse into the metal matrix. For most structural metals, the lattice solubility of hydrogen is low. However, in the vicinity of multifarious microstructural heterogeneities, the interaction between hydrogen and metal is much stronger than that in the bulk lattice. As a result, hydrogen can collect there. Typical microstructural heterogeneities in metals include vacancies, dislocations, grain boundaries, precipitates. A myriad of experimental studies revealed that HE in metals is strongly microstructure-sensitive. In sections below, the interactions between hydrogen and different types of microstructures are described within the context of key experiments and atomistic simulations, and the relevance of those interactions to HE is discussed.

2.2.1 Vacancies

Vacancy is one of the most common structural defects in metals. Although its concentration in metals under thermal equilibrium at room temperature is extremely low, the pioneering experimental studies performed by Fukai et al. [11-15] discovered incredibly high vacancy concentration in metals under high hydrogen pressures (see Figure 2.2a) which may subsequently cause void formation. The formation of excessive vacancies is named as superabundant vacancy (SAV) formation. However, Fukai et al’s work cannot provide further clarification for better understanding of hydrogen-related failure in metals. One important requirement to achieve such understanding is the rational analysis of fracture morphologies that often show apparent plasticity. Nagumo et al. [16, 17] later utilized hydrogen as tracer element to detect microstructure evolution under plastic deformation to analyze the fracture process. They observed significant increase in the density of point-like defect during deformation due to strong hydrogen trapping at vacancy clusters, as reflected by the desorption profile (see Figure 2.2b). They demonstrated that there exist a correlation between ductile crack propagation and the density of point defects created (see Figure 2.2c) with fractographic features of hydrogen-related cracking showing a dimple pattern. Based on the above study, a subsequent work by Takai et al. [18] made a couple of conclusions regarding the role of vacancy: (*i*) hydrogen-related degradation can occur without hydrogen involvement in the final stage of crack process (see Figure 2.2d); (*ii*) the hydrogen absorption profile under plastic deformation suggests that hydrogen facilitates the formation of strain-induced vacancies (see Figure 2.3), providing direct experimental evidence to hydrogen-enhanced superabundant vacancy model. A more recent study carried out by Li et al. [19] discovered the existence of nanovoids along the cleavage plane under hydrogen-containing environment (see Figure 2.4). Based on this, it was postulated that assisted by hydrogen, vacancy clusters can agglomerate in front of the crack tip and along (grain boundary) cleavage planes.

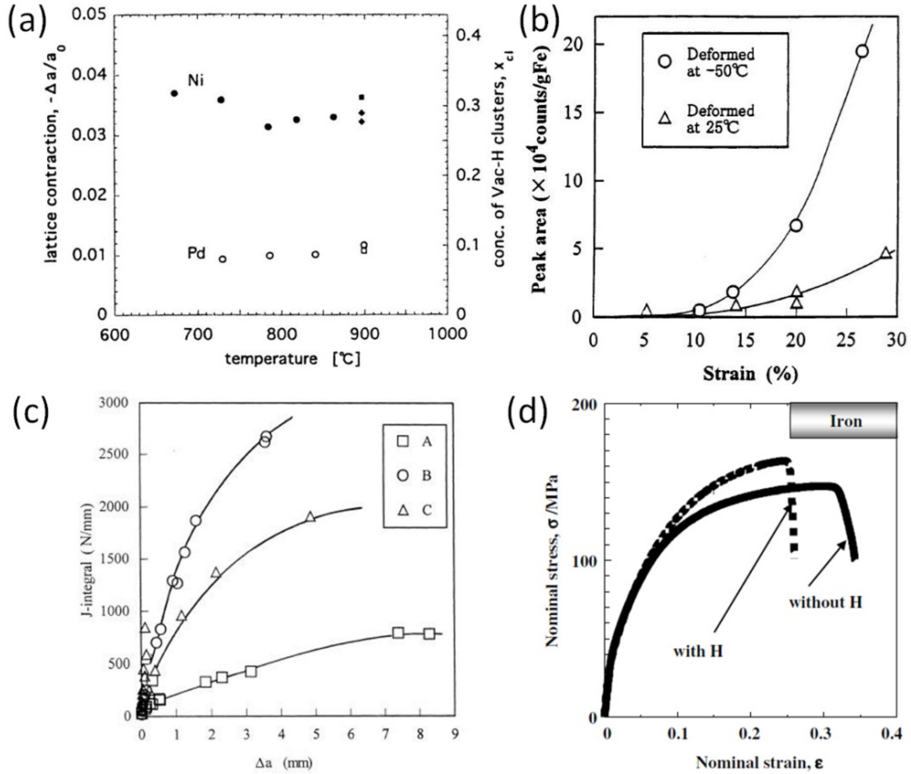

Figure 2.2. (a) Lattice concentration for Ni and Pd (left axis) and vacancy hydrogen cluster concentration for Ni and Pd (right axis) at different temperatures [11]. (b) Hydrogen absorption concentration as a function of plastic strain at different temperatures [17]. (c) J integral values as a function of ductile crack growth for three different steels (i.e., A,B,C) [16]. (d) Stress-strain curves for iron with and without hydrogen charging [18]. [Figure adapted with permissions]

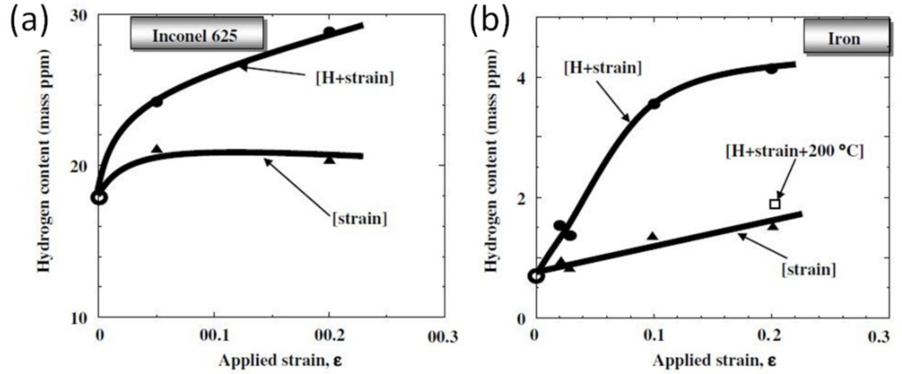

Figure 2.3. Hydrogen absorption content as a function of applied strain in the presence and absence of hydrogen [18]. (a) Inconel 625 alloy and (b) Iron. [Figure adapted with permissions]

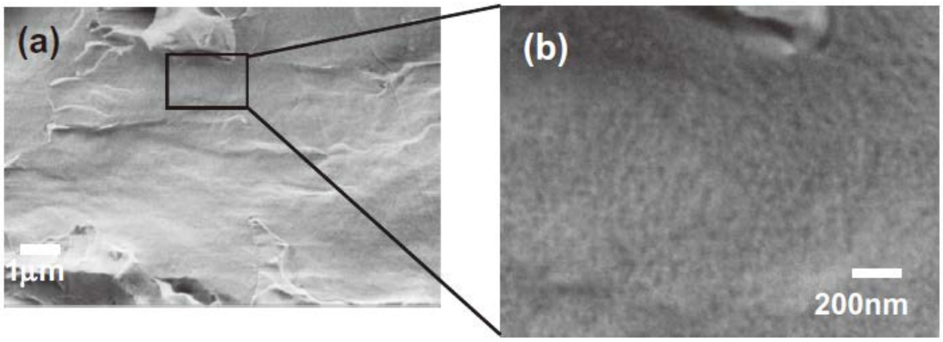

Figure 2.4. (a) Quasi-brittle fracture of X60 CT sample tested in the presence of hydrogen. (b) Magnified region indicated in (a). The black spots indicate the nanoscale dimples on quasi-brittle cleavage plane [19]. [Figure adapted with permissions]

Aside from the aforementioned key experimental findings, the interplays of hydrogen with vacancies have also been intensively investigated by means of atomistic simulations [20-26]. These fruitful studies revealed that hydrogen can be strongly trapped and segregated in the vacancy. For example, Yoshitaka et al. [27] and Hayward et al. [23, 28] carried out *ab initio* calculations and molecular dynamics simulations, confirming that maximum 6 hydrogen atoms prefer to stay in monovacancy in bcc Fe, as shown in Figure 2.5a. Recent simulation studies [29-31] suggested monovacancy in fcc Ni having similar trend to bcc Fe where up to 6 hydrogen atoms are stabilized in monovacancy. In addition, the results from Lu et al. [24] demonstrated hydrogen molecule (i.e., H_2) is stable in monovacancy fcc Al. Liu et al. [32] also noted that multiple hydrogen atoms are energetically favorable in single vacancy in bcc W, clearly demonstrating the thermodynamic stability of multiple hydrogen segregation in monovacancy. Apart from monovacancy, hydrogen decorated vacancy voids were also intensively studied. Hayward et al. [20] found out a stable void configuration with 10 vacancies and 50 hydrogen atoms in bcc Fe. Geng et al. [22] reported energetically favorable hydrogen bubble in bcc Fe with the smallest configuration being 27 vacancies (see Figure 2.5b). These studies further confirmed the stability of hydrogen vacancy cluster in metals, implying the possibility of nanovoid nucleation and hydrogen bubble formation energetically.

On the other hand, it is well documented that vacancy can drastically retard hydrogen diffusion due to strong trapping effect in metals [33-35]. For example, by combining *ab initio* calculations with Kinetic Monte Carlo simulations, the effective diffusivity of hydrogen as a function of vacancy concentration in fcc Ni was obtained and the calculated value is several order of magnitude lower than the case as pristine bulk lattice without vacancy [36]. This slowdown in hydrogen diffusion caused by the presence of vacancy agrees well with the predicted values by Oriani's model, indicative of salient trapping impact of vacancy.

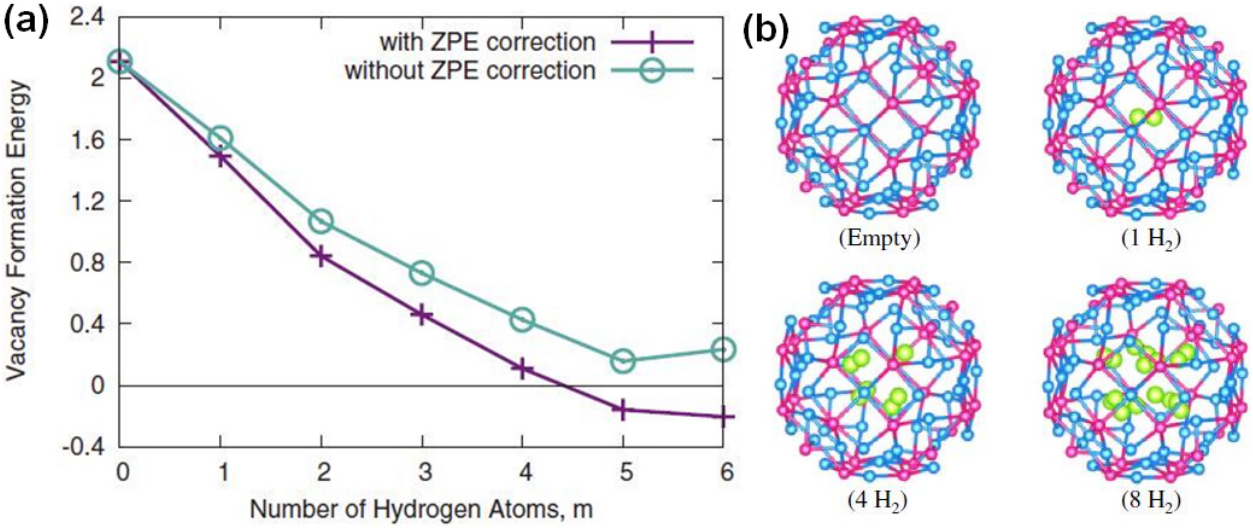

Figure 2.5. (a) Vacancy formation as a function of number of hydrogen atoms in bcc Fe [23]. (b) 27 vacancy voids with multiple hydrogen atoms in bcc Fe. Small pink balls represent Fe atoms, small blue balls show the adsorbed hydrogen atoms in void surface. Big green balls are hydrogen molecule [22]. [Figure adapted with permissions]

2.2.2 Dislocations

Dislocations are one category of most abundant defects in metals, dominating the plastic deformation via dislocation motion and multiplication [37, 38]. Hydrogen-dislocation interaction directly affects the plastic deformation process, and thus necessarily impacts HE. A major advance on this note was the postulation of the correlation between hydrogen and ductile features in metals, which was proposed by Beachem [39]. His work demonstrated hydrogen probably involved in the ductile failure process of HE. Followed by Beachem's study, a series of critical experiments based on transmission electron microscope (TEM) studies were conducted [40-43]. For example, the *in-situ* TEM observations of Fe samples under deformation with and without hydrogen demonstrated the decrease in separation distance between dislocations when hydrogen gas was introduced in the experiment [41] (see Figure 2.6). This result was regarded as the evidence of hydrogen dislocation-dislocation interactions. Other experiments conducted by Roberson et al. [40, 43-45] suggested hydrogen enhance the dislocation mobility. *In-situ* TEM observations were also carried out to track dislocation trajectories in the presence and absence of hydrogen, the snapshot of dislocation motion at different time steps is presented in Figure 2.7. The arrow in Figure 2.7 indicates the direction of dislocation motion with black curves at the initial position without introduction of hydrogen gas and white curves at new positions in the presence of hydrogen. From these snapshots, we can see some stationary dislocations in previous vacuum condition starting to move in hydrogen-containing environment with simultaneous dislocation velocity increase. When degassing hydrogen, dislocation stops moving again, indicating hydrogen might enhance the dislocation motion. However, due to the uncontrollable experiment conditions such high surface tension in their samples, the observed phenomena were probably not only caused by hydrogen solely, which needs more critical experiments to further confirm.

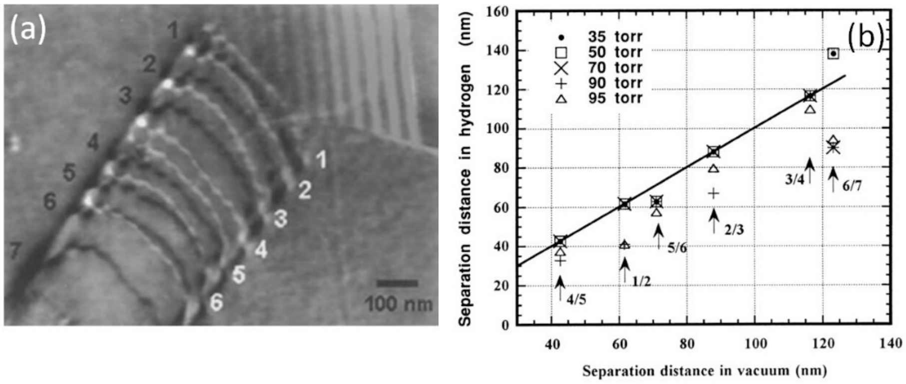

Figure 2.6. (a) The combined images of dislocation pile-ups with and without hydrogen gas. The black lines are initial positions without introducing hydrogen gas and white lines are new positions with hydrogen gas. (b) The separation distance in vacuum and under different hydrogen gas pressures [41]. [Figure adapted with permissions]

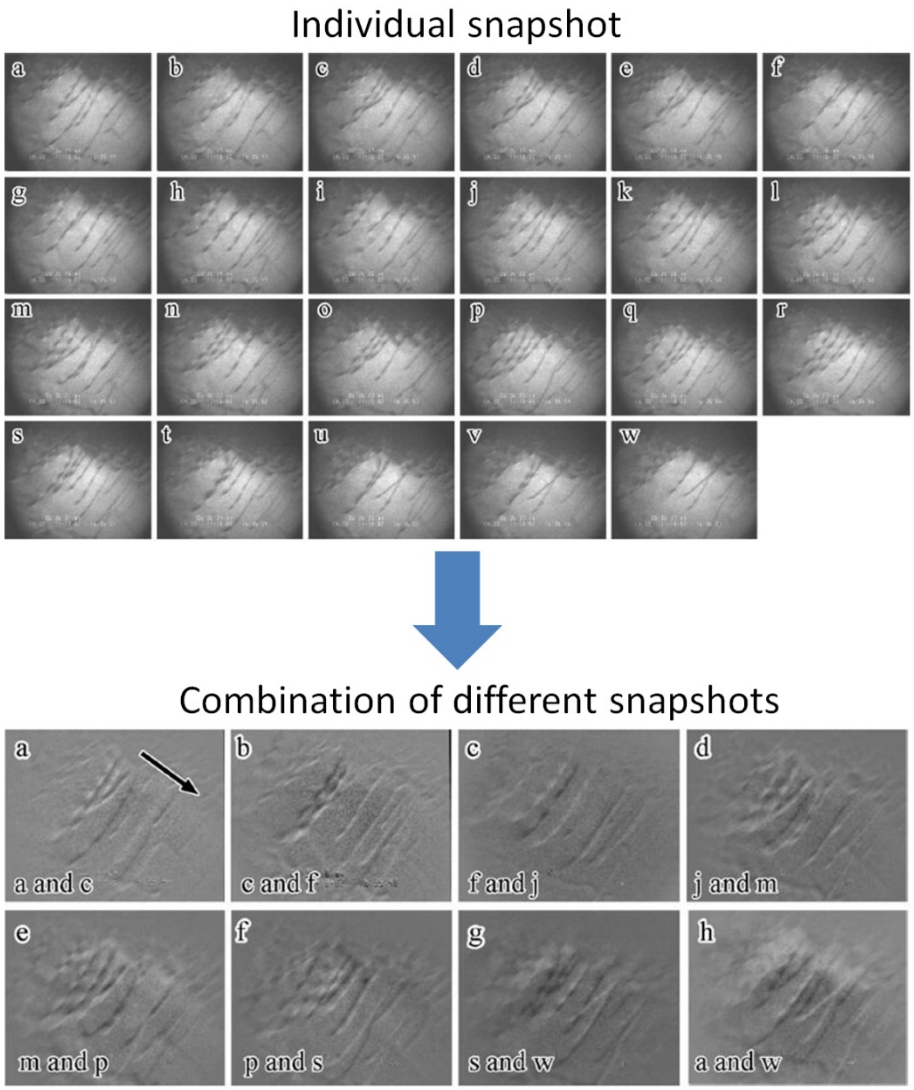

Figure 2.7. Top figure: individual images of dislocation motion induced by hydrogen. a~w represent different time. Bottom figure: the superimposed imaged adapted from top figure. The combined images from top figure are marked in the left bottom corner in each image. Black curves represent initial positions and white curve show new positions [43]. [Figure adapted with permissions]

More recently, some new experimental studies performed on Inconel 718 Ni-based alloys in the presence of hydrogen further demonstrated the influence of hydrogen on dislocation activities. *In-situ* Scanning Electron Microscope (SEM) studies performed by Zhou et al. [46, 47] revealed multiple dislocation slip bands existing in the samples with hydrogen charging. Crack initiation and propagation occur along these dislocation slip bands, suggesting the crucial role of hydrogen in affecting dislocation activities (see Figure 2.8a-c). It is worth noting that they also observed the nanovoid nucleation along dislocation slip bands and at the junctions between different dislocation slip bands (see Figure 2.8d-e) although the underlying mechanisms responsible for such phenomenon is still not clear.

Until now, though predominantly it was postulated that hydrogen tends to facilitate dislocation motion and to cause enhanced localized plasticity, there have been increasing new evidence to suggest otherwise. For example, one recent *in-situ* TEM experiment performed by Xie et al. [48] revealed that dislocations were “locked” in the presence of hydrogen. Their results are in sharp contrast to the “hydrogen enhanced plasticity” picture, raising critical concerns. Those opposite observations cast doubts on the exact role of hydrogen on dislocation activities, and call for new carefully designed experiments.

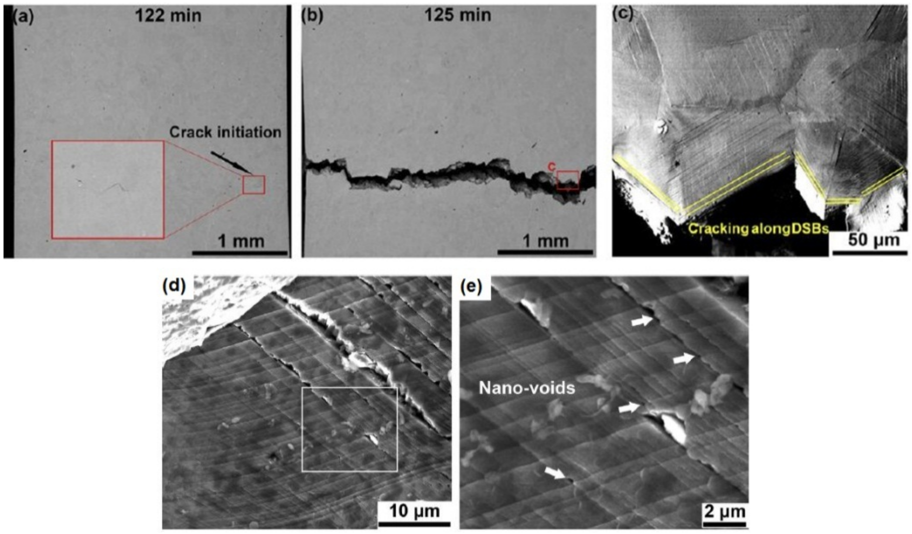

Figure 2.8. (a) SEM image of crack initiation at 122 min. (b) Magnified region of crack propagation at 125 min. (c) Fracture morphology with high magnifications [46]. (d)-(e) Enlarged

fractographs showing dislocation slip bands and nanovoids [47]. [Figure adapted with permissions]

Another important aspect regarding hydrogen-dislocation interaction is the influence of hydrogen on dislocation nucleation. The remarkable experimental studies by Barnoush et al. [49-52] shed some new light on better understanding this issue. Numerous nanoindentation tests have been performed for different structural metals. According to experimental results, they observed decrease in the *pop-in* load in presence of hydrogen (Here the *pop-in* load refers to the load plateau in the load-displacement curve during nanoindentation experiment). Figure 2.9 is the typical load-displacement curves of Fe-3%wt. Si alloy in air and under hydrogen charging condition, suggesting hydrogen can facilitate inhomogeneous dislocation nucleation in metals.

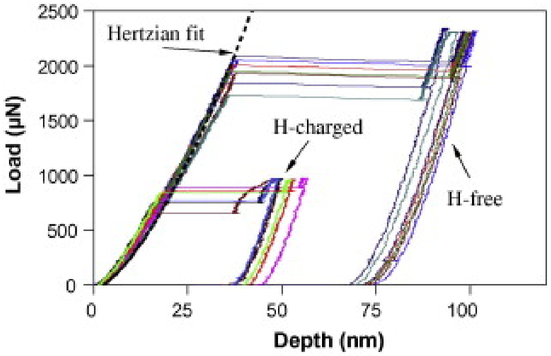

Figure 2.9. Nanoindentation load-displacement curves of Fe-3%wt.% Si alloy with and without hydrogen charging [49]. [Figure adapted with permissions]

Although those experimental studies have successfully provided us many meaningful insights, the unsolved issues regarding quantitatively detecting hydrogen occupation and gauging the local hydrogen concentration in dislocations at the atomic scale still hinders the better understanding of physical nature of HE in metals. Therefore, atomistic simulations are indispensable parts in tandem with experiments to break through the limitations aforementioned. Many atomistic simulations have been performed in the literature to verify hydrogen segregation and diffusion in dislocations at the atomic scale [35, 53, 54]. Taketomi et al. [55, 56] investigated hydrogen distribution and corresponding binding energies in various positions around a {112}<111> edge dislocation in bcc Fe, as shown in Figure 2.10. It was found that dislocation core region shows evident ability to trap hydrogen atoms, with the maximum binding energy being 0.49 eV. However, the capability of trapping hydrogen in core region is not static, since the hydrogen occupation and binding energy landscape can be drastically changed by hydrostatic and shear stress. Their results indicated external stress condition plays a vital role in hydrogen segregation profile in dislocations. Kimizuka et al. [57] used molecular dynamics simulations to examine the binding state of hydrogen in screw dislocation for bcc Fe. Their results demonstrated the same evident trapping effect exists in screw dislocation core region where the maximum binding energies of H in core region at 1000K and 300 K are 0.20 eV and 0.29 eV respectively. This binding state origins from the quantum effect due to electron density delocalized in core region (see Figure 2.11a-b). Itakura et al. [58] further reexamined the trapping effect of screw dislocation in bcc Fe by means of *ab initio* calculations. According to this study, different core structures were distinguished and hydrogen binding energies were mapped in the core region where the maximum binding energy is 0.26 eV and 0.39 eV for easy and hard core structure respectively. Similar to bcc Fe, both edge and screw dislocation in fcc Ni show strong attractive interaction with hydrogen atoms. It is worthy to note that core dissociation occurs in both edge and screw dislocation in fcc Ni. Therefore, hydrogen occupation and binding state strongly reply on the local atomic structure of dislocation core. Tang et al. [59] discovered that the most stable trapping sites resides in the octahedral sites near the Shockley partial cores for edge dislocation while the strongest binding sites in screw dislocation lie in the tetrahedral sites in stacking fault region and octahedral sites close to Shockley partial cores (see Figure 2.11c-d).

Aside from dislocation trapping and segregation, hydrogen diffusion in the proximity of dislocations is also important because the plastic deformation process can be severely influenced by hydrogen diffusion. Kimizuka et al. [57] systematically studied the hydrogen diffusivity in both edge and screw dislocation in bcc Fe via molecular dynamics simulations, it was found that there is no diffusion path with low migration barriers in both edge and screw dislocation core, indicative of low hydrogen diffusion behavior in dislocation core region. Recent study performed by Bombac et al. [60] also confirmed the confinement of hydrogen atoms to the dislocation core region in bcc Fe and no fast diffusion path existing in dislocations. In addition to afore mentioned studies, Tang et al. [59] also conducted molecular statics simulations to obtain hydrogen migration barriers in the region around the dislocation in fcc Ni. It was discovered that hydrogen can fast transport in the region around Shockley partial dislocation core due to the fast diffusion paths with relative low migration barriers compared to the migration barrier in bulk Ni lattice (see Figure 2.12). Therefore, based on the aforementioned works, there still exist controversies regarding hydrogen kinetics in dislocations, which necessities more comprehensive studies to clarify hydrogen diffusion behaviors in dislocations.

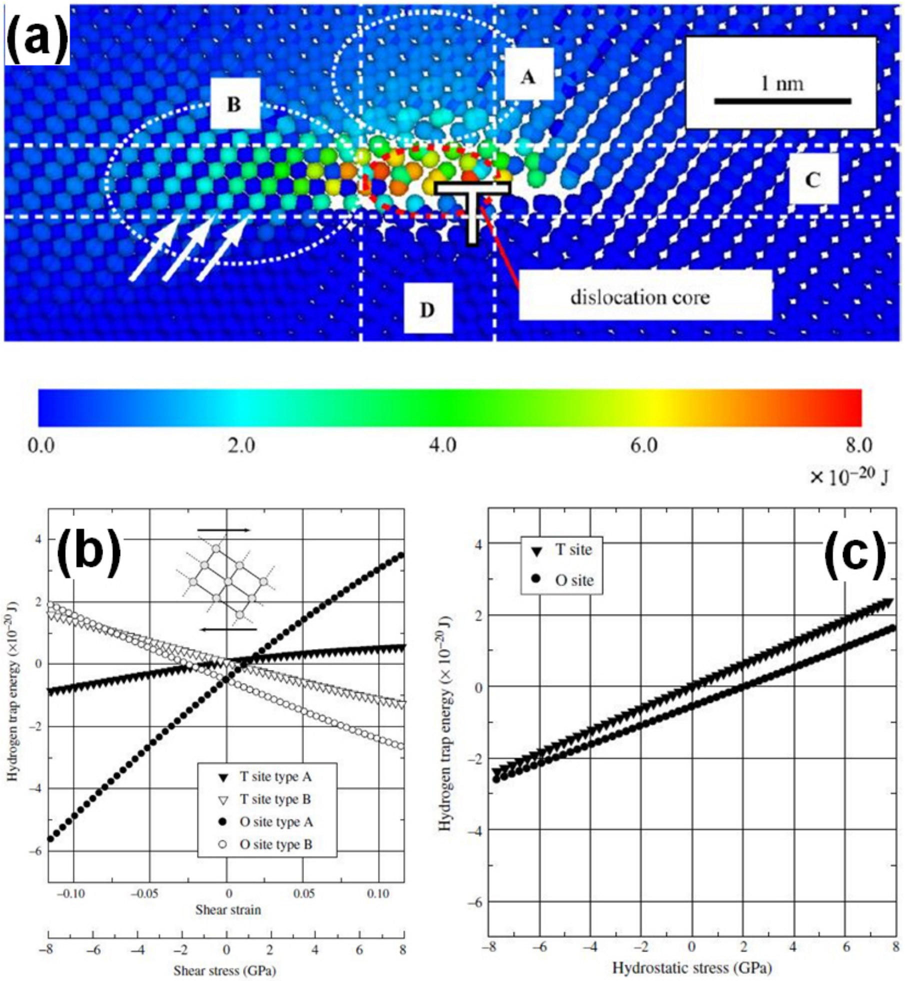

Figure 2.10. (a) Hydrogen binding energy map around bcc Fe edge dislocation. (b) Hydrogen binding energy as a function of shear stress. (c) Hydrogen binding energy as a function of hydrostatic stress [56]. [Figure adapted with permissions]

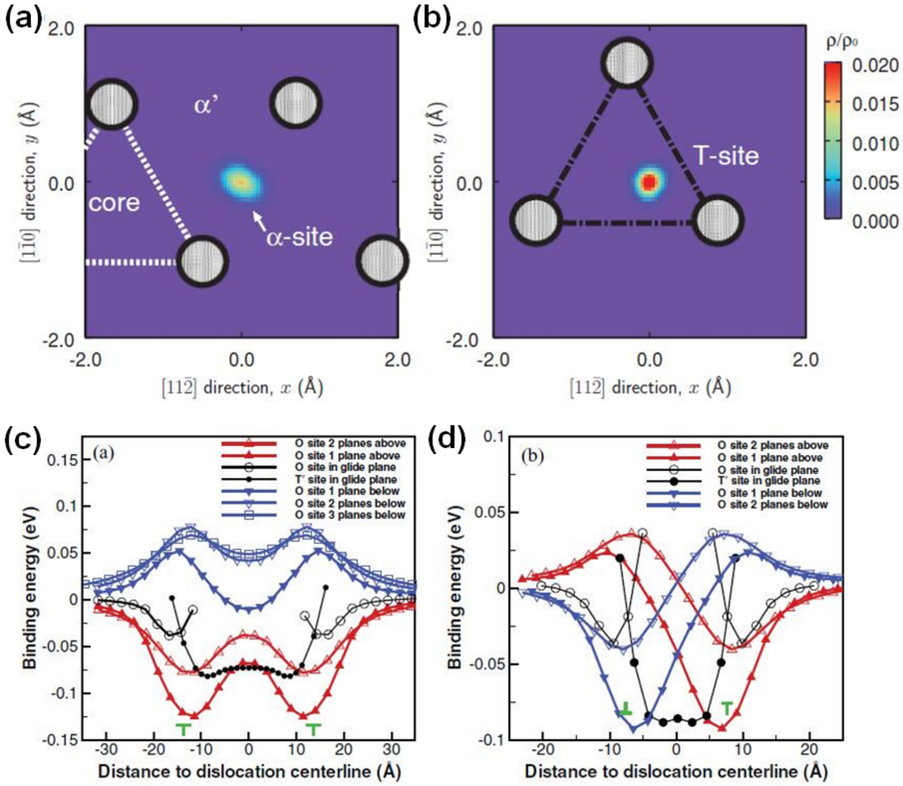

Figure 2.11. Electron density contour plot of one hydrogen atom at most stable trapping site around screw dislocation core (a) and at tetrahedral interstitial site in bulk lattice (b) in bcc Fe [57]. Binding energy of hydrogen atom at different position to edge dislocation (c) and screw dislocation (d) in fcc Ni. Note: green T symbol represents the position of Shockley partial dislocation core [59]. [Figure adapted with permissions]

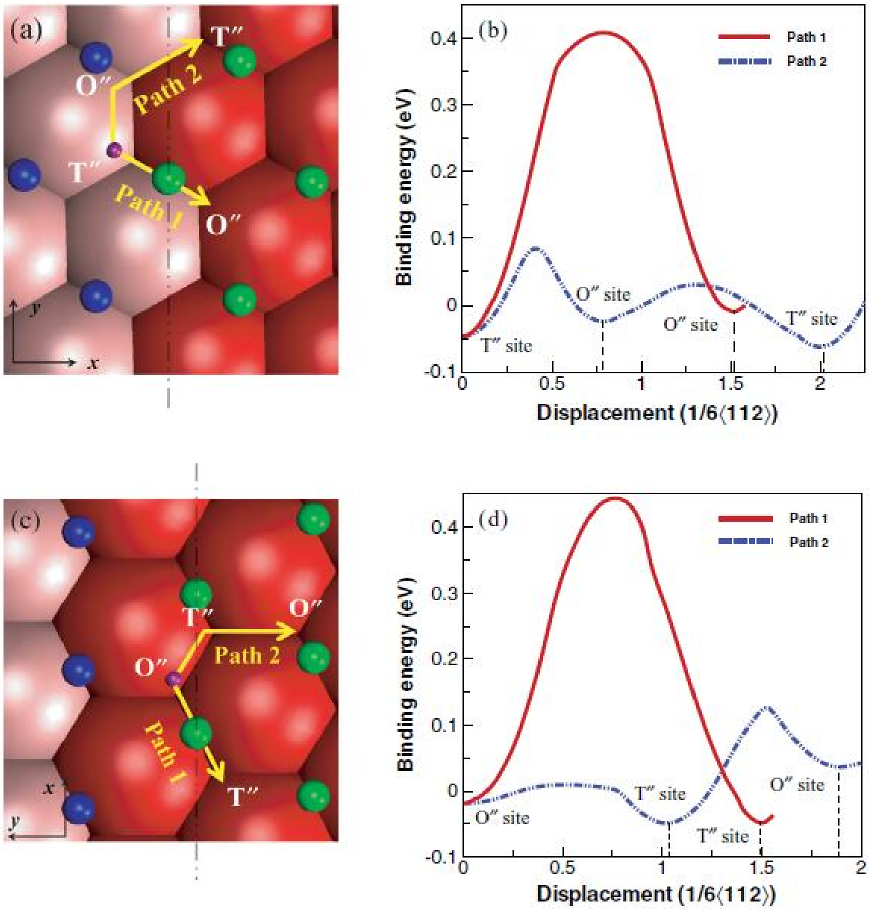

Figure 2.12. (a) Different migration path of hydrogen in Shockley partial core of edage dislocation in fcc Ni. (b) hydrogen diffusion barrier along identified path in edge dislocation. (c) Different migration path of hydrogen in Shockley partial core of screw dislocation in fcc Ni. (d) hydrogen diffusion barrier along identified path in screw dislocation. [Figure adapted with permissions]

2.2.3 Grain boundary

Grain boundary is another prevailing heterogeneity widely existed in polycrystalline materials, governing a series of mechanical properties such as strength and toughness of metals [61, 62]. The interactions between hydrogen and grain boundaries show detrimental effect on mechanical properties, resulting in intergranular fracture for metals. Numerous experimental studies reveal grain boundaries are vulnerable to hydrogen attack. Pfeil et al. [63] first noted the fracture of iron sample after acid immersion mostly occurring at grain boundaries, shown in Figure 2.13a. Lynch et al. [64] also found intergranular fracture in the vicinity of grain boundaries under hydrogen charging in various metals such as austenite steel (see Figure 2.13b). However, other researchers claimed that the observed intergranular failure mode is not induced by isolated hydrogen-grain boundary interaction. Alternatively, the active dislocation evolution caused by hydrogen segregation at grain boundaries are the key factors in hydrogen-caused intergranular fracture [65, 66]. For instance, Wang et al. [66] discovered the fractured surface microstructure in hydrogen-charging specimens with complicated dislocation evolution which was not observed in hydrogen-free samples, suggesting severe plasticity induced by hydrogen (see Figure 2.13c). This enhanced plasticity can bring about large amounts of hydrogen in the region of grain boundaries and finally result in premature crack (see Figure 2.13d).

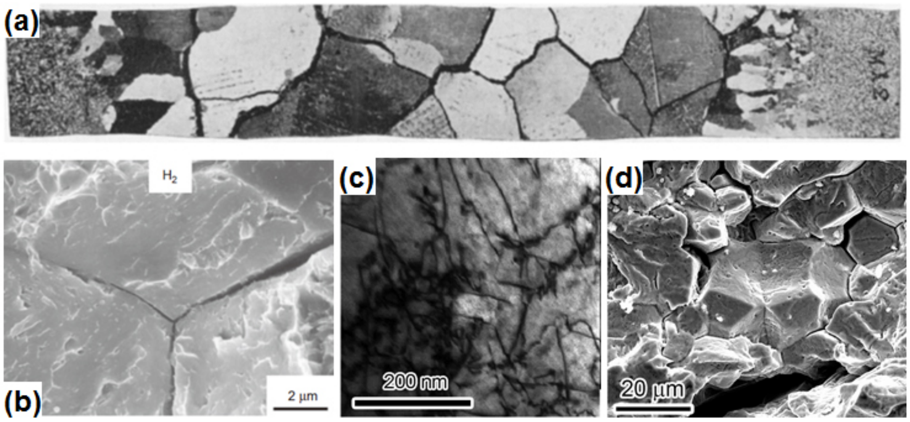

Figure 2.13. (a) Morphology of iron sample immersed in acid [63]. (b) SEM of fracture surfaces of high-strengthen martensitic steel in the presence of hydrogen [64]. (c) dislocation evolution underneath the fracture surface of the iron sample after hydrogen charging [66].(d) SEM of fracture surfaces of the iron sample under hydrogen charging condition [66]. [Figure adapted with permissions]

Among many kinds of grain boundaries, of particular interest is so-called special grain boundary with low grain boundary energy such as twin boundary. These special grain boundaries can inherently reduce the segregation tendency of impurities, which have intrinsic resistance to intergranular fracture [67]. The strategy of introducing special grain boundaries to increase mechanical properties and reduce intergranular failure is known as “grain boundary engineering” [68, 69]. As for HE in metals, the same idea was used to alleviate HE. Bechtle et al. [70] adopted “grain boundary engineering” to tune the microstructure of pure Ni and obtained high-quality samples with a high fraction of special grain boundaries. They found that special grain boundaries (especially for twin boundary) have strong resistance to HE compared to specimens with a low fraction of special grain boundaries (see Figure 2.14). However, this conclusion was faced with severe challenges due to other opposite experimental observations. For instance, many studies discovered hydrogen-assisted failure along twin boundaries in austenitic steel [71-73]. More recently, Seita et al. [74] pointed out the coherent twin boundary in the Ni-based alloy is vulnerable to hydrogen-induced crack initiation but are resistant to crack propagation, indicative of the dual role of coherent twin boundary in HE (see Figure 2.15). Therefore, the mechanisms regarding hydrogen-induced grain boundary decohesion is still not clear.

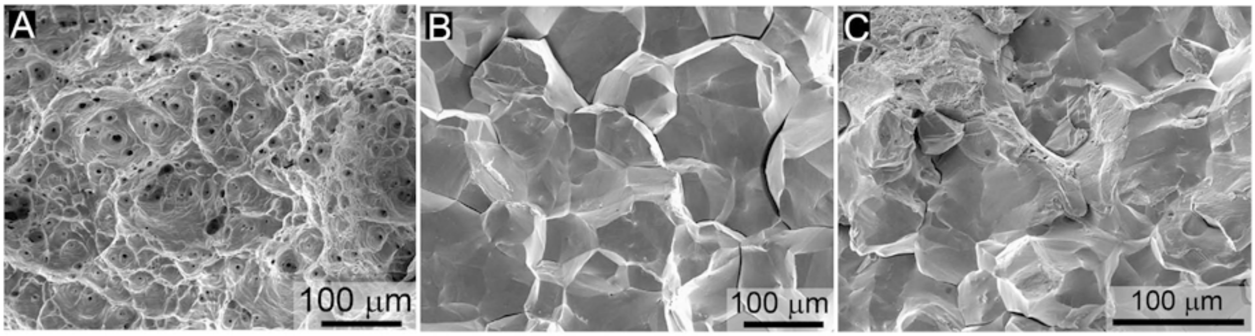

Figure 2.14. SEM images of fracture surfaces. (a) Fractography of Ni sample in the absence of hydrogen. (b) The fracture surface of Ni sample with a low proportion of special grain boundaries under hydrogen charging condition. (c) The fracture surface of Ni sample with a high fraction of special grain boundaries in the presence of hydrogen [70]. [Figure adapted with permissions]

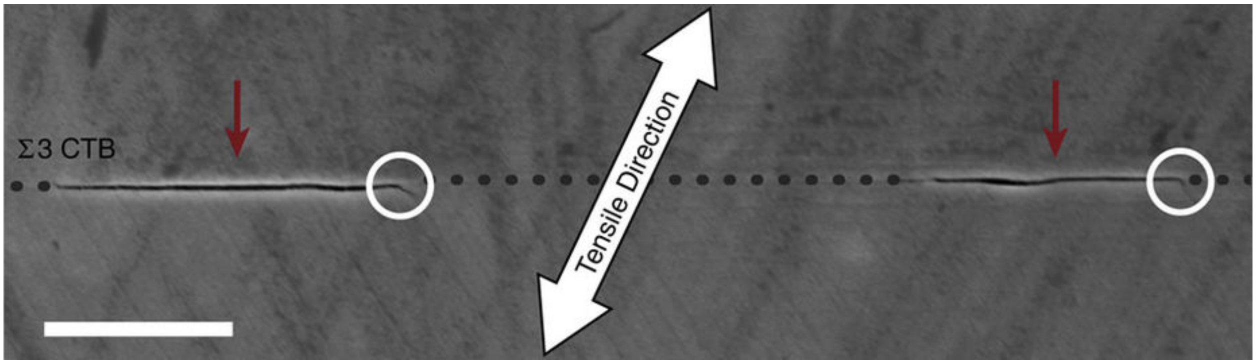

Figure 2.15. SEM image suggesting crack initiation and propagation at coherent twin boundary under hydrogen charging condition [74]. [Figure adapted with permissions]

Although many macroscale experimental studies confirmed that hydrogen segregation and diffusion at grain boundaries are very significant for hydrogen induced intergranular fracture, the convinced mechanism at the atomic scale regarding hydrogen assisted intergranular cracking along grain boundary is still far from being accepted. Therefore, constant efforts were devoted for calrification of the whole physical picture for hydrogen segregation and transport at grain boundaries by atomistic simulations. Geng et al. [75] employed first principles calculations to study the hydrogen impurity at the ∑5 grain boundary in fcc Ni. In this work, they found the expansion of chemical bond between impurity and host Ni atom, which might be one potential reason of grain boundary decohesion. Similar studies on the same system were also done by Yamagchi et al [76] by means of first principle calculations. The calculated segregation energy of hydrogen in most stable site is -0.3 eV, depicting the preference of hydrogen atom to reside at grain boundary rather than Ni bulk lattice. Du et al. [77] used many kinds of grain boundaries in both bcc and fcc Fe to examine the correlation between hydrogen trapping and grain boundary structure by *ab initio* calculations. Based on their calculations, they observed the trapping tendency of hydrogen at grain boundary strongly depends on the local atomic structure (see Figure 2.16). In particular, the ∑3 coherent twin boundary and ∑11 grain boundary show the minimum segregation tendency whereas hydrogen atom is energetically favorable at ∑5 grain boundary. They claimed this difference is derived from the local atomic volume at grain boundary. Similar hydrogen accumulation at grain boundaries in bcc Fe was also reexamined by Mirzaev et al. [78], they confirmed the similar hydrogen segregation tendency in ∑3 and ∑5 grain boundaries as Du's results, suggesting that the local space in grain boundary is the key factor in determining hydrogen trapping state. In addition to first principles calculations, some researchers also utilized molecular dynamics simulations to scrutinize the hydrogen segregation in relative large grain boundary model. Baskes et al. [79] investigated the trapping of hydrogen at grain boundaries in fcc Ni, where there are three kinds of symmetric tilt grain boundaries involved in their study (∑11, ∑9 and ∑17 grain boundaries). They first used the "structural unit model" concept to characterize grain boundary structure, where grain boundaries can be treated as a number of compact polyhedrons (see Figure 2.17),which can act as potential hydrogen trapping sites.

With respect to hydrogen diffusion behavior at grain boundaries, a myriad of experimental studies and atomistic simulations were performed [80-82]. However, there still exist controversy in the kinetic processes of hydrogen at grain boundaries. Du et al. [77] conducted first principles calculations to accurately obtain the migration barriers of hydrogen at different grain boundaries in bcc and fcc Fe, as shown in Figure 2.18. It was found that there is no fast diffusion path due to higher calculated barriers than that in bulk lattice. Furthermore, they performed Kinetic Monte Carlo simulations and confirmed that the effective diffusivity is apparently lower than hydrogen normal diffusivity in regular lattice [83]. More recent atomistic simulations by Stefano et al. [84] reported that hydrogen diffusion behavior depends on the local atomic structure of grain boundary using two distinct fcc Ni grain boundaries (i.e., ∑3 and ∑5 grain boundaries). In light of calculated results, they concluded ∑3 grain boundary cannot facilitate hydrogen diffusion while ∑5 grain boundary can be considered as fast diffusion path for hydrogen due to very low migration barrier as compared to barrier of hydrogen in bulk lattice.

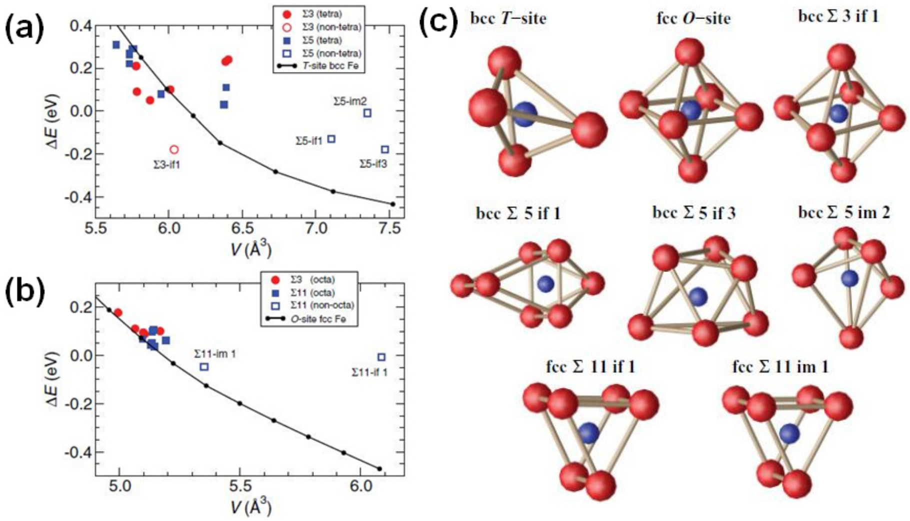

Figure 2.16. (a) Hydrogen binding energy as a function of atomic volume of multiple site in various grain boundares in bcc Fe. (b) Hydrogen binding energy as a function of atomic volume of multiple site in various grain boundares in fcc Fe. (c) Local atomic structure of hydrogen trapping sites where the small blue ball represents hydrogen atom and big red ball shows host Fe atom [77]. [Figure adapted with permissions]

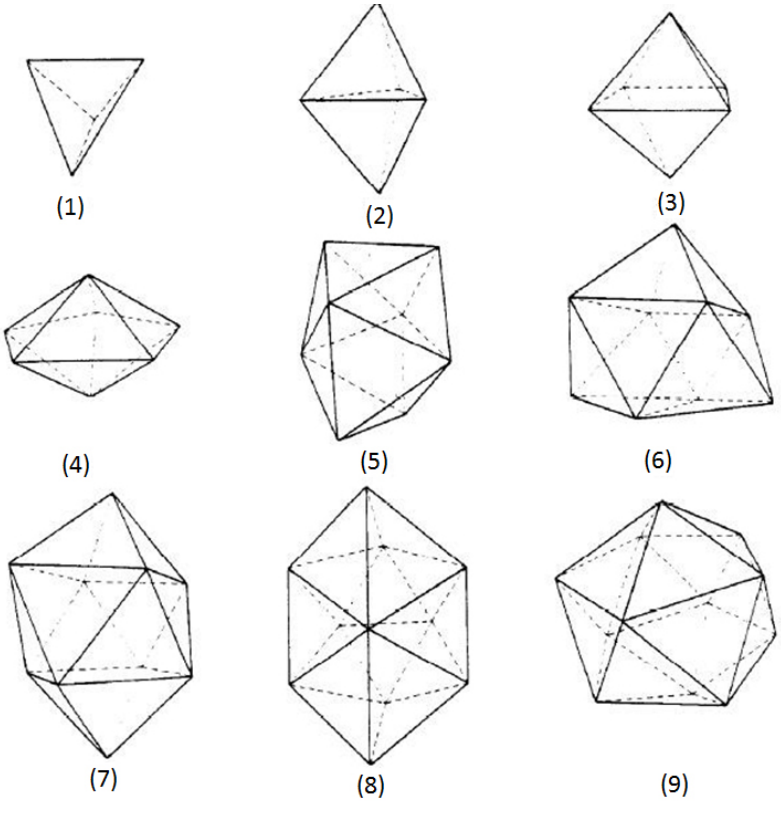

Figure 2.17. Polyhedral structure units in three dimensions. (1) Tetrahedron (2) Bi-tetrahedron (3) octahedron (4)Pentagonal bipyramid (5) Tetragonal dodecahedron (6) Cpped trigonal prism

(7) Archimedian antiprism (8) Octadecahedron (9) Regular icosahedron [85]. [Figure adapted with permissions]

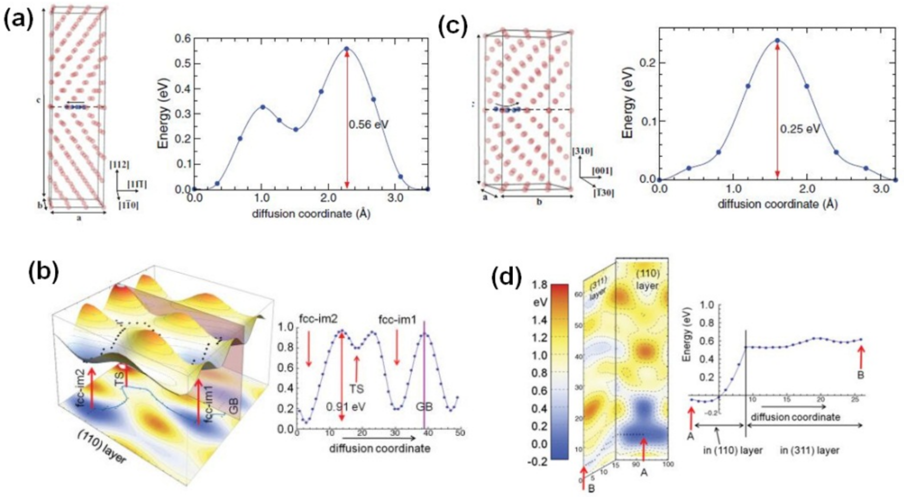

Figure 2.18. (a) Hydrogen migration path along ∑3 grain boundary and the migration barrier in bcc Fe. (b) Hydrogen migration path along ∑5 grain boundary and the migration barrier in bcc Fe. (c) Hydrogen diffusion barrier contour plot for ∑3 grain boundary in fcc Fe. (d) Hydrogen diffusion path at ∑11 grain boundary and the corresponding migration barriers in fcc Fe [77]. [Figure adapted with permissions]

2.3 Mechanisms of hydrogen embrittlement in metals

In foregoing sections, we systematically surveyed the pivotal experiments and atomistic simulations on HE, implying the interplays of hydrogen and microstructures are of extreme importance. Based on the analysis of these key experimental observations and atomistic simulations, various mechanisms have been proposed to interpret HE. Hereinafter, we discuss the commonly invoked mechanisms that can successfully account for some characteristics of HE in experimental observations.

2.3.1 Hydrogen and deformation-assisted vacancy formation

Hydrogen and deformation-assisted vacancy formation was proposed by Nagumo et al. [16-18], this mechanism postulates the excess vacancies generated by plastic deformation in metals can be stabilized by hydrogen, thereby resulting in the increase of vacancy concentration. This stabilization of excess vacancy induced by hydrogen is attributed to the scenario that hydrogen and vacancy can combine together to form hydrogen-vacancy clusters due to the prominent reduction of vacancy formation energy [24, 27]. The stabilized hydrogen-decorated vacancies can aggregate to form nanovoids, which can be seen as the embryos of crack initiation in metals. Although there are some experimental observations revealing nanovoids do exist at hydrogen caused brittle fracture surfaces [19] and some theoretical studies confirming the vacancy formation energy reduced by hydrogen [86], the kinetic processes regarding how hydrogen-vacancy clusters accumulate together or migrate to grain boundaries to promote crack initiation still remain unknown.

2.3.2 Hydrogen enhanced localized plasticity

Hydrogen-enhanced localized plasticity (HELP) was first described by Beachem as a new mechanism for the sake of interpreting hydrogen-assisted fracture [39]. He hypothesized that the stress field interactions between hydrogen and dislocations can reduce the interaction energy between dislocations and obstacles as well as the interactions among dislocation pile-ups, leading to increased dislocation mobility. Thereafter, Birnbaum, Robertson et al.[42, 44, 87-93] flourished HELP mechanism. Specifically, Birnbaum and Robertson utilized *in-situ* TEM to perform straining experiments in the absence and presence of hydrogen to monitor the effect of hydrogen on dislocation mobility, as discussed in previous section. They found faster dislocation movement in the presence of hydrogen gas. After removal of hydrogen gas, the dislocation velocity decreased, demonstrating the facilitation of dislocation motion with hydrogen. Despite numerous experimental studies supporting HELP mechanism, other experiments demonstrated the opposite conclusions. For example, recent *in-situ* TEM experiments for hydrogen aluminum system suggests retardation of dislocation motion with hydrogen, which is totally opposite to Robertson's results [48]. Therefore, the role of hydrogen in dislocation behavior is still not fully understood.

2.3.3 Hydrogen enhanced decohesion

The hydrogen enhanced decohesion (HEDE) mechanism was initially put forward by Pfeil [63], who found that hydrogen atoms can weaken the cohesive strength among cubic cleavage planes. After that, Troiano et al. [94] proposed the reduction of cohesion of Fe grain boundaries derived from electron interplay between hydrogen and Fe. In detail, when hydrogen atoms are dissolved in transition metals (Fe, Co, Ni, etc.), its electrons could enter the *d* bands of the host atoms, leading to overlapping of *d* bands and creating repulsive forces. This would finally enlarge the equilibrium atomic distance and reduce lattice strength. Additionally, Oriani [95-99] considered that brittle fracture can happen when the external local stress is equal to the maximum cohesive force per unit area in the vicinity of the crack tip. When hydrogen atoms reside in structural materials, the local hydrogen concentration will rise up with the increase of strain rate and hydrogen concentration, leading to the reduction of cohesive force in matrix atoms. Therefore, the mechanical work for cleavage in the aforementioned crystal model is lower in the presence of hydrogen than the absence of hydrogen. However, some issues still exist in HEDE mechanism. For example, the occurrence of hydrogen induced intergranular fracture necessities high hydrogen concentration. However, how such huge amount of hydrogen can arrive at crack tips or grain boundaries kinetically is still not clear.

2.4 References

[1] Borchers C, Michler T, Pundt A. Effect of hydrogen on the mechanical properties of stainless steels. Advanced Engineering Materials 2008;10:11-23.
[2] Myers SM, Baskes M, Birnbaum H, Corbett JW, DeLeo G, Estreicher S, et al. Hydrogen interactions with defects in crystalline solids. Reviews of Modern Physics 1992;64:559.
[3] Gao L, Conway B. Absorption and adsorption of H in the H2 evolution reaction and the effects of co-adsorbed poisons. Electrochimica acta 1994;39:1681-93.
[4] Chun JH, Ra KH, Kim NY. Qualitative analysis of the Frumkin adsorption isotherm of the over-potentially deposited hydrogen at the poly-Ni/KOH aqueous electrolyte interface using the phase-shift method. Journal of the Electrochemical Society 2002;149:E325-E30.
[5] Harrington D, Conway B. Kinetic theory of the open-circuit potential decay method for evaluation of behaviour of adsorbed intermediates: Analysis for the case of the H2 evolution reaction. Journal of electroanalytical chemistry and interfacial electrochemistry 1987;221:1-21.
[6] Iyer RN, Pickering HW, Zamanzadeh M. Analysis of Hydrogen Evolution and Entry into Metals for the Discharge ‐ Recombination Process. Journal of the Electrochemical Society 1989;136:2463-70.
[7] McCright R, Staehle R. Effect of Arsenic Upon The Entry of Hydrogen Into Mild Steel as Determined at Constant Electrochemical Potential. Journal of The Electrochemical Society 1974;121:609-18.
[8] Figueroa-Gordon DJ. Hydrogen re-embrittlement susceptibility of ultra high strength steels: Cranfield University; 2005.
[9] Sriraman K, Strauss H, Brahimi S, Chromik R, Szpunar J, Osborne J, et al. Tribological behavior of electrodeposited Zn, Zn–Ni, Cd and Cd–Ti coatings on low carbon steel substrates. Tribology International 2012;56:107-20.
[10] Sriraman K, Brahimi S, Szpunar J, Osborne J, Yue S. Characterization of corrosion resistance of electrodeposited Zn–Ni Zn and Cd coatings. Electrochimica Acta 2013;105:314-23.

[11] Fukai Y. Formation of superabundant vacancies in M–H alloys and some of its consequences: a review. Journal of Alloys and Compounds 2003;356:263-9.

[12] Fukai Y, Ōkuma N. Evidence of copious vacancy formation in Ni and Pd under a high hydrogen pressure. Japanese journal of applied physics 1993;32:L1256.

[13] Fukai Y, Ōkuma N. Formation of superabundant vacancies in Pd hydride under high hydrogen pressures. Physical review letters 1994;73:1640.

[14] Nakamura K, Fukai Y. High-pressure studies of high-concentration phases of the TiH system. Journal of alloys and compounds 1995;231:46-50.

[15] Fukai Y, Shizuku Y, Kurokawa Y. Superabundant vacancy formation in Ni–H alloys. Journal of alloys and compounds 2001;329:195-201.

[16] Nagumo M, Yagi T, Saitoh H. Deformation-induced defects controlling fracture toughness of steel revealed by tritium desorption behaviors. Acta materialia 2000;48:943-51.

[17] Nagumo M, Ohta K, Saitoh H. Deformation induced defects in iron revealed by thermal desorption spectroscopy of tritium. Scripta Materialia 1999;40:313-9.

[18] Takai K, Shoda H, Suzuki H, Nagumo M. Lattice defects dominating hydrogen-related failure of metals. Acta Materialia 2008;56:5158-67.

[19] Neeraj T, Srinivasan R, Li J. Hydrogen embrittlement of ferritic steels: observations on deformation microstructure, nanoscale dimples and failure by nanovoiding. Acta Materialia 2012;60:5160-71.

[20] Hayward E, Deo C. Energetics of small hydrogen–vacancy clusters in bcc iron. Journal of Physics: Condensed Matter 2011;23:425402.

[21] Nazarov R, Hickel T, Neugebauer J. First-principles study of the thermodynamics of hydrogen-vacancy interaction in fcc iron. Physical Review B 2010;82:224104.

[22] Geng W, Wan L, Du J-P, Ishii A, Ishikawa N, Kimizuka H, et al. Hydrogen bubble nucleation in α-iron. Scripta Materialia 2017;134:105-9.

[23] Hayward E, Fu C-C. Interplay between hydrogen and vacancies in α-Fe. Physical Review B 2013;87:174103.

[24] Lu G, Kaxiras E. Hydrogen embrittlement of aluminum: the crucial role of vacancies. Physical review letters 2005;94:155501.

[25] Nordlander P, No J, Besenbacher F, Myers S. Multiple deuterium occupancy of vacancies in Pd and related metals. Physical Review B 1989;40:1990.

[26] Hayward E, Hayward R, Fu C-C. Predicting distinct regimes of hydrogen behavior at nano-cavities in metals. Journal of Nuclear Materials 2016;476:36-44.

[27] Tateyama Y, Ohno T. Stability and clusterization of hydrogen-vacancy complexes in α− Fe: An ab initio study. Physical Review B 2003;67:174105.

[28] Hayward E, Beeler B, Deo C. Multiple hydrogen trapping at monovacancies. Philosophical Magazine Letters 2012;92:217-25.

[29] Connétable D, Wang Y, Tanguy D. Segregation of hydrogen to defects in nickel using first-principles calculations: The case of self-interstitials and cavities. Journal of Alloys and Compounds 2014;614:211-20.

[30] Tanguy D, Wang Y, Connétable D. Stability of vacancy-hydrogen clusters in nickel from first-principles calculations. Acta Materialia 2014;78:135-43.

[31] Metsue A, Oudriss A, Feaugas X. Hydrogen solubility and vacancy concentration in nickel single crystals at thermal equilibrium: New insights from statistical mechanics and ab initio calculations. Journal of Alloys and Compounds 2016;656:555-67.

[32] Liu Y-L, Zhang Y, Zhou H-B, Lu G-H, Liu F, Luo G-N. Vacancy trapping mechanism for hydrogen bubble formation in metal. Physical Review B 2009;79:172103.

[33] Oda T, Zhu D, Watanabe Y. Kinetic Monte Carlo simulation on influence of vacancy on hydrogen diffusivity in tungsten. Journal of Nuclear Materials 2015;467:439-47.

[34] Lu T, Niu G-J, Xu Y, Wang J, An Z, Liu H, et al. Molecular dynamics study of the diffusion properties of H in Fe with point defects. Fusion Engineering and Design 2016;113:340-5.

[35] Ramasubramaniam A, Itakura M, Ortiz M, Carter E. Effect of atomic scale plasticity on hydrogen diffusion in iron: Quantum mechanically informed and on-the-fly kinetic Monte Carlo simulations. Journal of Materials Research 2008;23:2757-73.

[36] Wang Y, Connétable D, Tanguy D. Influence of trap connectivity on H diffusion: Vacancy trapping. Acta Materialia 2016;103:334-40.

[37] Li X, Wei Y, Lu L, Lu K, Gao H. Dislocation nucleation governed softening and maximum strength in nano-twinned metals. Nature 2010;464:877-80.

[38] Mughrabi H. Dislocation wall and cell structures and long-range internal stresses in deformed metal crystals. Acta metallurgica 1983;31:1367-79.

[39] Beachem CD. A new model for hydrogen-assisted cracking (hydrogen “embrittlement”). MT 1972;3:441-55.

[40] Robertson IM, Birnbaum HK. An HVEM study of hydrogen effects on the deformation and fracture of nickel. Acta Metallurgica 1986;34:353-66.

[41] Ferreira P, Robertson I, Birnbaum H. Hydrogen effects on the interaction between dislocations. Acta materialia 1998;46:1749-57.

[42] Ferreira PJ, Robertson IM, Birnbaum HK. Hydrogen effects on the character of dislocations in high-purity aluminum. Acta Materialia 1999;47:2991-8.

[43] Robertson IM. The effect of hydrogen on dislocation dynamics. Engineering Fracture Mechanics 2001;68:671-92.

[44] Tabata T, Birnbaum HK. Direct observations of the effect of hydrogen on the behavior of dislocations in iron. Scripta Metallurgica 1983;17:947-50.

[45] Robertson I, Birnbaum H, Heubaum F, Tabata T, Wei W. Hydrogen embrittlement and grain boundary fracture. Scr Metall;(United States) 1984;18.

[46] Zhang Z, Obasi G, Morana R, Preuss M. In-situ observation of hydrogen induced crack initiation in a nickel-based superalloy. Scripta Materialia 2017;140:40-4.

[47] Zhang Z, Obasi G, Morana R, Preuss M. Hydrogen assisted crack initiation and propagation in a nickel-based superalloy. Acta Materialia 2016;113:272-83.

[48] Xie D, Li S, Li M, Wang Z, Gumbsch P, Sun J, et al. Hydrogenated vacancies lock dislocations in aluminium. Nature communications 2016;7:13341.

[49] Barnoush A, Vehoff H. Recent developments in the study of hydrogen embrittlement: Hydrogen effect on dislocation nucleation. Acta Materialia 2010;58:5274-85.

[50] Barnoush A. Correlation between dislocation density and nanomechanical response during nanoindentation. Acta materialia 2012;60:1268-77.

[51] Barnoush A, Asgari M, Johnsen R. Resolving the hydrogen effect on dislocation nucleation and mobility by electrochemical nanoindentation. Scripta Materialia 2012;66:414-7.

[52] Stenerud G, Johnsen R, Olsen JS, He J, Barnoush A. Effect of hydrogen on dislocation nucleation in alloy 718. International Journal of Hydrogen Energy 2017.

[53] Lu G, Zhang Q, Kioussis N, Kaxiras E. Hydrogen-Enhanced Local Plasticity in Aluminum: An Ab Initio Study. Physical Review Letters 2001;87:095501.

[54] Angelo JE, Moody NR, Baskes MI. Trapping of hydrogen to lattice defects in nickel. Modelling and Simulation in Materials Science and Engineering 1995;3:289.

[55] Taketomi S, Matsumoto R, Miyazaki N. Atomistic simulation of the effects of hydrogen on the mobility of edge dislocation in alpha iron. J Mater Sci 2008;43:1166-9.

[56] Taketomi S, Matsumoto R, Miyazaki N. Atomistic study of hydrogen distribution and diffusion around a {112}<111> edge dislocation in alpha iron. Acta Materialia 2008;56:3761-9.

[57] Kimizuka H, Ogata S. Slow diffusion of hydrogen at a screw dislocation core in α-iron. Physical Review B 2011;84:024116.

[58] Itakura M, Kaburaki H, Yamaguchi M, Okita T. The effect of hydrogen atoms on the screw dislocation mobility in bcc iron: A first-principles study. Acta Materialia 2013;61:6857-67.

[59] Tang Y, El-Awady JA. Atomistic simulations of the interactions of hydrogen with dislocations in fcc metals. Physical Review B 2012;86:174102.

[60] Bombac D, Katzarov I, Pashov D, Paxton A. Theoretical evaluation of the role of crystal defects on local equilibrium and effective diffusivity of hydrogen in iron. Materials Science and Technology 2017;33:1505-14.

[61] Lu K, Lu L, Suresh S. Strengthening materials by engineering coherent internal boundaries at the nanoscale. science 2009;324:349-52.

[62] Ma E, Zhu T. Towards strength–ductility synergy through the design of heterogeneous nanostructures in metals. Materials Today 2017.

[63] Pfeil L. The effect of occluded hydrogen on the tensile strength of iron. Proceedings of the Royal Society of London Series A, Containing Papers of a Mathematical and Physical Character 1926;112:182-95.

[64] Lynch S. Environmentally assisted cracking: overview of evidence for an adsorption-induced localised-slip process. Acta Metallurgica 1988;36:2639-61.

[65] Robertson IM, Sofronis P, Nagao A, Martin M, Wang S, Gross D, et al. Hydrogen embrittlement understood. Metall and Mat Trans A 2015;46:2323-41.

[66] Wang S, Martin ML, Sofronis P, Ohnuki S, Hashimoto N, Robertson IM. Hydrogen-induced intergranular failure of iron. Acta Materialia 2014;69:275-82.

[67] Bruley J, Keast V, Williams DB. An EELS study of segregation-induced grain-boundary embrittlement of copper. Acta materialia 1999;47:4009-17.

[68] Randle V. Twinning-related grain boundary engineering. Acta materialia 2004;52:4067-81.

[69] Randle V. Mechanism of twinning-induced grain boundary engineering in low stacking-fault energy materials. Acta materialia 1999;47:4187-96.

[70] Bechtle S, Kumar M, Somerday BP, Launey ME, Ritchie RO. Grain-boundary engineering markedly reduces susceptibility to intergranular hydrogen embrittlement in metallic materials. Acta Materialia 2009;57:4148-57.

[71] Koyama M, Akiyama E, Tsuzaki K, Raabe D. Hydrogen-assisted failure in a twinning-induced plasticity steel studied under in situ hydrogen charging by electron channeling contrast imaging. Acta Materialia 2013;61:4607-18.

[72] Koyama M, Akiyama E, Sawaguchi T, Raabe D, Tsuzaki K. Hydrogen-induced cracking at grain and twin boundaries in an Fe–Mn–C austenitic steel. Scripta Materialia 2012;66:459-62.

[73] Chen S, Zhao M, Rong L. Hydrogen-induced cracking behavior of twin boundary in γ' phase strengthened Fe–Ni based austenitic alloys. Materials Science and Engineering: A 2013;561:7-12.

[74] Seita M, Hanson JP, Gradečak S, Demkowicz MJ. The dual role of coherent twin boundaries in hydrogen embrittlement. Nature communications 2015;6.

[75] Geng WT, Freeman AJ, Wu R, Geller CB, Raynolds JE. Embrittling and strengthening effects of hydrogen, boron, and phosphorus on a Σ5 nickel grain boundary. Physical Review B 1999;60:7149-55.

[76] Yamaguchi M, Shiga M, Kaburaki H. First-Principles Study on Segregation Energy and Embrittling Potency of Hydrogen in Ni Σ5(012) Tilt Grain Boundary. Journal of the Physical Society of Japan 2004;73:441-9.

[77] Du YA, Ismer L, Rogal J, Hickel T, Neugebauer J, Drautz R. First-principles study on the interaction of H interstitials with grain boundaries in α- and γ-Fe. Physical Review B 2011;84:144121.

[78] Mirzaev D, Mirzoev A, Okishev KY, Verkhovykh A. Ab initio modelling of the interaction of H interstitials with grain boundaries in bcc Fe. Molecular Physics 2016;114:1502-12.

[79] Baskes MI, Vitek V. Trapping of hydrogen and helium at grain boundaries in nickel: An atomistic study. MTA 1985;16:1625-31.

[80] Brass A, Chanfreau A. Accelerated diffusion of hydrogen along grain boundaries in nickel. Acta Materialia 1996;44:3823-31.

[81] Oudriss A, Creus J, Bouhattate J, Savall C, Peraudeau B, Feaugas X. The diffusion and trapping of hydrogen along the grain boundaries in polycrystalline nickel. Scripta Materialia 2012;66:37-40.

[82] Zhou H-B, Liu Y-L, Jin S, Zhang Y, Luo G-N, Lu G-H. Investigating behaviours of hydrogen in a tungsten grain boundary by first principles: from dissolution and diffusion to a trapping mechanism. Nuclear Fusion 2010;50:025016.

[83] Du YA, Rogal J, Drautz R. Diffusion of hydrogen within idealized grains of bcc Fe: a kinetic Monte Carlo study. Physical Review B 2012;86:174110.

[84] Di Stefano D, Mrovec M, Elsässer C. First-principles investigation of hydrogen trapping and diffusion at grain boundaries in nickel. Acta Materialia 2015;98:306-12.

[85] Ashby MF, Spaepen F, Williams S. The structure of grain boundaries described as a packing of polyhedra. Acta Metallurgica 1978;26:1647-63.

[86] Li S, Li Y, Lo Y-C, Neeraj T, Srinivasan R, Ding X, et al. The interaction of dislocations and hydrogen-vacancy complexes and its importance for deformation-induced proto nano-voids formation in α-Fe. International Journal of Plasticity 2015;74:175-91.

[87] Bond GM, Robertson IM, Birnbaum HK. The influence of hydrogen on deformation and fracture processes in high-strength aluminum alloys. Acta Metallurgica 1987;35:2289-96.

[88] Bond GM, Robertson IM, Birnbaum HK. Effects of hydrogen on deformation and fracture processes in high-ourity aluminium. Acta Metallurgica 1988;36:2193-7.

[89] Lee TC, Dewald DK, Eades JA, Robertson IM, Birnbaum HK. An environmental cell transmission electron microscope. Review of Scientific Instruments 1991;62:1438-44.

[90] Birnbaum HK, Sofronis P. Hydrogen-enhanced localized plasticity—a mechanism for hydrogen-related fracture. Materials Science and Engineering: A 1994;176:191-202.

[91] Sofronis P, Birnbaum HK. Mechanics of the hydrogendashdislocationdashimpurity interactions—I. Increasing shear modulus. Journal of the Mechanics and Physics of Solids 1995;43:49-90.

[92] Ferreira PJ, Robertson IM, Birnbaum HK. Hydrogen effects on the interaction between dislocations. Acta Materialia 1998;46:1749-57.

[93] Robertson IM, Birnbaum HK, Sofronis P. Chapter 91 Hydrogen Effects on Plasticity. In: Hirth JP, Kubin L, editors. Dislocations in Solids: Elsevier; 2009. p. 249-93.

[94] Troiano AR. The role of hydrogen and other interstitials in the mechanical behavior of metals. Trans ASM 1960;52:26.

[95] Oriani RA. A mechanistic theory of hydrogen embrittlement of steels. Berichte der Bunsengesellschaft für physikalische Chemie 1972;76:848-57.

[96] Oriani RA, Josephic PH. Equilibrium aspects of hydrogen-induced cracking of steels. Acta Metallurgica 1974;22:1065-74.

[97] Oriani RA, Josephic PH. Equilibrium and kinetic studies of the hydrogen-assisted cracking of steel. Acta Metallurgica 1977;25:979-88.

[98] Oriani RA. Hydrogen Embrittlement of Steels. Annual review of materials research 1978;8:30.

[99] Oriani RA. Whitney Award Lecture—1987: Hydrogen—The Versatile Embrittler. Corrosion 1987;43:390-7.

Chapter 3: Methodology

It is well recognized that the accurate hydrogen mapping in microstructures at the atomic scale is very difficult due to the low mass and high diffusivity of hydrogen. Severe premature failure induced by hydrogen can be achieved even at extremely low hydrogen concentrations, which cannot be effectively detected at the atomic scale in experiments. Therefore, spatial hydrogen mapping and temporal hydrogen tracking via experimental approaches are the two greatest challenges on the avenue to better understanding of the mechanisms of HE. With the development of computational power and the advance of computing methods, atomistic simulations are becoming valuable tools for not only investigating the interactions of hydrogen with metals, but also verifying those proposed mechanisms of HE. Therefore, in this thesis, we used the hierarchical multi-scale atomistic simulations to systematically study the interplays of hydrogen with various microstructures in metals. This chapter will provide a brief instruction in terms of computational methods and techniques we adopted in our thesis.

3.1 First principles calculations

Ab initio calculations on the basis of density functional theory is one of the most common theoretical method to describe physical properties of materials. The key idea of this method is to solve Schrödinger equation based on some important assumptions. It is well known that atoms are made up of atomic nuclei and electrons where the mass of atomic nucleus is larger than electron. Therefore, we can consider atomic nuclei as fixed points and electrons move fast around these static atomic nuclei (This is famous Born-Oppenheimer approximation). The Schrödinger equation with Born-Oppenheimer approximation can be described as [1]:

$$\left[-\sum_{n=1}^{N}\frac{\hbar^2\nabla_n^2}{2m_e}+\sum_{n=1}^{N}V_n+\sum_{n=1}^{N}\sum_{m<n}U_{n,m}\right]\Psi=E\Psi \tag{3.1}$$

where m_e is the mass of one electron, Ψ is the Schrödinger wave function and E on the right side is the ground state energy. The first term on the left side in the bracket is the kinetic energy and the second term represents electron interaction energy and the third term is the interaction energy between electron and nucleus. Although the Born-Oppenheimer approximation simplifies the original complicated Schrödinger equation by separating the whole system into atomic nuclei and electrons, it is still impossible to solve Eq. 3.1 due to the fact that a huge number of electrons participate in the system. This difficulty was finally solved based on the joint effort from Kohn, Hohenberg and Sham [2, 3]. In particular, Kohn and Hohenberg proved the first theorem that the ground state energy (i.e., E in Eq. 3.1) can be obtained by electron density alone without considering individual electrons. Then, the second theorem was proposed and gives the method to obtain the ground state energy. Namely, the ground state energy can be calculated by the minimization of the functional of electron density. Then, Kohn and Sham further simplified the Schrödinger equation and deduced the Kohn-Sham equation [3]:

$$\left[-\sum_{n=1}^{N}\frac{\hbar^2\nabla_n^2}{2m_e}+V+V_H+V_{XC}\right]\Psi=\varepsilon\Psi \tag{3.2}$$

where V is the interaction energy between electron and nuclei, V_H is coulomb interaction energy between electrons and V_{XC} is the exchange correlation energy. The ground state energy of systems can be calculated via Eq. 3.2 by performing self-consistent calculation using an initial trial electron density. In our thesis, the commercial simulation package VASP [4, 5] was used to perform all first principles calculations so as to investigate hydrogen segregation and diffusion behaviors at microstructural entities in metals. Specifically, the interaction energy between hydrogen and grain boundary and the migration barriers can be accurately calculated, providing us a clear energetic picture at the atomic scale.

3.2 Molecular dynamics simulations

Although first principles calculations are capable of obtaining very useful information at the atomic scale, it is very time-consuming to handle with complicated systems with a large number of atoms. Furthermore, the kinetic processes such as dislocation nucleation and hydrogen diffusion in larger systems are beyond the scope of first principles calculations. Therefore, other methods should be involved to overcome the limitations of first principles calculations and to simulate more complicate systems in larger scale. Fortunately, molecular dynamics simulations on the basis of the empirical interatomic potentials show strong ability to simulate very complicated system with a huge number of atoms (million atoms) without losing accuracy.

Molecular dynamics simulations are mainly based on Newton's laws of motion. In particular, Atoms in systems can be viewed as the classical particles. The motions of atoms can be described by Newton's second law:

$$F_i = m_i \frac{d^2 r_i}{dt^2} \tag{3.3}$$

where F_i is the force on atom *i*, mi is the mass of atom *i* and r_i is the position of *i*th atom. Fore F_i can be calculated by means of interatomic potential $U(r_i)$:

$$F_i = -\nabla_i U \tag{3.3}$$

In light of the aforementioned equations, the forces and interactions between atoms can be easily described and the trajectories of atom motions can be obtained. It is worth noting that the validation of the results from molecular dynamics simulations completely relies on the used empirical interatomic potential. Roughly speaking, the interatomic potential can be expressed as [6]:

$$U = \sum_i \sum_{j>i} u_1(r_i, r_j) + \sum_i \sum_{j>i} \sum_{k>j>i} u_2(r_i, r_j, r_k) + \cdots \tag{3.4}$$

where the first term shows the pair potential and the other terms are many-body potentials. It is worthy to note that there are many formats of interatomic potential and the selection of interatomic potentials depends on the research area. As for metals and alloys, the embedded atom method (EAM) potential is widely used due to the accurate description of the atomic interactions. The EAM potential can be described as [7]:

$$U = \sum_i F_i(\rho_i) + \sum_{i \neq j} \varphi(r_i, r_j) \tag{3.5}$$

where $\varphi(r_i, r_j)$ is the pair potential and $F_i(\rho_i)$ is named "embedded energy" that can be calculated by electron density ρ_i.

In this thesis, all molecular dynamics simulations were carried out by open source software LAMMPS [8]. LAMMPS is a versatile simulation package that is able to simulate large complicate systems with high efficiency. Therefore, some critical phenomena during plastic deformation or other dynamic processes can be successfully detected.

3.3 Kinetic Monte Carlo simulations

It should be noted that there still remain many limitations in molecular dynamics simulations. For example, the timescale in molecular dynamics simulations is limited to picoseconds or nanoseconds. Therefore, it is very difficult to investigate long time diffusion behaviors or microstructure evolution. Fortunately, Kinetic Monte Carlo simulations can break though the aforementioned limitations in timescale and is very suitable for studying hydrogen diffusion behaviors in metals. The diffusion process of atom in Kinetic Monte Carlo simulations can be seen as individual jump between predefined lattice positions. Each jump is determined by the hoping rate which can be calculated by migration barriers associated with this individual hopping. The whole process of Kinetic Monte Carlo simulation is listed as follows [9]: we first set the time is zero (i.e., t=0), followed by the calculation of all possible rates in system (i.e., R_{tot}). Then, we calculate the cumulative rate of atom i. Here the cumulative rate can be obtained by the summation of the possible rates of all nearest neighbor hopping paths (R_i). Next step is to choose the path to jump where the path can be determined by $R_{i-1} < \rho_0 R_{tot} < R_i$ (ρ_0 is a random number $\in (0,1]$). Now the jumping process is finished. With respect to time evolution of system, the updated time can be calculated by $t = t - \ln(\rho_1) / R_{tot}$ where ρ_1 is a random number $\in (0,1]$. By using the calculated migration barriers of hydrogen as input, long time hydrogen diffusion behaviors can be easily achieved by means of Kinetic Monte Carlo simulations, which provides some new insights toward better understanding HE at the atomic scale.

3.4 Nudged elastic band method

One critical problem in solid diffusion is the identification of the migration barriers associated with atom hops and the search of minimum energy pathways (MEP). In our thesis, we used the nudged elastic band (NEB) method [10, 11] to effectively obtain the migration barriers. In NEB method, a series of interpolated atomic configurations (i.e., images) are constructed between the initial and final stable configuration (here the initial and final stable configuration corresponds to the ground state before and after diffusion). The inserted adjacent configurations are linked by a spring to imitate an elastic band. The search of MEP can be easily achieved by the force minimization on the images. During the force minimization, the image would be dragged toward the MEP and the image at MEP with the maximum energy is the saddle point. The corresponding migration barrier can be calculated by the energy difference between the saddle point and the ground state.

3.5 References

[1] Martin ML, Robertson IM, Sofronis P. Interpreting hydrogen-induced fracture surfaces in terms of deformation processes: A new approach. Acta Materialia 2011;59:3680-7.

[2] Hohenberg P, Kohn W. Inhomogeneous electron gas. Physical review 1964;136:B864.

[3] Kohn W, Sham LJ. Self-consistent equations including exchange and correlation effects. Physical review 1965;140:A1133.

[4] Kresse G, Hafner J. Ab initio molecular dynamics for liquid metals. Physical Review B 1993;47:558-61.

[5] Brass A, Chanfreau A. Accelerated diffusion of hydrogen along grain boundaries in nickel. Acta Materialia 1996;44:3823-31.

[6] LeSar R. Introduction to computational materials science: fundamentals to applications: Cambridge University Press; 2013.

[7] Foiles S, Baskes M, Daw MS. Embedded-atom-method functions for the fcc metals Cu, Ag, Au, Ni, Pd, Pt, and their alloys. Physical review B 1986;33:7983.

[8] Plimpton S. Fast Parallel Algorithms for Short-Range Molecular Dynamics. Journal of Computational Physics 1995;117:1-19.

[9] Voter AF. Introduction to the kinetic Monte Carlo method. Radiation effects in solids 2007:1-23.

[10] Henkelman G, Jóhannesson G, Jónsson H. Methods for Finding Saddle Points and Minimum Energy Paths. In: Schwartz SD, editor. Theoretical Methods in Condensed Phase Chemistry. Dordrecht: Springer Netherlands; 2002. p. 269-302.

[11] Jónsson H, Mills G, Jacobsen KW. Nudged elastic band method for finding minimum energy paths of transitions. Classical and quantum dynamics in condensed phase simulations: World Scientific; 1998. p. 385-404.

Chapter 4: Chemomechanical Origin of Hydrogen Trapping at Grain Boundaries in FCC Metals

It is well known that hydrogen segregation and trapping at grain boundaries play the crucial role in intergranular fracture induced by hydrogen. However, the mechanism of hydrogen segregation and related intergranular failures remain poorly understood, which mainly derives from the lack of decent ways to analyze the interaction of hydrogen with grain boundaries. The first paper provided an efficient way to characterize local atomic structures of grain boundaries and to quickly identify possible hydrogen trapping sites along grain boundaries. This novel method, combined with first principles calculations, allows effective analysis of hydrogen segregation profile at grain boundaries. Our work discovered hydrogen segregation at grain boundaries strongly depends on local atomic structure. In addition, the segregation tendency can be accurately predicted by one continuum model proposed in this article.

- This chapter has been published in *Physical Reviews Letters*, shown as: **Chemomechanical origin of hydrogen trapping at grain boundaries in FCC metals**, Xiao Zhou, Daniel Marchand, David L. McDowell, Ting Zhu, and Jun Song, *Physical Reviews Letters* 2016; 116(7): 075502.

4.1 Abstract

Hydrogen embrittlement of metals is widely observed, but its atomistic origins remain little understood and much debated. Combining a unique identification of interstitial sites through polyhedral tessellation and first-principles calculations, we study hydrogen adsorption at grain boundaries in a variety of face-centered cubic metals of Ni, Cu, γ-Fe and Pd. We discover the chemomechanical origin of variation of adsorption energetics for interstitial hydrogen at grain boundaries. A general chemomechanical formula is established to provide accurate assessments of hydrogen trapping and segregation energetics at grain boundaries, and it also offers direct explanations for certain experimental observations. The present study deepens our mechanistic understanding of the role of grain boundaries in hydrogen embrittlement, and points to a viable path towards predictive microstructure engineering against hydrogen embrittlement in structural metals.

4.2 Introduction

Despite drastic technological advances in the development of polymers and composites in the past several decades, metals remain the irreplaceable backbone in many important applications for automotive, aerospace and energy industries. However, metals are typically susceptible to environmental attack. One prominent example is hydrogen embrittlement (HE) that can result in sudden and catastrophic failure of metallic components and systems [1]. Hydrogen is abundant in service environments and manufacturing processes. As a result, HE poses a significant threat to load-bearing metallic components and is often considered as a major obstacle to the reliable applications of structural metals. Despite considerable effort in the study of HE [2-15], the dominant physical mechanisms of HE remain controversial [16, 17]. Hence, the study of HE at the atomistic and electronic levels may illuminate the mechanistic origin of HE and thus enable the development of effective means to mitigate HE. Moreover, the influence of hydrogen on dislocation migration can be distinguished from its role in grain boundary (GB) segregation and compromise of fracture resistance. We focus on the latter here.

Hydrogen adsorption is favored at microstructural heterogeneities [18], such as GBs, as opposed to in interstitial sites in the bulk lattice. Recently, Bechtle et al. [19] conducted experiments on GB-engineered Ni samples with and without hydrogen, and their results showed that the susceptibility of HE can be drastically redued at special GBs that are characterized with low excess free volumes and a high degree of atomic matching. In addition, Oudriss et al. [20] showed that special GBs can trap hydrogen and reduce hydrogen diffusion. These studies highlight the important role of GBs in influencing hydrogen transport and embrittlement behaviors, and suggest the possibility of controlling the susceptibility of structural metals to HE through GB engineering.

To advance rational GB engineering, it is essential to characterize the GBs and associated hydrogen segregation behaviors in a systematic and quantitative manner. The structure of certain high angle tilt GBs is commonly described by the Coincidence Site Lattice (CSL) model [21]. Alternatively, the GB structure can be represented by a periodic array of nested three-dimensional (3D) structural units [22, 23], which are associated with CSL boundaries but also pertain to general high angle tilt grain boundaries. Along this line of approach, Ashby et al. [24] showed that there exist eight unique convex polyhedrons with triangle faces (i.e., so-called deltahedra) to account for all possible basic packing units at a tilt GB. This approach enables the characterization of GBs with a simple, yet powerful, concept of geometric packing unit, which can be applied to investigate many structural and chemomechanical properties of GBs, such as interstitial impurity segregation at GBs [25, 26].

Here we develop a novel modeling approach that combines the space tessellation of polyhedral packing units and first principles density functional theory (DFT) calculations for studying the hydrogen segregation at GBs in structural metals. Using several face-centered cubic (FCC) metals, including Ni, Cu, γ-Fe and Pd as representative systems, we demonstrate that the polyhedral packing units at GBs can be uniquely identified and their central holes are shown to serve as favorable interstitial sites of hydrogen adsorption. Our DFT calculations reveal a universal dependence of hydrogen adsorption energies on the local volume deformation of polyhedral packing units in all four FCC metals studied. To uncover its physical origin, we establish a general formula involving a minimum number of first principles input and fitting parameters that closely matches all DFT data of hydrogen adsorption energies at GBs in four different FCC metals. Such a general result illuminates the chemomechanical origin of hydrogen segregation at GBs. The physical meaning of the parameters in the formula is clarified. Our results thus provide mechanistic insights towards predictive GB engineering to support the development of HE-resistant metals.

4.3 Computational methodology

First-principles density functional theory (DFT) calculations were performed using the Vienna *ab initio* Simulation Package (VASP) [27, 28] on the basis of the density functional theory (DFT) with the projector augmented wave method (PAW) [29, 30]. The generalized gradient approximation (GGA) [31] with the Perdew-Burke-Ernzerhof exchange-correlation (PBE) [32] functional, and the first-order Methfessel-Paxton scheme with a smearing of 0.05 eV were implemented in the calculations. A k-point grid of 3×1×5 and a cut-off energy of 400 eV were used and shown to yield sufficient accuracy. Structural relaxation was considered converged when atomic force was less than 0.01 eV/Å. During relaxation, atoms were allowed to move freely except for the atoms in the surface layers whose motions were constrained to be perpendicular to the GB only. A vacuum space of 10 Å in thickness exists between surfaces to eliminate interactions between surfaces. We focused on symmetric tilt GBs in the present study, yet several non-symmetric GBs were also investigated for the purpose of *proof-of-concept* or when looking for certain polyhedrons.

In our calculations, the zero point energy (ZPE) correction was not included due to the high computational cost. However, preliminary studies with ZPE correction were performed, showing that ZPE does not affect our results (*albeit* possibly overall a small shift for energetics that does not change the trend).

4.4 Results and discussion

We have studied a number of symmetric tilt GBs with various mis-orientations in the FCC metals of Ni, Cu, γ-Fe and Pd. Among these GBs, five types of polyhedrons are involved, i.e., tetrahedron (TET), octahedron (OCT), pentagonal bipyramid (PBP), cap trigonal prism (CTP) and bi-tetrahedron (BTE) [24], as illustrated in Figure 4.1 for a representative Σ 5(130)[100] GB (meaning the (130) GB face with a [100] tilt axis) in Ni. We identified these polyhedrons by space tessellation [33]. Energy minimization from DFT calculations indicates that there is only one interstitial site of hydrogen adsorption in each polyhedron, which lies closely to the centroid of the polyhedron. This is consistent with the Switendick criterion based on the minimum H-H distance [34]. Hence, the center of each polyhedron corresponds to an individual hydrogen adsorption site at the GBs. In other words, one can identify potential hydrogen adsorption sites along GBs using a geometric approach of space tessellation of polyhedral packing units without a detailed knowledge of hydrogen adsorption chemistry.

After the identification of hydrogen adsorption sites at GBs through space tessellation of polyhedral packing units, we performed DFT calculations to evaluate the interactions between hydrogen and GBs in terms of adsorption energetics. Figure 4.2 shows the differential charge density of Σ5(130)[100] Ni GB projected along the (100) plane (see details in section 4.7 for similar plots of other FCC metals studied). These results indicate that the interactions between hydrogen and the host atoms are dominantly localized at GBs, and hence the adsorption energy can be primarily determined by the local environment of the *capsule*, i.e., the polyhedron enclosing the hydrogen atom.

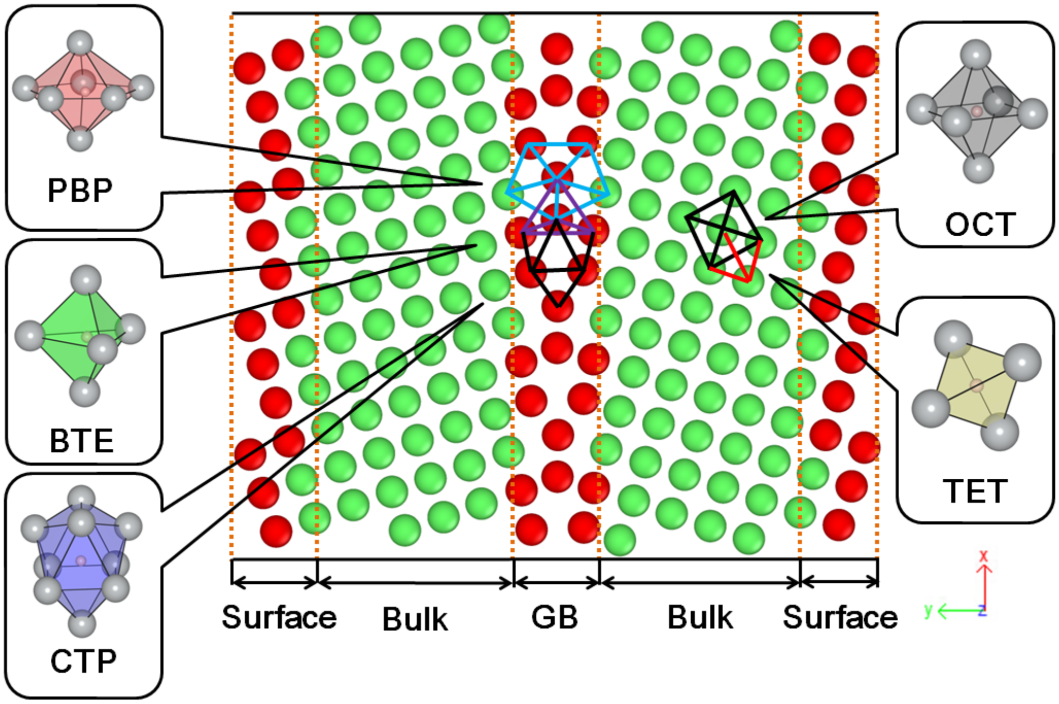

Figure 4.1. (color online): Schematic illustration of polyhedron in representative $\Sigma 5(130)[100]$ GB and bulk lattice. The grey ball in distinguished polyhedron represents host Ni atom and the small pink ball in center is hydrogen atom.

The adsorption energy of hydrogen, E^{ad}, is defined as

$$E^{ad} = E_H^{GB} - E^{GB} - E_{iso}^H \tag{4.1}$$

where E^{GB} and E_H^{GB} are the total energies of the system before and after adsorption of one hydrogen atom, respectively, and E_{iso}^H is the energy of one isolated hydrogen atom in vacuum. Based on Eq. 4.1, we calculated the hydrogen adsorption energies for different polyhedral sites for a series of symmetric tilt GBs (elaborated in details in section 4.7) in Ni, Cu, γ-Fe and Pd, as plotted in Figure 4.3. Clearly, the hydrogen adsorption energies E^{ad} depend largely on the type of polyhedral interstitial site, i.e., the average values of E^{ad} differ for different types of polyhedra. Moreover, for each type of polyhedral interstitial site, the values of E^{ad} vary markedly. Hence, the polyhedron is not sufficient alone to uniquely determine the interactions between hydrogen and GBs.

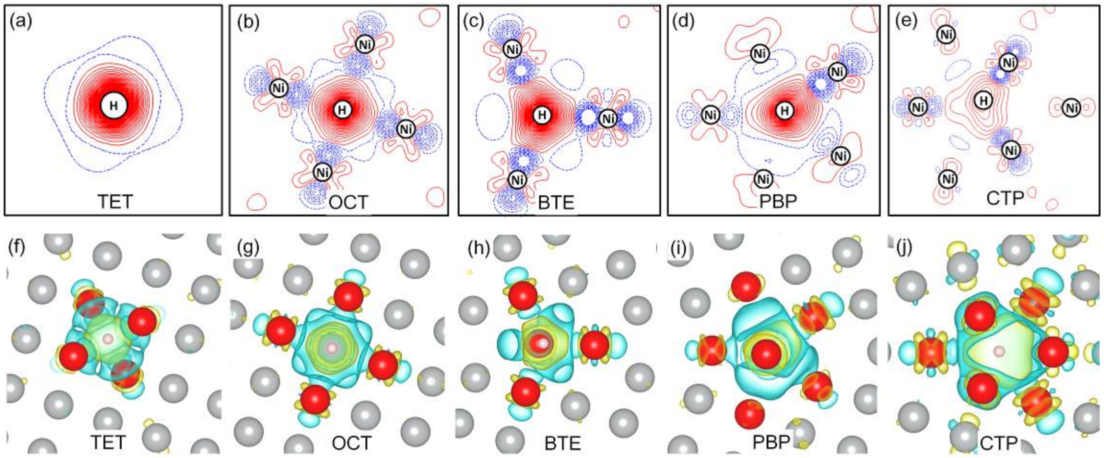

Figure 4.2. (color online): Differential charge density of $\Sigma 5(130)[100]$ Ni GB projected on the (100) plane, with (a)-(e) being two dimensional while (f)-(j) being three dimensional charge density contours. In (a)-(e), the blue dash line represents electron depletion and the red solid line signifies electron accumulation. In (f)-(j), the red spheres represent Ni atoms locating at the vertices of the polyhedron that encloses the hydrogen atom, indicated by the small pink sphere, while the grey spheres represent other Ni atoms. Blue region represents electron depletion while yellow region signifies electron accumulation.

To understand the large variation of E^{ad}, we examined the local deformation of polyhedrons at GBs. A parameter, dV_p / V_p^0, is used to measure the local volume changes (dilatation) of polyhedrons. Here, V_p^0 is the volume of the pristine polyhedron, which is defined as the corresponding deltahedron with the edge length being the nearest-neighboring distance, $\sqrt{2}a_0 / 2$, where a_0 denotes the equilibrium lattice constant in the bulk FCC lattice; further, $dV_p = V_p - V_p^0$ measures the deviation of the actual polyhedron volume V_p from V_p^0.

We plot dV_p / V_p^0 together with E^{ad} in Figure 4.3. A clear correspondence between the variations in the E^{ad} and dV_p / V_p^0 data can be observed for all four FCC metals studied.

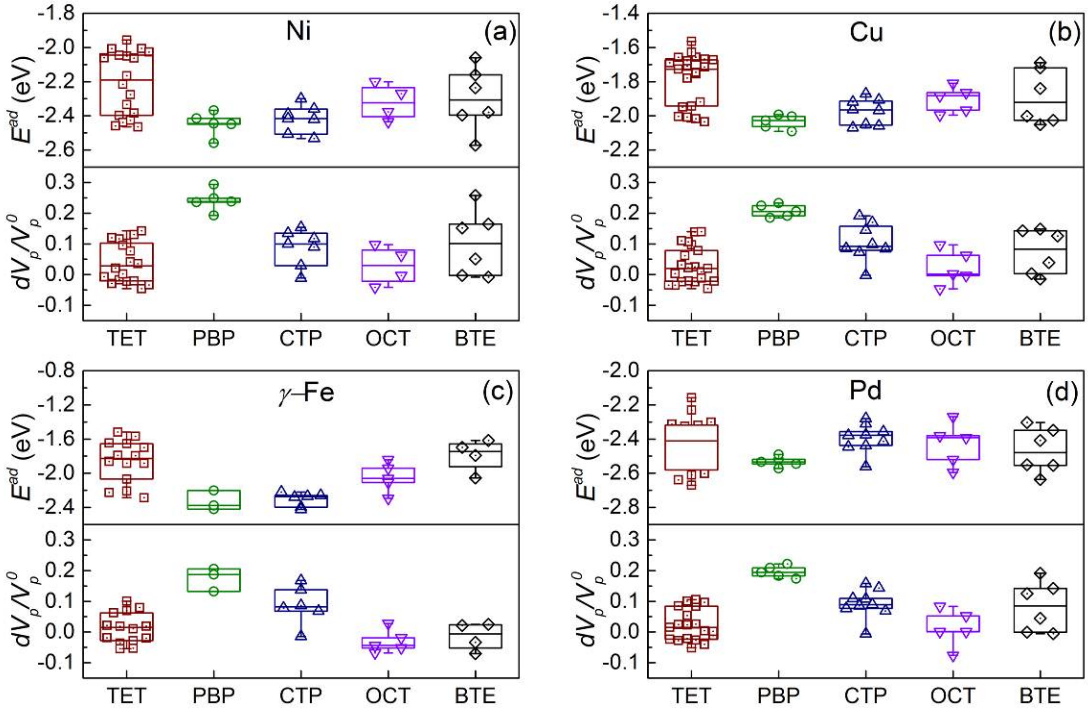

Figure 4.3. (color online): The variation in the hydrogen adsorption energy E^{ad} and normalized lattice dilatation dV_p/dV_p^0 of polyhedrons in (a) Ni, (b) Cu, (c) γ-Fe, and (d) Pd systems.

The intriguing correspondence shown in Figure 4.3 suggests that the variation of E^{ad} is dictated by the local volume changes of polyhedral packing units. To elucidate the physical origin of such a correspondence, we note that the mechanical interaction energy between a GB and an interstitial point defect can be determined by evaluating the work of $P\Omega_p$, which corresponds to the local pressure P in the absence of point defects times the lattice expansion (i.e., partial volume) Ω_p occurring due to interstitial insertion of a point defect [14, 35]. For the present case of hydrogen adsorption at the polyhedral interstitial site, the partial volume Ω_p

should be the volume change associated with hydrogen adsorption at the polyhedral interstitial site, and the local pressure P is determined by the volume change dV_p / V_p^0 according to

$$P = -B \frac{dV_p}{V_p^0} \tag{4.2}$$

where B is the bulk modulus (see Table 4.1). We note that the bulk modulus of the lattice is an approximation of the local bulk modulus pertaining to GB regions, owing to the differences in atomic coordination and bond lengths, but is used here as a first-order approximation. Consequently the mechanical interaction energy between the hydrogen and polyhedral packing unit is estimated as

$$dE^{ad} = -B\Omega_p \frac{dV_p}{V_p^0} \tag{4.3}$$

Using Eq. 4.3, we can express the adsorption energy of a hydrogen atom in a polyhedron packing unit at a GB in terms of

$$E^{ad} = E_0^{ad} - B\Omega_p \frac{dV_p}{V_p^0} \tag{4.4}$$

where E_0^{ad} is the chemisorption energy of hydrogen in a deltahedron (i.e., a pristine polyhedron as defined earlier). Eq. 4.4 explicitly reveals the dependence of hydrogen adsorption on the chemisorption energy and the mechanical interaction energy, the latter of which is governed by the partial volume of hydrogen insertion and the local volume deformation of the polyhedral structural unit at GBs. In Figure 4.4, the fitting curves (dashed lines) based on Eq. 4.4 overall agrees very well with the data points of adsorption energies from DFT calculations. This good agreement also directly explain the correspondence between the variations in the E^{ad} and dV_p / V_p^0 data as observed in Figure 4.3. There are, however, noticeable deviations between some of the first principles data and model predictions in the case of γ-Fe. Such deviations are primarily attributed to our assumption of the isotropic volumetric deformation of polyhedrons in the model (cf. Eq. 4.4) while the actual polyhedron distortion can be anisotropic (elaborated in details in section 4.7). This suggests the need of a further study to investigate the effect of deformation anisotropy of polyhedrons for improving the model, which will be pursued in the future.

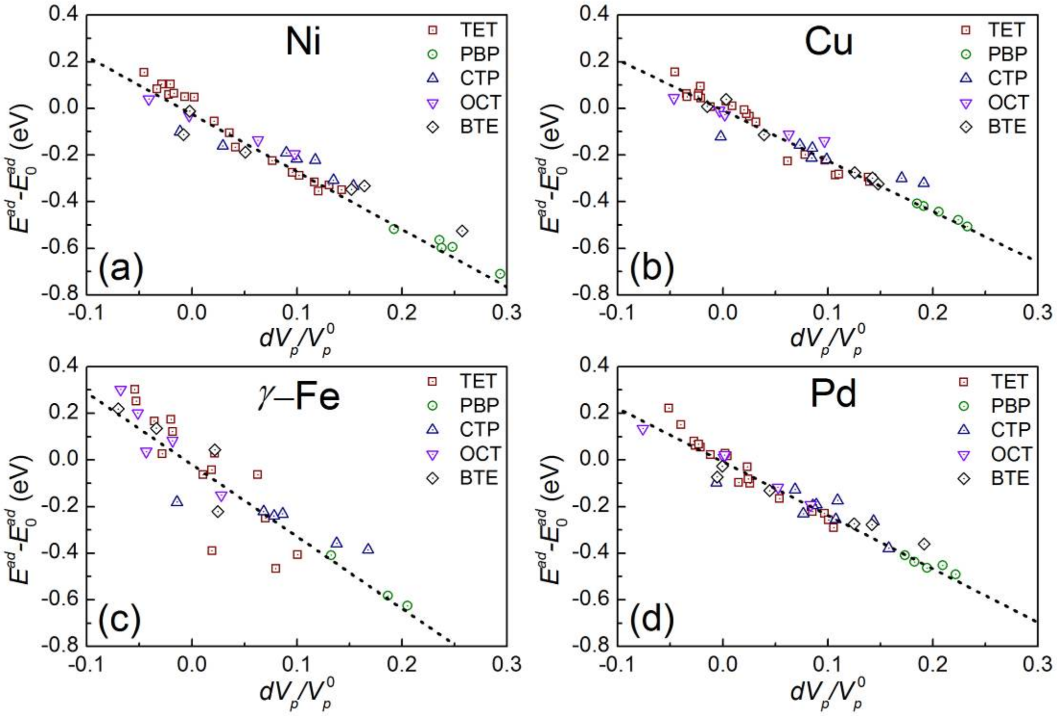

Figure 4.4. (color online): Comparison between the DFT calculated (open symbols) and model predicted (dash lines) adsorption energetics versus volume distortion relation in (a) Ni, (b) Cu, (c) γ-Fe, and (d) Pd systems.

Here for simplicity yet without loss of generality, we take a single value of partial volume Ω_p for all polyhedrons, given an FCC metal studied. The fitting parameters of E_0^{ad} and Ω_p are listed in Table 4.1. The close agreement between the DFT data and the predictions based on Eq. 4.4 shown in Figure 4.4 demonstrates that Eq. 4.4 captures the dominant chemomechanical effects of hydrogen adsorption and segregation at GBs. In Eq. 4.4, E_0^{ad} can be regarded as an intrinsic property of pristine polyhedrons associated with chemisorption of hydrogen, which can be separately determined (other than the GB calculations). The pristine TETs and OCTs are commonly present in a bulk FCC lattice and the pristine BTEs are basic constituents of coherent twin boundaries, and the corresponding hydrogen adsorption energies can be readily evaluated. These data, also listed in Table 4.1, are in close agreement with the E_0^{ad} values obtained from the previous GB calculations. This validates the treatment of E_0^{ad} as a material constant. Incidentally, the pristine PBP and OCT polyhedrons are not present in the GB structures examined in the present study. Nonetheless we suggest the possible methods (elaborated in details in section 4.7) by which one might construct pseudo-pristine PBP and OCT polyhedrons to compute the corresponding values of E_0^{ad}. In addition, we note that in Table 4.1, OCT (the polyhedron responsible for H adsorption in bulk lattice) exhibits the lowest E_0^{ad} among all five polyhedrons. Besides E_0^{ad}, the partial volume of hydrogen adsorption at GBs, Ω_p, is another important parameter in Eq. 4.4. Interestingly, the value of Ω_p obtained is nearly identical to the partial volume of a hydrogen interstitial in the bulk lattice (see Table 4.1). Hence, hydrogen induces similar dilatation both at the GB and in the bulk (elaborated in details in section 4.7).

Table 4.1. List of material properties, i.e., bulk modulus (B), bulk hydrogen partial volume (Ω), predicted hydrogen partial volume at polyhedrons (Ω_p), model predicted (and DFT calculated) adsorption energy of hydrogen in a pristine polyhedron, i.e., [Model] E_0^{ad} ([DFT] E_0^{ad}), in examed material systems.

Properties \ System		Ni	Cu	γ-Fe	Pd
B (GPa)		195	137	281	168
Ω (Å^3)		2.28	2.68	2.07	2.42
Ω_p (Å^3)		2.03	2.54	1.76	2.19
[Model] E_0^{ad} ([DFT] E_0^{ad}) (eV)	TET	-2.11 (-2.06)	-1.72 (-1.72)	-1.82 (-1.87)	-2.38 (-2.35)
	OCT	-2.24 (-2.26)	-1.86 (-1.85)	-2.14 (-2.18)	-2.40 (-2.38)
	BTE	-2.05 (-2.04)	-1.73 (-1.70)	-1.83 (-1.79)	-2.27 (-2.30)
	PBP	-1.85	-1.59	-1.79	-2.06
	CTP	-2.20	-1.75	-2.04	-2.18

Eq. 4.4 provides a predictive model for evaluating the energetics of hydrogen trapping and segregation at GBs. It is important to point out that this model is a very general, physics-based model. Besides the FCC metal systems, the model is also expected to be applicable to metals of other crystal structures (e.g., HCP and BCC). Some preliminary calculations have been performed using BCC Nb as an example to demonstrate the generality of the model (elaborated in details in section 4.7). In light of recent experiments [19, 20, 36, 37] on hydrogen embrittlement, several case studies of hydrogen embrittlement of GBs were performed (elaborated in details in section 4.7). Eq. 4.4 enables a quick evaluation of tendency of hydrogen segregation at GBs. For instance, the $\Sigma 3$ and $\Sigma 3^n$ families (i.e., the “special” GBs defined in [19] and discussed earlier in this paper) and $\Sigma 11$ GB exhibit a lack of volume changes of

polyhedral structural units. As a result, they are unfavorable to hydrogen trapping and thus less prone to hydrogen embrittlement in terms of less decease of work of separation of GBs. In contrast, other GBs with high sigma numbers, such as $\Sigma17$ and $\Sigma73$, involve substantial volume changes of polyhedral structural units and are more susceptible to hydrogen trapping and accumulation, thus giving rise to more severe embrittlement effects (elaborated in details in section 4.7) This trend is consistent with the experimental observations of hydrogen embrittlement effects on GB-engineered Ni [19] where Ni samples consisting of high density special boundaries (i.e., principally $\Sigma3$ twin boundaries) are demonstrated to exhibit good HE resistance.

Moreover, our study suggests a mechanistic pathway for further study of the GB effects on hydrogen embrittlement. First, with polyhedrons as atomic structural units of the metal lattice, the diffusion of hydrogen can be considered as discrete hops between neighboring polyhedra. Given the highly localized interactions between hydrogen and GBs, the jumping trial frequency and migration barrier would presumably depend on the coupling of neighboring polyhedra and their associated dilatation. Recognition of such localized interactions will enable the characterization of the complete diffusion parameters through a finite set of calculations, thus greatly facilitating the study of kinetics of hydrogen migration at GBs. Second, the present study calls for a rigorous continuum micromechanical study on the deformation fields of GBs, e.g., through the generalized Peierls–Nabarro model that treats the atomic interaction right at the GB interface and the continuum elastic interaction for the rest of system [38, 39]. This will enable the prediction of volume distortion, dV_p / V_p^0 at GBs directly from continuum micromechanics, and thus reduce the need of intensive first principles calculations, besides the intrinsic properties of polyhedrons, such as E_0^{ad} and Ω_p. As such, Eq. 4.4, in conjunction with the aforementioned analyses, would provide a full-scale predictive framework to quantitatively guide the GB engineering against hydrogen embrittlement.

4.5 Conclusions

In summary, we study the energetics of hydrogen adsorption for a variety of GBs structures by combining the space tessellation of polyhedral packing units and the first principles calculations. We further develop a physics-based, predictive model, as given by Eq. 4.4, to reveal the chemomechanical origin of hydrogen trapping and segregation at GBs. This model is validated through the quantitative evaluation of hydrogen adsorption energies as a function of volumetric deformation of polyhedral structural units at GBs for several FCC metals. Our results advance the atomic-level understanding of the role of GBs in hydrogen embrittlement, and provide mechanistic insights that may enable predictive GB engineering against hydrogen embrittlement. Such insights can be also fed into the study of hydrogen adsorption kinetics and fracture mechanics for advancing our understanding of hydrogen-assisted GB decohesion or cracking.

4.6 Acknowledgements

J.S. acknowledges the financial support from McGill Engineering Doctoral Award and National Sciences and Engineering Research Council (NSERC) Discovery grant (grant # RGPIN

418469-2012). D.L.M. and T.Z. acknowledge support from QuesTek to study hydrogen effects in metals. Z.X. acknowledges the financial support from China Scholarship Council (CSC). We also acknowledge Supercomputer Consortium Laval UQAM McGill and Eastern Quebec for providing computing power.

4.7 Supplementary Information

4.7.1 Space tessellation algorithm for quick identification of polyhedrons

A space tessellation algorithm based on 3D Voronoi diagram [33] was developed to enable quick division of the lattice into convex deltahedron units. The algorithm first computes the locations of all the vertex points of the Voronoi polyhedrons enclosing the host atoms. For each vertex point, the host atoms that neighbor it (within a cut-off distance) are identified. Then with the vertex point approximated as the polyhedron center, Voronoi diagrams are constructed to determine possible polyhedron configurations. The above process is illustrated in Figure 4.5. One main challenge in the above algorithm is that there are degenerated Voronoi cell vertices [40], i.e., multiple vertex points being in close vicinity of each other (the red circle, as shown in Figure 4.5a). Herein, we introduce a simple method to consolidate degenerated points, i.e., all vertex points with mutual separations within a certain cut-off distance are "*fused*" into a single point (e.g., a cut-off distance of 1.30 Ǻ is chosen for the Ni system). This approach is schematically illustrated in Figure 4.5b. The central idea behind the above tessellation algorithm is that the vertices of Voronoi cells, after consolidation to eliminate degeneracy, effectively serve as the vertices of polyhedrons.

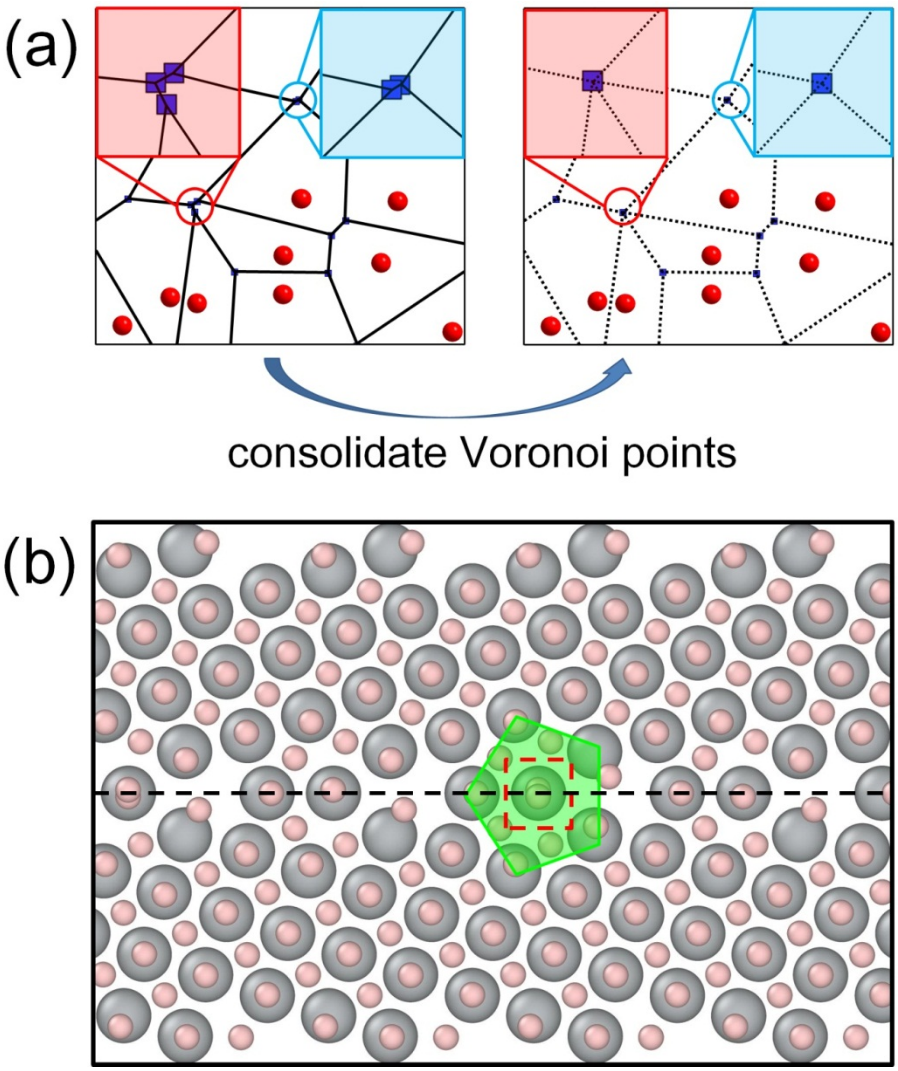

Figure 4.5. (a) A schematic illustration of the consolidation process of degenerated Voronoi vertices. The subfigure on the left shows a raw Voronoi tessellation plot where the red spheres indicate seed points, the small black squares and solid black lines indicate the resultant vertices and line segments. The red and cyan circles indicate two sample regions where degeneration of Voronoi vertices occur, with the red-shaded and cyan-shade squares respectively showing their zoom-in views. The subfigure on the right shows the plot after the consolidation process. (b) A projection view of $\Sigma 5(130)[100]$ GB where the large grey spheres represent host atoms and the pink balls represents the Voronoi vertices resulted from space tessellation. The red dashed square encloses a region where the degeneration of Voronoi vertices occurs. Those degenerated vertices within the red dashed square are subsequently "fused" into a single point following the process outlined in (a). The green-shaded polygon indicates a pentagonal bipyramid (PBP) from the space tessellation algorithm.

4.7.2 Material properties of bulk lattices

Prior to GB calculations, DFT calculations were performed to obtain the essential material properties of the bulk lattice. A 3×3×3 periodic supercell containing 108 host atoms was used in these calculations. Table 4.2 lists the values of equilibrium lattice constant (a_0), bulk modulus (B) and partial volume (Ω), for different materials (i.e., Ni, Cu, FCC-Fe and Pd). Those values are in good agreement with data in literatures, as shown in Table 4.2.

Table 4.2. Essential material properties, i.e., equilibrium lattice constant (a_0), bulk modulus (B) and partial volume (Ω) for Ni, Cu, γ-Fe and Pd.

	Ni	γ-Fe	Cu	Pd
a0 (Å)	3.52	3.46	3.64	3.95
Ref.	3.52[41];3.53[42];3.38[43];3.47[44]	3.45[45]	3.65[42];3.47[43];3.56[44]	3.96[42];3.79[43];3.83[44]
B(GPa)	195	281	137	168
Ref.	186[46];221[42];265[43];192[47]	314[48]	117[42];192[43];137[44]	171[42];232[43];181[44]
Ω (Å^3)	2.28	2.07	2.68	2.42
Ref.	2.20[49]; 3.30[50]; 2.30[47]	-	-	2.47[49]

4.7.3 Predictive modeling of hydrogen adsorption energetics

4.7.3.1 Localization of hydrogen-lattice interactions

As mentioned in previous section, the hydrogen-lattice interactions are strictly local and thus the adsorption energy is solely determined by the local environment of the polyhedron that encloses the hydrogen atom. The localization was demonstrated via the differential charge density plots in Figure 4.2 for Ni. Similarly for other material systems, i.e., Cu, γ-Fe and Pd, the localization was also observed, illustrated in Figure 4.6 below.

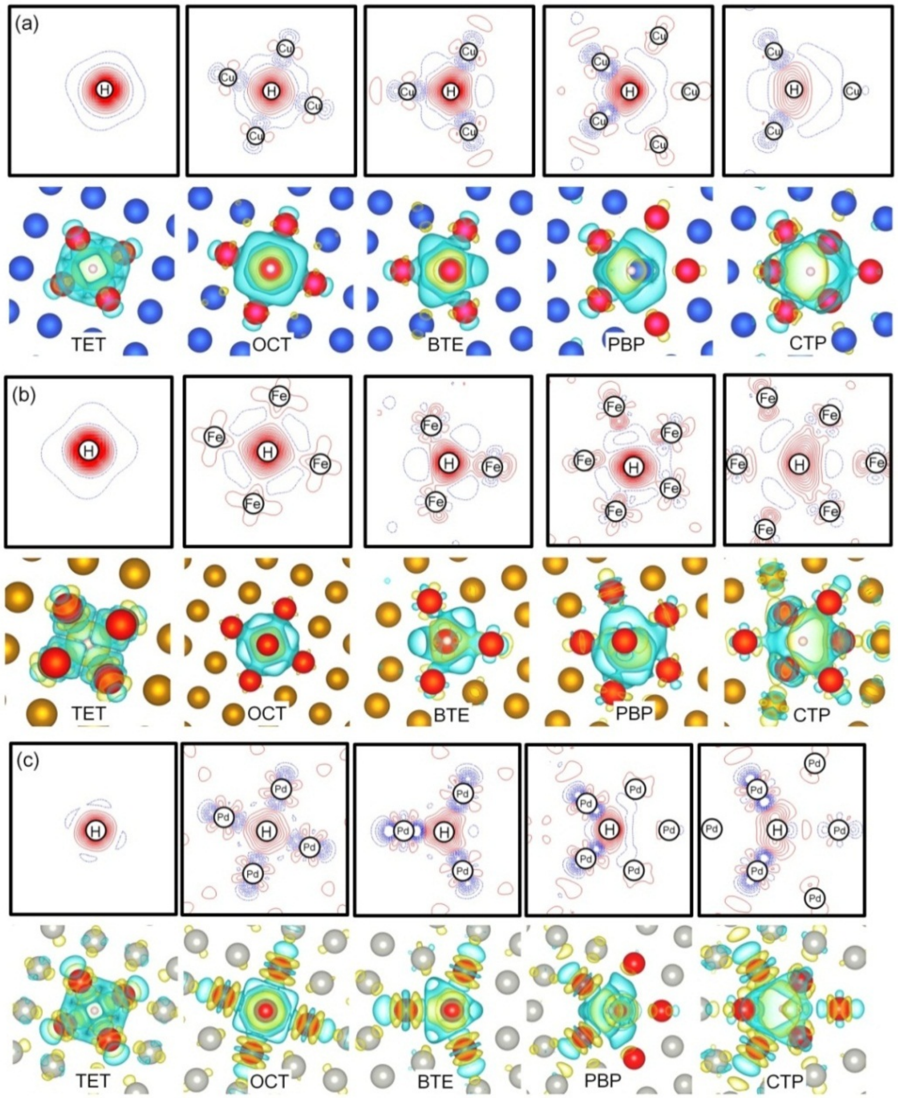

Figure 4.6. 2D and 3D differential charge density plots of $\Sigma 5(130)[100]$ GB projected on the (100) plane for (a) Cu, (b) γ-Fe, and (c) Pd. The blue dash and red solid lines in the 2D plots represent electron depletion and electron accumulation respectively. In the 3D plots, blue isosurface and yellow isosurface are electron depletion and electron accumulation, respectively. The small pink spheres are hydrogen atoms and big red spheres are metal atoms at polyhedron vertices. The big gray spheres represent other metal atoms surrounding the polyhedron.

4.7.3.2 Determination of model parameters

Applying the proposed analytical model to the E^{ad} vs dV_p / V_p^0 data for all polyhedrons, the model parameters Ω_p and E_0^{ad} can be determined. The global least-squares method [51] was employed, and from respectively the slope and intercept values Ω_p and E_0^{ad} can be determined. Meanwhile as mentioned in the main text, E_0^{ad} is an intrinsic property of the pristine polyhedron and thus can be determined separately, while can then be used to validate the analytical model. The validation can readily performed for polyhedrons TET, OCT and BTE, the pristine forms of which are available in bulk lattice and we have demonstrated in the main text that the two sets of data (i.e., the ones from fitting and the ones separately computed) show excellent agreement. On the other hand, the pristine PBP and CTP polyhedrons are not available (at least in all the GB structures examined in the present study).

In our preliminary pursuit to tackle this challenge, we found that one possible route to construct *pseudo*-pristine PBP and CTP polyhedrons, using which the corresponding E_0^{ad} values can be determined. Below we outline two potential means attempted for the construction of those *pseudo*-pristine polyhedrons.

1) **Method #1**: A standing-alone pristine polyhedron with atoms sitting at vertices and the edge length being $\sqrt{2}a_0 / 2$ is built, following which extra metal atoms are introduced to add in the region surrounding the polyhedron. In particular, one atom will be added one top of each polyhedron surface. These extra atoms form a “shell” enclosing the polyhedron in the core. The resultant configuration is then optimized with a minimal interatomic separation of $\sqrt{2}a_0 / 2$ enforced. The afore-mentioned shell construction may be repeated to build several shells. A hydrogen atom is then introduced into the polyhedron and the whole system is then relaxed (with atoms in the outmost shell fixed while other atoms free to move) to obtain the hydrogen

adsorption energy (as the value for E_0^{ad}). Two sample constructions (for PBP and CTP) are illustrated in Figure 4.7. The number of shells and the details of how each shell is constructed depend on the convergence and polyhedron stability during the relaxation process;

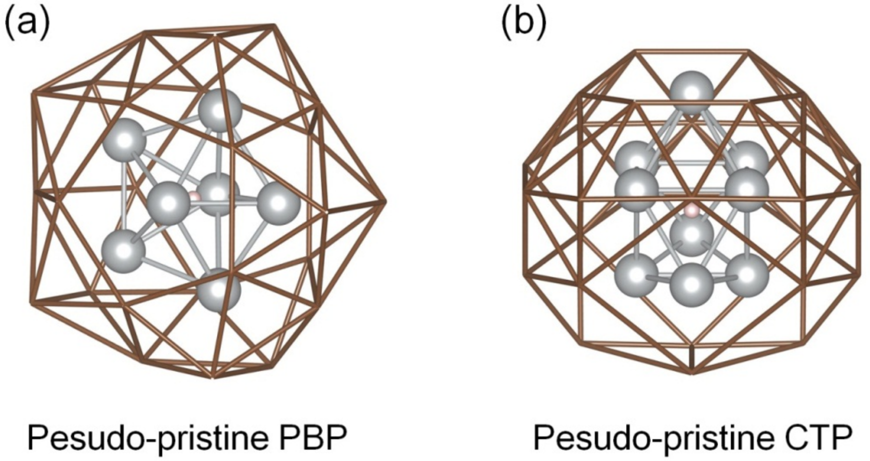

Figure 4.7. Sample construction of *pseudo*-pristine (a) PBP and (b) CTP polyhedron configurations. The grey spheres represent atoms at the pristine polyhedron vertices while the small pink spheres represent the hydrogen atom enclosed in the polyhedron; while the brown bonds denote the bonds between atoms in the outer shells surrounding the polyhedron.

2) **<u>Method #2</u>**: Given than distorted PBP and CTP exist along certain GBs, another way to construct the pseudo-pristine polyhedron is to carve out a region with the polyhedron of interest in the center. A displacement field can then be applied to the carved-out cluster to “revert” the distortion so as to transform the polyhedron into its pristine form. Then a hydrogen atom can be introduced to compute the hydrogen adsorption energy (as the value for E_0^{ad}) – again with the outmost atoms fixed while other atoms free to move. For this method, the challenge is to properly determine the size of the carve-out region and systematically define the displacement field. We can see that the above two methods of *pseudo*-pristine polyhedron construction are

rather *ad-hoc* in nature, which definitely necessitates detailed studies to grant a consistent and reliable construction - this will be tackled in our future studies.

The E_0^{ad} data obtained using the *pseudo*-pristine polyhedrons are shown in Figure 4.8, in comparison with the data obtained from fitting (see Table 4.1) from which we can see that despite being somewhat scattered they are in reasonable agreement with the values obtained from GB simulations. One exception is the PBP polyhedron in Pd, where large deviation between E_0^{ad} values (from fitting and the *pseudo*-pristine approach) can be observed. This discrepancy may originate from the fact that Pb has the largest lattice constant (3.954 Å), which results in very large volumes for PBP and CTP, then prevent the hydrogen atom from settling in an optimum state when a non-periodic cluster model is used in the DFT calculation.

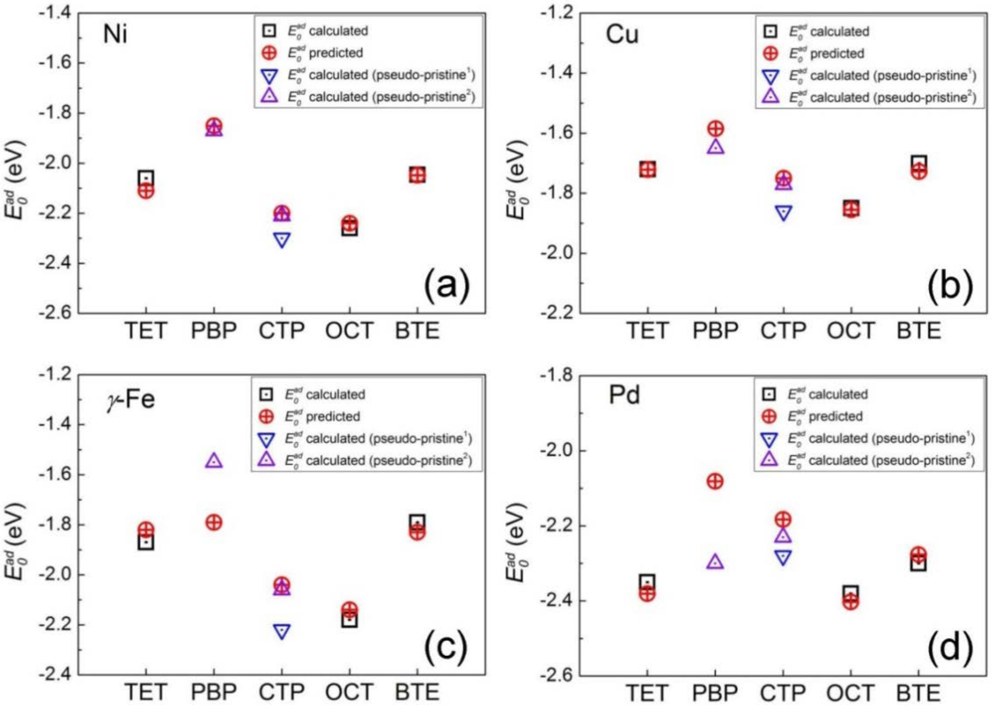

Figure 4.8. Comparison between the predicted E_0^{ad} values obtained from the GB data (i.e., E_0^{ad} predicted, red open circles), predicted E_0^{ad} values for pristine polyhedrons in bulk lattice

(i.e., E_0^{ad} calculated, black solid squares, for TET, OCT and BTE polyhedrons), and pristine polyhedrons using the pseudo-polyhedron construction (i.e., E_0^{ad} calculated [pseudo-pristine^n], for PBP and CTP polyhedrons, with n = 1 or 2 indicated the construction methods #1 or #2 respectively), for (a) Ni, (b) Cu, (c) γ-Fe and (d) Pd.

4.7.4 Role of deformation anisotropy

As noted in Figure 4.4c, somewhat deviations between some of the first principles data and model predictions are observed in the case of γ-Fe. Such deviations can be primarily attributed to the fact that isotropic volumetric deformation of polyhedrons is assumed in the proposed model (cf. Eq. 4.4). This isotropic assumption is a first-order approximation of the actual polyhedron distortion that can be anisotropic. The effect of anisotropy can however be significant, particularly for polyhedrons of small volumes (e.g., tetrahedrons). Using the tetrahedrons as the representative group, we have studied the role of anisotropy.

The degree of anisotropy of polyhedron distortion (denoted as ζ in Eq. 4.5 below) can be analyzed using the concept of quadratic elongation proposed by Robinson et al. [52],

$$\zeta = \frac{1}{n}\sum_{i=1}^{n}\left(\frac{d_i}{d_0}\right)^2 - 1 \tag{4.5}$$

where n is the number of vertices, d_i is the center-to-vertex distance of the distorted tetrahedron, and d_0 is the center-to-vertex distance of the reference tetrahedron of the same volume. A large value of ζ indicates a high anisotropy in deformation.

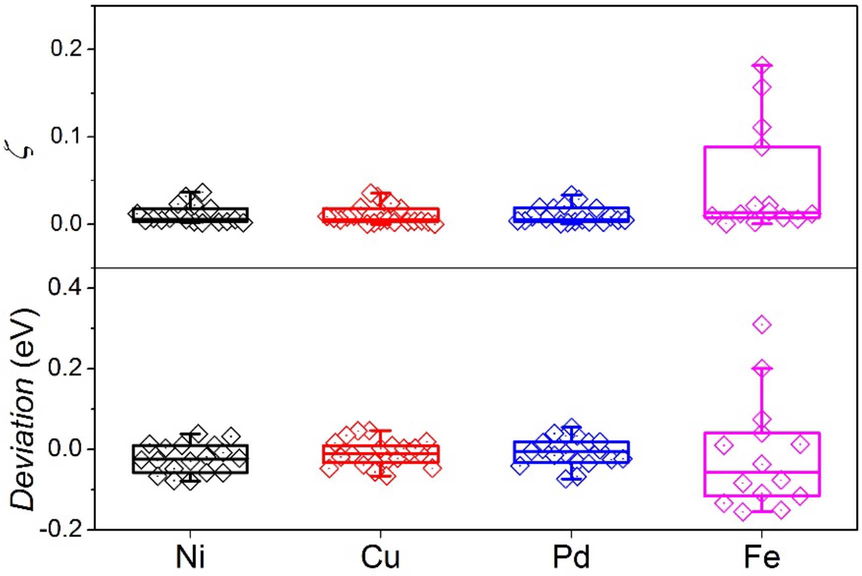

Figure 4.9. The variation in the anisotropic parameter ζ and deviation (i.e., the difference between simulated and predicted values of $E^{ad} - E_0^{ad}$) for tetrahedrons in energy in (a) Ni, (b) Cu, (c) Pd, and (d) γ-Fe.

The ζ data together with the deviation, defined as the difference between simulated and predicted values of $[\mathrm{E}^{\mathrm{ad}} - \mathrm{E}_0^{\mathrm{ad}}]$ are shown in Figure 4.9. As noted by the referee, somewhat large deviation is observed for γ-Fe, while deviation is rather small for Ni, Cu and Pd. Such characteristics are directly reflected by the ζ data. The above analysis suggests that the noticeable deviation in the case of γ-Fe arises from the high anisotropy in the distortion of polyhedrons. In view of the important role of anisotropy, one may rewrite the formula in Eq. 4.4 as

$$E^{ad} = E_0^{ad} - \Omega_p f\left(C_{ij}, \varepsilon_{ij}\right) \tag{4.6}$$

where the term of $B(dV_p/V_p^0)$ in Eq. 4.4 is replaced by a function of $f(C_{ij}, \varepsilon_{ij})$ that depends on the stiffness tensor C_{ij} and local strain tensor ε_{ij}. The function of $f(C_{ij}, \varepsilon_{ij})$ accounts for the effect of deformation anisotropy of polyhedrons and its explicit expression requires a systematic study in the future. In our future studies, we will work towards identifying the appropriate means to quantify the anisotropy and determining the functional form of $f(C_{ij}, \varepsilon_{ij})$.

4.7.5 Hydrogen segregation analysis

The segregation energy of hydrogen at GB and free surface is calculated as:

$$E_{g(fs)}^{sg} = E_{g(fs)}^{ad} - E_{b}^{ad} \tag{4.7}$$

where $E_{g(fs)}^{ad}$ denotes the adsorption energy of hydrogen at GB (free surface), and E_{b}^{ad} is the adsorption energy of hydrogen in bulk lattice.

The hydrogen occupancy c_i (defined as hydrogen/metal atomic ratio) at an adsorption site i can be related to the bulk hydrogen concentration c_0 as [11, 14]:

$$\frac{c_i}{1-c_i} = \frac{c_0}{1-c_0}\exp\left(-E_i^{sg}\right) \tag{4.8}$$

where the segregation energy of hydrogen at site i is defined in the same way as Eq. 4.7 Combining the above with the analytical model (see Eq. 4.4), we can obtain the segregation energy for an interstitial site enclosed in a polyhedron as:

$$E_i^{sg} = -B\Omega_p \frac{dV_p^i}{V_p^{0,i}} + E_{0,i}^{ad} - E_b^{ad} \tag{4.9}$$

where $dV_p^i / V_p^{0,i}$ and $E_{0,i}^{ad}$ denote the corresponding dV_p / V_p^0 and E_0^{ad} (cf. Eq. 4.4) of the polyhedron at adsorption site i. From Eqs. 4.8-4.9, the hydrogen occupancy at different polyhedrons as functions of dV_p / V_p^0 and c_0 can be analyzed, shown in Figure 4.10 (for the sample case of T=300K).

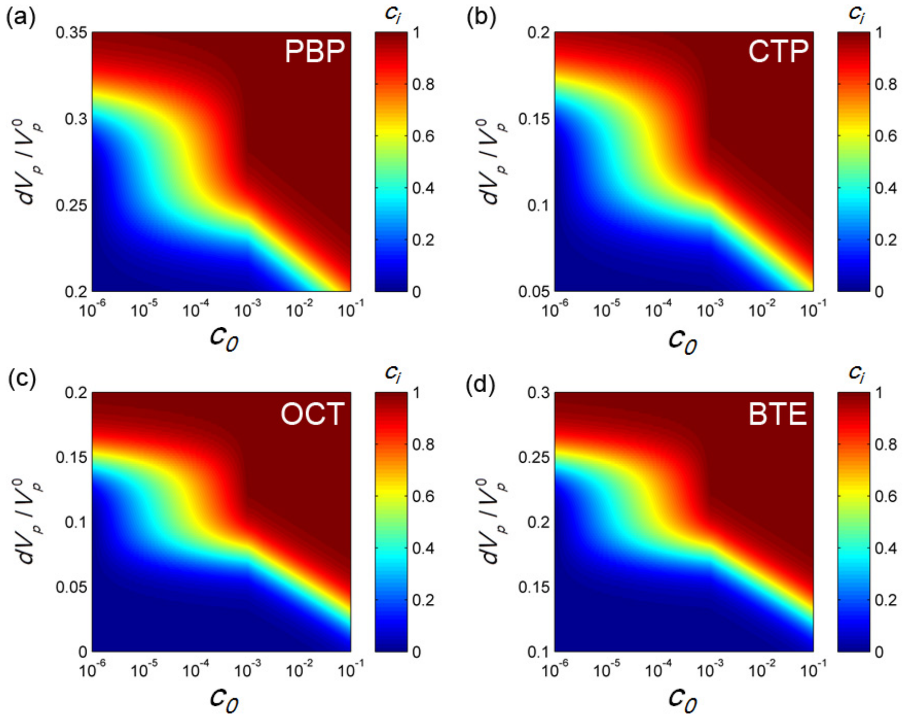

Figure 4.10. Hydrogen occupancy c_i at different polyhedrons as the volume distortion dV_p/V_p^0 and bulk hydrogen concentration c_0 vary.

With hydrogen segregation at GBs characterized, the hydrogen influenced work of separation can be easily analyzed combining our analytical model and the thermodynamic Rice-Wang model [53]: $W_c \approx W_0 - \sum_i (E_{gb}^{sg,i} - E_{fs}^{sg,i}) c_i \Theta_{\max}$, where W_c is the work of separation with hydrogen trapping, W_0 is the work of separation without any hydrogen, $\Theta_{\max}$ is the maximum hydrogen concentration of polyhedral site. Figure 4.11 shows the predicted evolution of work of separation (W_c) for several representative symmetric tilt Ni GBs, i.e., $\Sigma 3$, $\Sigma 9$, $\Sigma 11$ $\Sigma 17$ and $\Sigma 73$ GBs. Here only the hydrogen segregation directly along the GB was considered in the analysis for simplicity and the room temperature of T=300K was assumed.

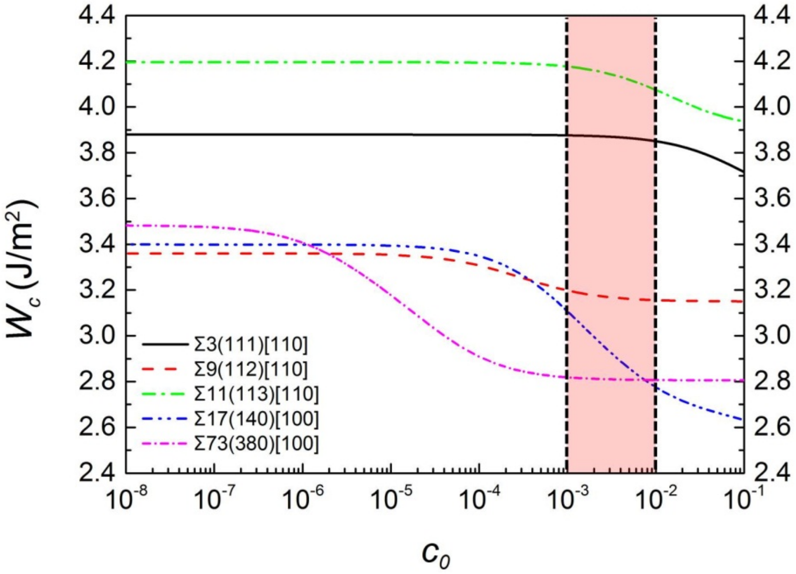

Figure 4.11. The evolution of work of separation (W_c) for several symmetric tilt Ni GBs, i.e., Σ 3(111)[110] (solid black line), Σ9(112)[110] (red dash line), Σ11(113)[110](green dash dot line), Σ17(140)[100] (blue dash dot-dot dash line), Σ73(380)[100] (pink short dash dot line) as the hydrogen bulk concentration varies (considering hydrogen segregation along the GB).

There are several observations from Figure 4.11. First, we see that Σ73 is most sensitive to H infiltration, showing an apparent drop in W_c starting from c_0 = 1 appm, while Σ3 is most resistant to H infiltration with W_c remaining invariant even up to a very high c_0 of 10,000 appm. Also it is worth noting from Fig. S8 that another GB, Σ11, that exhibits very similar behaviors as Σ3. Second, we note that the two GBs, Σ17 and Σ73, exhibit noticeably larger and more abrupt drop in W_c in comparison to the other three, i.e., Σ3, Σ9 and Σ11, suggesting that Σ 17 and Σ73 be more susceptible to HE (in the sense of cleavage-type failure).

To put the above observations in perspective, we examined relevant experimental studies reported in literature. In a recent study by S. Bechtle et al. [19], the HE phenomena in pure Ni was investigated. In the study, they demonstrated that the HE resistance of Ni can be considerably enhanced by increasing the fraction of the so-called “special” GBs. These “special” GBs refer to the GBs with low sigma number (Σ<29) under the CSL nomenclature. Among those “special” GBs, $\Sigma 3$ and $\Sigma 3^n$ GBs were shown to play the main role in enhancing the HE resistance [54]. This is directly reflected in our results shown in Figure 4.11, where we see that $\Sigma 3$ and $\Sigma 9$ are both very resistant to hydrogen infiltration (The red shadow region in Figure 4.11 correspond to the c_0 in Bechtle’s experiment). On the other hand, our results also indicated that the general definition of “special” GBs is ambiguous, as evidenced by the case of Σ 17(140)[100] (a “special” GB according to the general definition) in Fig. S8 where sizable influence of hydrogen is observed. This echoes with the work by Randle [54] which demonstrated that the CSL definition of “special” GBs is indeed ambiguous and a more realistic definition is needed when applied to corrosion or fracture of GBs or GB engineering.

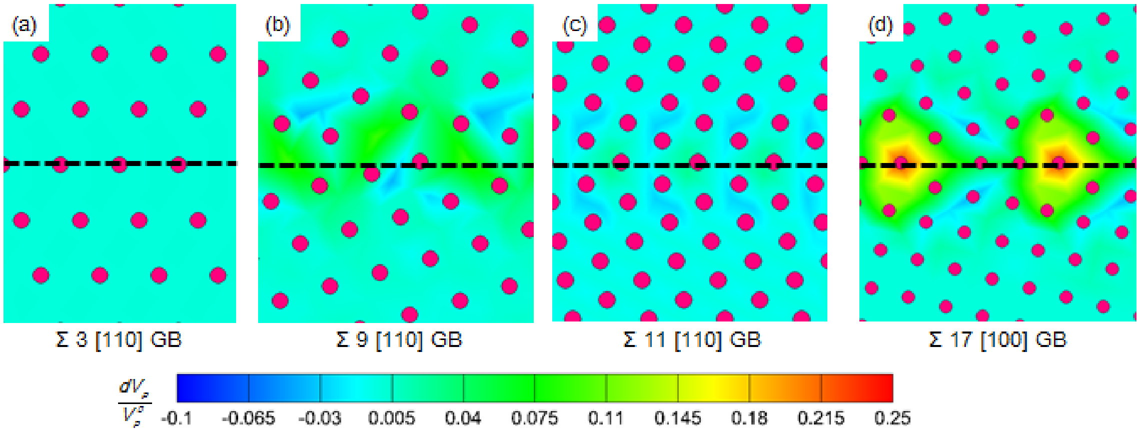

Figure 4.12. Contour plots of lattice distortion dV_p/V_p^0 (of polyhedrons) along and neighboring the GB for (a) $\Sigma 3$, (b) $\Sigma 9$, (c) $\Sigma 11$ and (d) $\Sigma 17$ symmetric tilt GBs in Ni.

In light of the above, we explored the possibility of identifying a more-refined definition of “special” GBs using the new insights from the present study. As we stated in the main text, the key underlying strong trapping of hydrogen at a GB is the lattice distortion. In Figure 4.12, we show the corresponding contour plots of lattice distortion dV_p/V_p^0 (of polyhedrons) along those “special” ($\Sigma<29$) GBs examined in Figure 4.11, we note that these contour plots also help effectively distinguish the GBs within the “special” category, i.e., we can clearly see that $\Sigma 3$, $\Sigma 9$ and $\Sigma 11$ show significantly less degree of lattice distortion than $\Sigma 17$. In this regard, we expect that $\Sigma 17$ would remain quite susceptible to HE despite it being a “special” GB (according to the general $\Sigma<29$ definition). Among the three GBs, i.e., $\Sigma 3$, $\Sigma 9$ and $\Sigma 11$, we see from Figs S7 and S8 that $\Sigma 3$ and $\Sigma 11$ are particularly insensitive to hydrogen infiltration. This can be further explained by a detailed analysis at the polyhedron level, described as follows. For the $\Sigma 3$ GB, there is simply no distortion at GB as it consists of only pristine BTE polyhedrons. While for the $\Sigma 11$ GB, it is composed of nearly pristine CTP polyhedrons with ignorable distortion. The observed high resistance of $\Sigma 11$ to hydrogen is also consistent with previous experimental studies, e.g., Baskes et al. [25] investigated H trapping behavior in Ni $\Sigma 9$ and $\Sigma 11$ GB, suggesting no apparent HE tendency; Du et al. [55] demonstrated there is no notable hydrogen trapping in γ-Fe $\Sigma 11$ GB. From the above, we see that we can redefine “special” GBs in the context of HE, e.g., as the group of GBs with overall (or individual) lattice distortion smaller than a *critical threshold*. Of course further studies are necessary to properly determine this critical threshold distortion.

4.7.6 Generality of the model: application to BCC Nb

The model (cf. Eq. 4.4) we proposed is a rather general model, and is not just limited to FCC metals. To demonstrate the general applicability of the model, we have performed some preliminary studies on BCC metals. Taking BCC Nb as an example, the results are presented in Figure 4.13 and Table 4.3, which clearly demonstrates the correspondence between $\mathrm{dV_p/V_p^0}$ and $\mathrm{E^{ad}}$ data (cf. Figure 4.13a) and that the model remains valid (cf. Figure 4.13b and Table 4.3). This provides a direct support to the generality of our model. Additionally we expect that our model should be applicable to HCP systems given their close-packing lattice and close structural resemblance to FCC crystals.

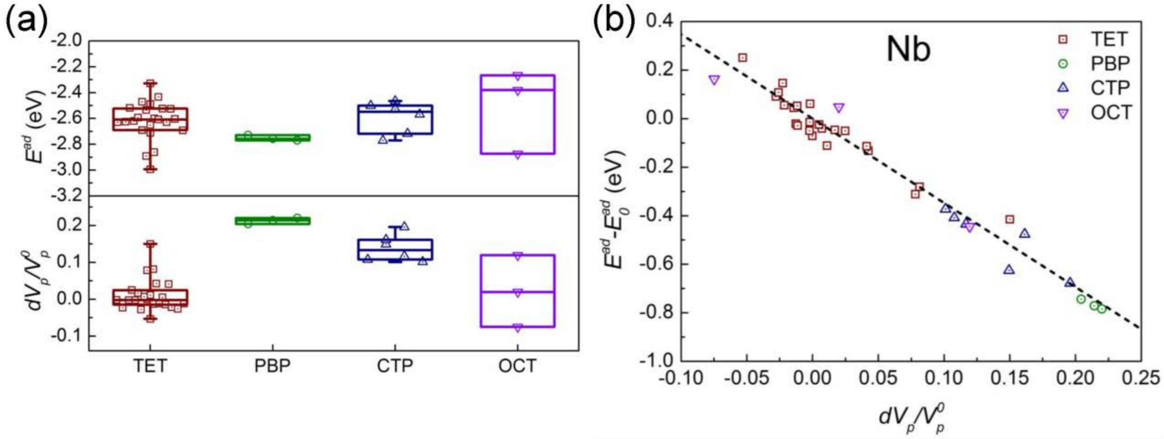

Figure 4.13. (a) The variation in the hydrogen adsorption energy E^{ad} and normalized lattice dilatation $dV_p/dV_p{}^0$ of polyhedrons in bcc Nb. (b) Comparison between the DFT calculated (open symbols) and model predicted (dash lines) adsorption energetics versus volume distortion relation in bcc Nb.

Table 4.3. List of material properties, i.e., bulk modulus (B), bulk hydrogen partial volume (Ω), predicted hydrogen partial volume at polyhedrons (Ω_p), model predicted (and DFT calculated) adsorption energy of hydrogen in a pristine polyhedron, i.e., [Model] E_0^{ad} ([DFT] E_0^{ad}) in bcc Nb.

Properties \ System		Nb
B (GPa)		176
Ω (Å^3)		3.30
Ω_p (Å^3)		3.16
[Model] E_0^{ad} ([DFT] E_0^{ad}) (eV)	TET	-2.60 (-2.64)
	OCT	-2.41 (-2.38)
	BTE	--
	PBP	-1.98
	CTP	-2.09

4.8 References

[1] Johnson WH. On Some Remarkable Changes Produced in Iron and Steel by the Action of Hydrogen and Acids Proceedings of the Royal Society of London 1874;23:12.

[2] Gangloff RP, Wei RP. Gaseous hydrogen embrittlement of high strength steels. MTA 1977;8:1043-53.

[3] Lynch SP. Hydrogen embrittlement and liquid-metal embrittlement in nickel single crystals. Scripta Metallurgica 1979;13:1051-6.

[4] Hirth JP. Effects of hydrogen on the properties of iron and steel. MTA 1980;11:861-90.

[5] Lynch SP. A fractographic study of gaseous hydrogen embrittlement and liquid-metal embrittlement in a tempered-martensitic steel. Acta Metallurgica 1984;32:79-90.

[6] Myers SM, Baskes M, Birnbaum H, Corbett JW, DeLeo G, Estreicher S, et al. Hydrogen interactions with defects in crystalline solids. Reviews of Modern Physics 1992;64:559.

[7] Wipf H. Diffusion of hydrogen in metals. Hydrogen in metals III: Springer; 1997. p. 51-91.

[8] Robertson IM. The effect of hydrogen on dislocation dynamics. Engineering Fracture Mechanics 2001;68:671-92.

[9] Kirchheim R. Reducing grain boundary, dislocation line and vacancy formation energies by solute segregation. I. Theoretical background. Acta Materialia 2007;55:10.

[10] Kirchheim R. Reducing grain boundary, dislocation line and vacancy formation energies by solute segregation II. Experimental evidence and consequences. Acta Materialia 2007;55:10.

[11] Song J, Curtin WA. A nanoscale mechanism of hydrogen embrittlement in metals. Acta Materialia 2011;59:1557-69.

[12] Martin ML, Somerday BP, Ritchie RO, Sofronis P, Robertson IM. Hydrogen-induced intergranular failure in nickel revisited. Acta Materialia 2012;60:2739-45.

[13] Solanki K, Tschopp M, Bhatia M, Rhodes N. Atomistic Investigation of the Role of Grain Boundary Structure on Hydrogen Segregation and Embrittlement in α-Fe. Metall and Mat Trans A 2013;44:1365-75.

[14] Song J, Curtin WA. Atomic mechanism and prediction of hydrogen embrittlement in iron. Nat Mater 2013;12:145-51.

[15] Wang S, Martin ML, Sofronis P, Ohnuki S, Hashimoto N, Robertson IM. Hydrogen-induced intergranular failure of iron. Acta Materialia 2014;69:275-82.

[16] Lu G, Kaxiras E. Hydrogen Embrittlement of Aluminum: The Crucial Role of Vacancies. Physical Review Letters 2005;94:155501.

[17] Takai K, Shoda H, Suzuki H, Nagumo M. Lattice defects dominating hydrogen-related failure of metals. Acta Materialia 2008;56:5158-67.

[18] Pundt A, Kirchheim R. Hydrogen in metals microstructural aspects. Annual Review of Materials Research 2006;36:53.

[19] Bechtle S, Kumar M, Somerday BP, Launey ME, Ritchie RO. Grain-boundary engineering markedly reduces susceptibility to intergranular hydrogen embrittlement in metallic materials. Acta Materialia 2009;57:4148-57.

[20] Oudriss A, Creus J, Bouhattate J, Savall C, Peraudeau B, Feaugas X. The diffusion and trapping of hydrogen along the grain boundaries in polycrystalline nickel. Scripta Materialia 2012;66:37-40.

[21] Grimmer H. Coincidence-site lattices. Acta Crystallographica Section A 1976;32:783-5.

[22] Sutton A, Vitek V. On the structure of tilt grain boundaries in cubic metals I. Symmetrical tilt boundaries. Phil Trans R Soc Lond A 1983;309:1-36.

[23] Sutton A, Vitek V. On the structure of tilt grain boundaries in cubic metals II. Asymmetrical tilt boundaries. Phil Trans R Soc Lond A 1983;309:37-54.

[24] Ashby MF, Spaepen F, Williams S. The structure of grain boundaries described as a packing of polyhedra. Acta Metallurgica 1978;26:1647-63.

[25] Baskes MI, Vitek V. Trapping of hydrogen and helium at grain boundaries in nickel: An atomistic study. MTA 1985;16:1625-31.

[26] Tschopp MA, Solanki KN, Gao F, Sun X, Khaleel MA, Horstemeyer MF. Probing grain boundary sink strength at the nanoscale: Energetics and length scales of vacancy and interstitial absorption by grain boundaries in α-Fe. Physical Review B 2012;85:064108.

[27] Kresse G, Hafner J. Ab initio molecular dynamics for liquid metals. Physical Review B 1993;47:558-61.

[28] Kresse G, Furthmüller J. Efficient iterative schemes for ab initio total-energy calculations using a plane-wave basis set. Physical Review B 1996;54:11169-86.

[29] Blöchl PE. Projector augmented-wave method. Physical Review B 1994;50:17953-79.

[30] Kresse G, Joubert D. From ultrasoft pseudopotentials to the projector augmented-wave method. Physical Review B 1999;59:1758-75.

[31] Perdew JP, Chevary JA, Vosko SH, Jackson KA, Pederson MR, Singh DJ, et al. Atoms, molecules, solids, and surfaces: Applications of the generalized gradient approximation for exchange and correlation. Physical Review B 1992;46:6671-87.

[32] Perdew JP, Burke K, Ernzerhof M. Generalized Gradient Approximation Made Simple. Physical Review Letters 1996;77:3865-8.

[33] Okabe A. Spatial tessellations: Wiley Online Library; 1992.

[34] Switendick A. Band structure calculations for metal hydrogen systems. Zeitschrift für Physikalische Chemie 1979;117:89-112.

[35] Friedel J. Dislocations: International Series of Monographs on Solid State Physics: Elsevier; 2013.

[36] Rodney D. Molecular dynamics simulation of screw dislocations interacting with interstitial frank loops in a model FCC crystal. Acta Materialia 2004;52:607-14.

[37] Seita M, Hanson JP, Gradečak S, Demkowicz MJ. The dual role of coherent twin boundaries in hydrogen embrittlement. Nature communications 2015;6.

[38] Wei H, Xiang Y, Ming P. A generalized Peierls-Nabarro model for curved dislocations using discrete Fourier transform. Communications in computational physics 2008;4:275-93.

[39] Dai S, Xiang Y, Srolovitz DJ. Atomistic, generalized Peierls–Nabarro and analytical models for (111) twist boundaries in Al, Cu and Ni for all twist angles. Acta Materialia 2014;69:162-74.

[40] Lucarini V. Symmetry-Break in Voronoi Tessellations. Symmetry 2009;1:21.

[41] Schusteritsch G, Kaxiras E. Sulfur-induced embrittlement of nickel: a first-principles study. Modelling and Simulation in Materials Science and Engineering 2012;20:065007.

[42] You Y-W, Kong X-S, Wu X-B, Xu Y-C, Fang Q, Chen J, et al. Dissolving, trapping and detrapping mechanisms of hydrogen in bcc and fcc transition metals. AIP advances 2013;3:012118.

[43] Korhonen T, Puska MJ, Nieminen RM. Vacancy-formation energies for fcc and bcc transition metals. Physical Review B 1995;51:9526-32.

[44] Kittel C, McEuen P, McEuen P. Introduction to solid state physics: Wiley New York; 1996.

[45] Du YA, Rogal J, Drautz R. Diffusion of hydrogen within idealized grains of bcc Fe: a kinetic Monte Carlo study. Physical Review B 2012;86:174110.

[46] Mehl MJ, Papaconstantopoulos DA. Applications of a tight-binding total-energy method for transition and noble metals: Elastic constants, vacancies, and surfaces of monatomic metals. Physical Review B 1996;54:4519-30.

[47] Leyson G, Grabowski B, Neugebauer J. Multiscale description of dislocation induced nano-hydrides. Acta Materialia 2015;89:50-9.

[48] Guo G, Wang H. Gradient-corrected density functional calculation of elastic constants of Fe, Co and Ni in bcc, fcc and hcp structures. Chinese Journal of Physics 2000;38:949-61.

[49] Fukai Y. The metal-hydrogen system: basic bulk properties: Springer Science & Business Media; 2006.

[50] Angelo JE, Moody NR, Baskes MI. Trapping of hydrogen to lattice defects in nickel. Modelling and Simulation in Materials Science and Engineering 1995;3:289.

[51] Nocedal J, Wright SJ. Least-squares problems. Numerical optimization 2006:245-69.

[52] Robinson K, Gibbs G, Ribbe P. Quadratic elongation: a quantitative measure of distortion in coordination polyhedra. Science 1971;172:567-70.

[53] Rice JR, Wang J-S. Embrittlement of interfaces by solute segregation. Materials Science and Engineering: A 1989;107:23-40.

[54] Randle V. Twinning-related grain boundary engineering. Acta materialia 2004;52:4067-81.

[55] Du YA, Ismer L, Rogal J, Hickel T, Neugebauer J, Drautz R. First-principles study on the interaction of H interstitials with grain boundaries in α- and γ-Fe. Physical Review B 2011;84:144121.

Chapter 5: The Role of Grain Boundaries in Hydrogen Diffusion: Atomistic Origin and Mechanistic Modeling

In Chapter 4, hydrogen segregation tendency at different grain boundaries was carefully studied by means of proposed space tessellation algorithm and first principles calculations. It was found the energetics of hydrogen at grain boundaries are strongly relied on local atomic structures of grain boundaries. However, aside from hydrogen segregation, the kinetics and diffusion behaviors of hydrogen at grain boundaries are also important and the convinced mechanisms regarding hydrogen diffusion at grain boundaries are still not fully understood. Therefore, this chapter quantified the kinetics of hydrogen at grain boundaries employing first principles calculations and Kinetic Monte Carlo simulations. The grain boundary angle-dependent diffusivity was identified and one micromechanical model was proposed to predictively assess hydrogen diffusion behaviors at grain boundaries.

- This chapter shall be submitted as: **The role of grain boundaries in hydrogen diffusion: atomistic origin and mechanistic modeling**, Xiao Zhou, W.A. Curtin, Jun Song

5.1 Abstract

Hydrogen embrittlement (HE) is a common nuisance that severely deteriorates mechanical properties of structural metals and alloys, but the physical origin of HE is still not clear. In order to better understand the mechanisms of HE, elucidation of hydrogen kinetics at microstructural heterogeneities such as grain boundary (GB) is of extreme importance. In this study, hydrogen diffusion behaviors at various types of GBs with GB angle ranging from low to high tilt angle were systematically studied using first principles calculations and Kinetic Monte Carlo simulations. Our results suggested that GB plays the dual role in determining hydrogen diffusion (i.e., fast diffusion and blocking), strongly depended on the atomic arrangement of GB and the corresponding tilt angle. Based on our calculated results, one micromechanical model was proposed to quantitatively evaluate hydrogen diffusion behaviors and the distinct transition between fast diffusion and blocking at GBs. The present study provides some new insights towards the clarification of the effect of microstructural heterogeneities on hydrogen kinetics, offering the new knowledge towards mechanistic understanding of HE.

5.2 Introduction

Hydrogen embrittlement (HE), a phenomenon where hydrogen causes premature failure with a drastic loss in ductility, toughness and strength in metals, in particular high-strength metals, has been a topic of intense research for decades [1-7]. Though the exact microscopic mechanism underlying HE remains elusive and highly debated [2, 8-11], it is commonly agreed that one prerequisite for HE to occur is the delivery of hydrogen to target regions to achieve a critical hydrogen concentration. Consequently it necessitates accurate knowledge of hydrogen transport in metals in the interpretation of various HE data and phenomena.

The effect of microstructures on hydrogen diffusion in metals has been well recognized and studied in the literature [3, 12-15]. In particular, hydrogen segregation and diffusion along GBs has been regarded to be of great relevance to hydrogen induced intergranular cracking [16-20]. Nonetheless, different and even contrary viewpoints exist regarding the exact role of GBs in hydrogen diffusion. As much as numerous studies reporting accelerated hydrogen transport along GBs [7, 16-19, 21-25], which was attributed to low activation barrier and short-circuit diffusion along GBs [18, 26]. However, there also exist ample evidence of the opposite observation [17, 27-30]. For instance, Yao et al. [28] discovered at extremely low hydrogen concentration, hydrogen is virtually stopped at GBs, suggesting GBs strongly retard hydrogen motion. They claimed this slowdown of hydrogen diffusion at GBs attributed to deep trapping sites provided by GBs. In addition, the experimental results from Birnbaum et al. [16] revealed that GBs have dual role on hydrogen diffusion: on one hand, some GBs can facilitate hydrogen diffusion and on the other hand, they noted other GBs can neither enhance nor impede hydrogen diffusion (i.e., in some GBs, hydrogen keeps the same as in the bulk lattice). Oudriss et al. [31, 32] suggested hydrogen diffusion behaviors at GBs pronouncedly rely on the GB characterizes and grain size where random high angle GBs can facilitate hydrogen diffusion while some special GBs inhibited hydrogen transportation.

The high contention regarding the role of GBs in hydrogen diffusion indicates a clear lack of mechanistic understanding. The present study aims to address this long-standing open question. Comprehensive first principles density functional theory (DFT) calculations have been performed to obtain complete mapping of hydrogen energetics, migration pathways and associated energy barriers at and neighboring GBs, and DFT-informed Kinetic Monte Carlo (KMC) simulations were conducted to examine the collective hydrogen diffusion behaviors. Our results reveal two distinct hydrogen diffusion responses as the GB tilt angle varies, indicative of the dual role of GBs in hydrogen diffusion. The atomistic origin underlying different hydrogen diffusion behaviors at GBs is then elucidated and a mechanistic model is developed to accurately predict the transition between those behaviors. Our work sheds critical new lights on understanding and interpreting the various experimental studies of hydrogen diffusion in metals.

5.3 Computatinal methods

The various GB systems were systematically investigated by means of *ab-initio* calculations. Vienna ab initio simulation package (VASP) [33, 34] was used for all calculations. The electron-ion interactions were prescribed by Blöch projector-augmented wave method (PAW) [35, 36]. Generalized gradient approximation (GGA) in the formula proposed by Perdew, Burke and Ernzerhof (PBE) [37] based on plane-wave basis sets was adopted for exchange-correlation and ultrasoft pseudopotential were utilized for the core-valence interactions. First-order Mehthfessel-Paxton scheme with a 0.1 eV smearing width was used. In terms of GB structure optimization, the convergence criteria of energy and atomic fore were set as 10^{-4} eV and 10^{-2} eV/Å respectively. As for investigating hydrogen migration barriers at various systems, nudged elastic band method (NEB) [38] was used, which is implemented in VASP. The hydrogen diffusion behavior can be monitored and gauged by our Kinetic Monte Carlo (KMC) simulations. The hydrogen diffusivity was calculated based on the mean square displacement (MSD) extracted from hydrogen trajectory in our KMC simulations. In particular, the hydrogen diffusion coefficient can be obtained by $D = \frac{\left\langle \left[\vec{r}_t - \vec{r}_0\right]^2 \right\rangle}{2Nt}$, where $\vec{r}_t$ is the hydrogen position after time t, $\vec{r}_0$ is hydrogen position at time 0 and N is the dimension number.

5.4 Results and discussion

In order to study hydrogen diffusion along GBs, first we need to identify the interstitial sites for hydrogen adsorption therein. Here we use the method proposed in Zhou et al. [39] to characterize the GB structure as an array of joint polyhedrons which serve as individual capsules to host interstitial hydrogen. In the group of GBs examined in this study, the following polyhedral units, octahedron (OCT), tetrahedron (TET), bi-tetrahedron (BTE), pentagonal bipyramid (PBP) and capped-trigonal prism (CTP), are identified, as schematically illustrated in Figure 5.1. The exact locations of interstitial sites within those polyhedrons and corresponding adsorption energetics are then determined from DFT calculations, following which migration barriers of hydrogen along GBs are obtained by NEB method. In particular, the migration barriers at grain boundaries are calculated based on our predetermined possible hopping paths between polyhedrons, then the barriers can be mapped to give us a clear picture, as shown in Figure 5.2. In this study, various types of GBs with GB tilt angle ranging from low to high angle are included. Specifically, the lowest barriers of hydrogen transported along Σ3[110](111) Σ5[100](210), Σ5[100](310) and Σ11[110](113) high angle GBs are 0.39, 0.27, 0.25 and 0.38 eV respectively, as shown in Figure 5.2. As for low angle GB, the corresponding barriers of hydrogen are higher compared with high angle GBs, with values being 0.50 and 0.80 eV for Σ25[100](430) and Σ41[100](540) GB respectively. To put the above results in context, it is worth noting that the migration barrier of hydrogen transport in bulk Ni lattice is determined to be 0.38 eV, corresponding to hydrogen hopping between two neighboring octahedral sites through the transition tetrahedral site. The value of 0.38 eV in our study is also in agreement with previous theoretical (0.37eV in [40]) and experimental (0.43 eV in [41]) studies.

It is apparent that the migration barriers of low angle GBs are distinct from those of high angle GBs. Interestingly, we also find the barriers of hydrogen diffusion along Σ3[110](111) and Σ11[110](113) GBs are very close to that in bulk Ni lattice. As for Σ3[110](111) GB, the local atomic structure of GB is composed of only OCT and TET basic structural units and these units have ignorable distortion (i.e., the structural units exist in Σ3[110](111) GB is almost the same as bulk Ni lattice). The hopping process of hydrogen along Σ3[110](111) GB is achieved by two OCT structural units with the assistance of transition TET structural unit, which is the same as hydrogen diffusion in bulk Ni lattice. Therefore, we believe the structural similarity between Σ3[110](111) GB and bulk Ni lattice results in the similar hydrogen migration barrier. With respect to special Σ11[110](113) GB, although the local atomic structure is different from bulk Ni lattice, there still exist no distortion in these units in Σ11[110](113) GB, which would not give rise to significant change of migration barrier. As for other high angle GBs, fast diffusion path can be identified along both Σ5[100](210) and Σ5[100](310) GBs with very low migration barriers compared with bulk Ni lattice. It is important to mention that the identified paths are continuous and satisfy connectivity in a complete period along GB so that hydrogen can successfully move along these paths without interruption in one complete period. However, the scenario is completely different when it comes to low angle GBs, we note there is no such continuous fast diffusion path. The migration barrier is apparently higher than that in bulk Ni lattice, indicating low angle GBs only consider as strong trapping sites and hydrogen atoms are totally blocked.

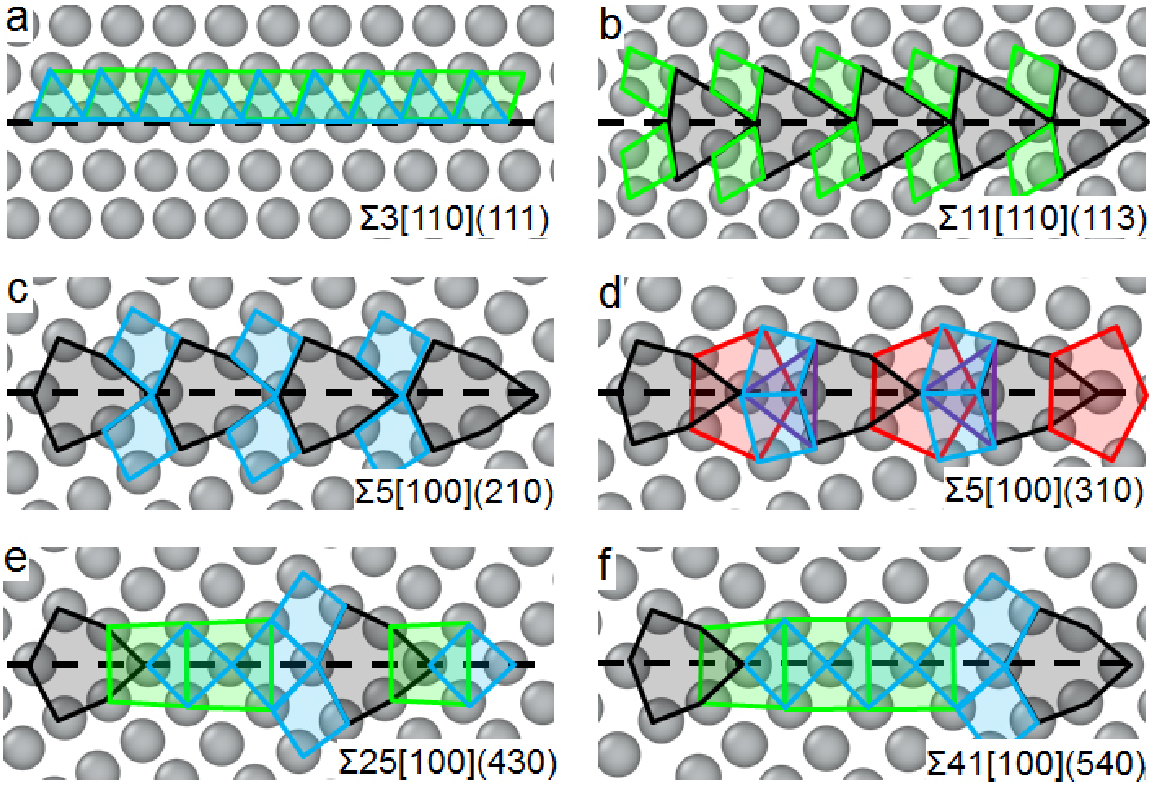

Figure 5.1. The representative GBs studied in this work. (a) Σ3[110](111) GB; (b) Σ11[110](113) GB; (c) Σ5[100](210) GB; (d) Σ5[100](310) GB; (e) Σ25[100](430) GB; (f) Σ41[100](540) GB;

the big grey balls are host Ni atoms. The colored geometrical shape illustrates different polyhedral units. In particular, octahedron (i.e., OCT) is shown in green shade, tetrahedron (i.e., TET) is presented in blue shade, capped-trigonal prism (i.e., CTP) is shown in grey shade, bi-tetrahedron (i.e., BTE) is shown in purple shade and pentagonal bipyramid (i.e., PBP) is shown in red shade.

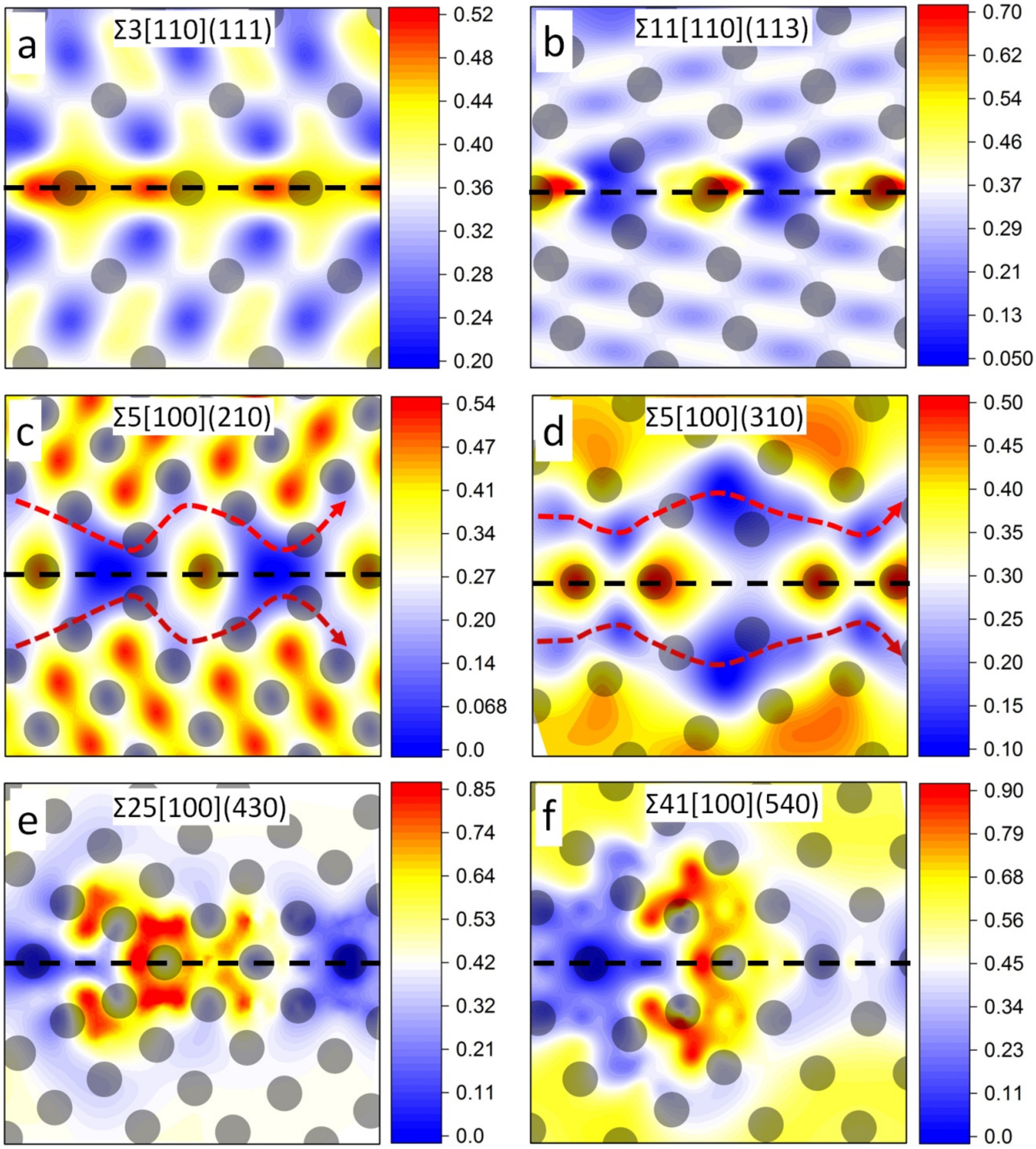

Figure 5.2. The maps of energy barriers of hydrogen at representative GBs. (a) Σ3[110](111) GB; (b) Σ11[110](113) GB; (c) Σ5[100](210) GB; (d) Σ5[100](310) GB; (e) Σ25[100](430) GB; (f) Σ41[100](540) GB. Big grey balls represent host Ni atoms. Note: the unit is eV.

To further investigate the kinetics of hydrogen along GBs, we then performed KMC simulations by using the calculated migration barriers of hydrogen as input. Within the framework of KMC, the time evolution of the system can be described as a series of hops from one polyhedral unit into the connected neighboring polyhedron. Firstly, we use bulk lattice model, involved only octahedral and tetrahedral units, to benchmark hydrogen diffusivity in bulk Ni lattice as a reference line. By using the calculated barrier of hydrogen in the bulk lattice with zero point energy (ZPE) correction, the hydrogen diffusion coefficient in bulk Ni lattice within dilute limit can be obtained. The Arrhenius equation $\mathrm{lnD} - \mathrm{ln}D_0 = (-\Delta E/k_B)/T$ is used for fitting the simulated data, where the prefactor D_0 is 1.7×10^{-6} $\mathrm{m^2s^{-1}}$ and the effective barrier ΔE is 0.45 eV. Our simulated result is in good agreement with other theoretical calculations (1.7×10^{-6} $\mathrm{m^2s^{-1}}$ and 0.48 eV in [42]) and experimental data (4.8×10^{-6} $\mathrm{m^2s^{-1}}$ and 0.408 eV in [14] and 6.7×10^{-6} $\mathrm{m^2s^{-1}}$ and 0.41 eV in [43]). Without ZPE correction, our simulated results are overestimated due the relative low migration barrier (i.e., 0.38 eV). However, we think ZPE correction does not influence the main results in this work because the main target is to clarify the role of GBs in hydrogen diffusion behavior in comparison with bulk lattice (reference state). Therefore, for the purpose of simplification and consistency, we do not include ZPE correction for diffusion simulations in both GBs and bulk lattice. The hydrogen diffusion coefficients as a function of hydrogen concentration C_H are also represented at various temperatures. It is worthy to note that the C_H in our KMC simulation is defined as the ratio of number of hydrogen inserted in system over number of all lattice sites in our KMC model. Therefore, this C_H includes the hydrogen atoms residing in bulk lattice or GB region. Regarding hydrogen diffusivities at various GBs, the KMC model for diverse GBs can be easily described by polyhedron units, where all possible hydrogen diffusion pathways can be considered as the conterminous polyhedrons and the hopping barriers of hydrogen for different pathways can be pre-decided by our first principles calculations, as mentioned before. Figure 5.3 shows the hydrogen diffusivities for some representative GBs as a function of C_H in different temperatures. As for Σ3[110](111) GB, hydrogen diffusivity remains unchanged for low C_H and then dramatically decreases with the increase of C_H. This scenario can be interpreted as the fact that there are sufficient unoccupied sites for hydrogen atoms at low C_H while the available sites drastically decrease with the increase of C_H and hydrogen would be blocked and the diffusion process would be retarded. In addition, the diffusion coefficients of other high-angle GBs (i.e., Σ5[100](210) and Σ5[100](310)) are much higher than that in bulk Ni lattice, originating from the fact that hydrogen atoms can freely transport in those paths with low migration barriers at GB. However, with the increase of the number of hydrogen, these polyhedrons with low migration barriers are fully occupied by hydrogen atoms. When hydrogen atoms stay in all possible polyhedrons at GBs, the fast diffusion paths at GBs would be completely blocked and hydrogen diffusion would come from the contribution of those hydrogen atoms in bulk Ni lattice. In addition, with respect to low-angle tilt GBs, hydrogen diffusivity is much lower than that in bulk lattice at low hydrogen concentration. This is rational since hydrogen atoms are trapped due to the fact that there is no conterminous pathway with low barrier at low-angle tilt GBs. Once these trapped sites are filled with hydrogen, hydrogen diffusivity begins to increase because of the contribution of those hydrogen residing in bulk Ni lattice.

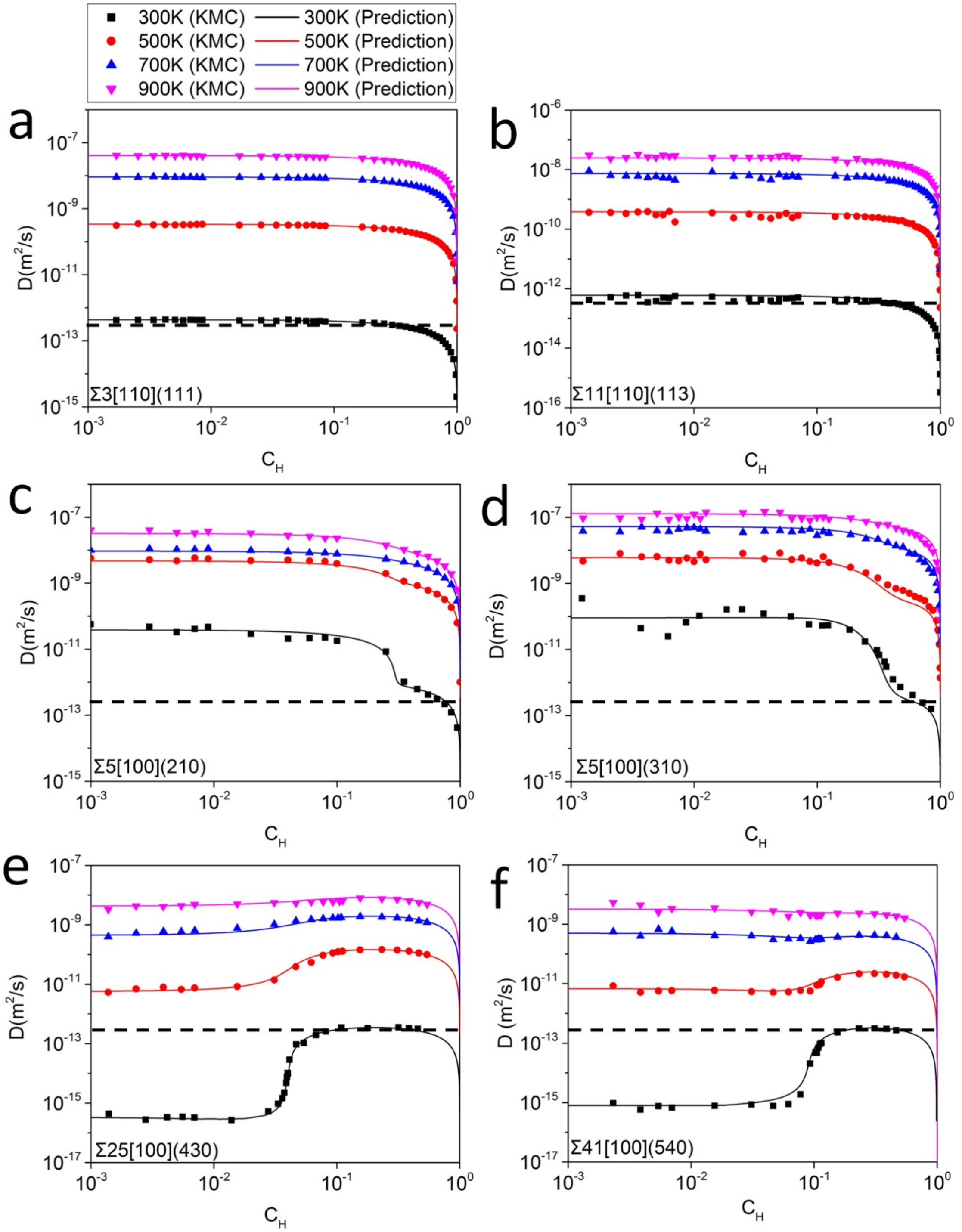

Figure 5.3. KMC calculated and model predicted hydrogen diffusivity as a function of hydrogen concentration at various GBs in different temperatures. (a) Σ3[110](111) GB; (b) Σ11[110](113)

GB; (c) Σ5[100](210) GB; (d) Σ5[100](310) GB; (e) Σ25[100](430) GB; (f) Σ41[100](540) GB. Note: the black dash line corresponds hydrogen diffusivity in the bulk lattice.

In order to quantitatively capture the characteristics of hydrogen diffusion at GBs, we develop one model to predict our KMC simulated results. In the framework of polyhedral geometrical description of GB structures, the hydrogen concentration in system is given by

$$C_H = \sum_i \frac{x_i^0}{1 + \exp\left(\frac{E_{seg}^i - \mu}{k_B T}\right)} \tag{5.1}$$

where x_i^0 is the fraction of specific polyhedral interstitial site *i*, E_{seg}^i is segregation energy of hydrogen trapped in polyhedral interstitial site *i* and μ is chemical potential. Therefore, the probability of finding hydrogen in specific polyhedral site *i* can be calculated by $p_i = \frac{x_i}{C_H}$, where $x_i = \frac{x_i^0}{1 + \exp\left(\frac{E_{seg}^i - \mu}{k_B T}\right)}$, corresponding to *individual hydrogen concentration* in specific site *i*. For example, Figure 5.4 shows the probability of hydrogen in various sites at representative Σ5[100](310) GB. After obtaining the probability, then the hydrogen diffusion coefficient can be calculated by

$$D(T, C_H) = \sum_i p_i(T)\delta_{0,i} \exp\left(\frac{-\Delta E_i}{k_B T}\right) \times \Theta(T, C_H) \tag{5.2}$$

where $\Theta(T, C_H) = \left(1 - \frac{x_i(\mathrm{C_H})}{x_i^0}\right)$ and $\delta_{0,i} = \gamma_i \beta_i^2 \alpha_0$, γ_i is average number of neighbor polyhedrons for specific site *i*, β_i is average jump distance and α_0 is attempt frequency. As illustrated in Figure 5.3, the model predicted results are in good agreement with the KMC simulated results, suggesting that this model can effectively capture the feature of concentration dependent diffusion behavior in our examined systems. Interestingly, it is worthy to note that the apparent transition of diffusion constant at low temperature (e.g., 300K) disappear when temperature increasing, and this scenario originates from the fact that thermal activity effect plays the dominant role in diffusion process when temperature is high.

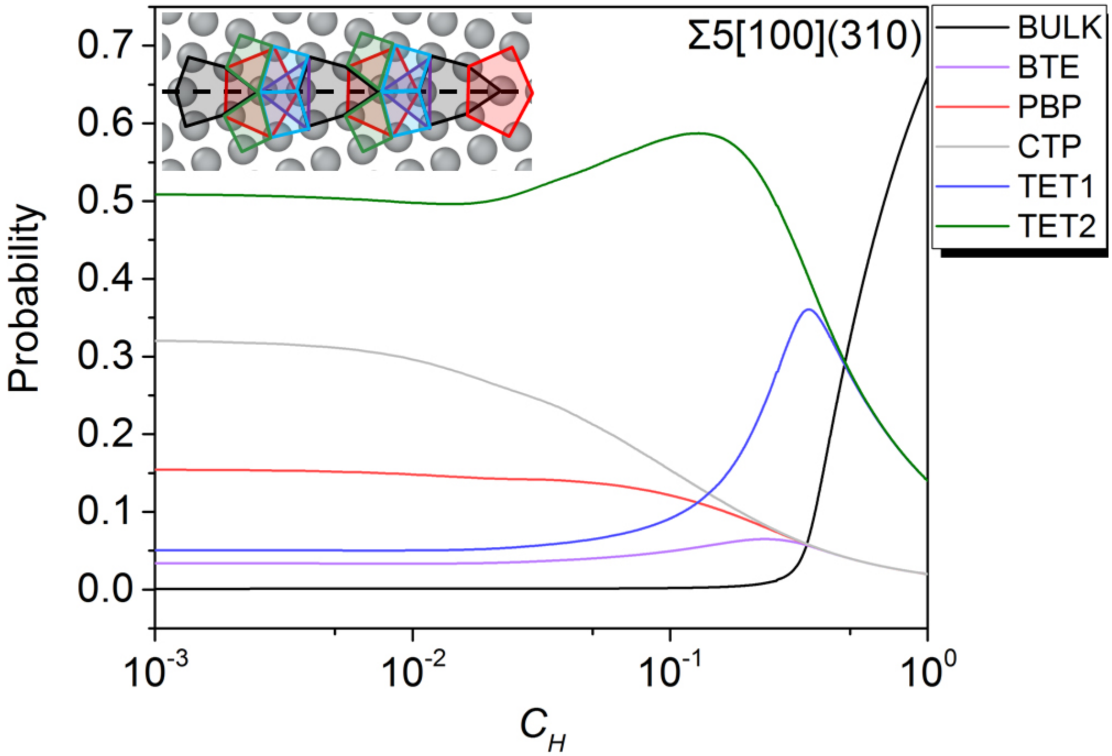

Figure 5.4. Probability of finding hydrogen at different polyhedral units in representative Σ5[100](310) GB.

In addition, we found hydrogen diffusivity is quite different for low-angle and high-angle tilt GBs, where fast transport and block take place at low-angle and high-angle tilt GB respectively. We assume the different hydrogen diffusion behavior is linked with diverse local geometrical structures at GBs, which is depended on the GB angle misorientation. The local atomic structure of GB is dynamically changed when GB angle being altered. To further quantitatively assess the effect of GB tilt angle on hydrogen diffusion, we utilize Frank-Bilby model to evaluate tilt angle dependent diffusivity. We consider GB as a series of dislocation core structure and the dislocation separation distance as a function of tilt angle can be easily achieved by Frank-Bilby equation, as shown in Figure 5.5. According to Frank-Bilby, the net burgers vector $\vec{B}$ can be calculated by

$$\vec{B} = \left(\vec{S}_A^{-1} - \vec{S}_B^{-1}\right) \cdot \vec{p} \tag{5.3}$$

where $\vec{p}$ is the periodic vector at GB and $\vec{S}_A$, $\vec{S}_B$ are operators changing the un-deformed reference crystal lattice, where the bicrystal is generated, into reference lattice A and B. Therefore, $\vec{B}$ is the resultant burgers vector of all basic dislocations at GBs. With respect to the investigated [100] tilt GBs. The tilt angle (θ) is in the range between 0º and 90º. There are two main Frank-Bilby Burgers vectors are taken into consideration where the first one gives rise to a net Burgers vector being parallel to the [100] direction of the reference lattice and the other one is parallel to $[\bar{1}\bar{1}0]$ direction of the reference lattice. Both of them are expressed by the primary dislocations with Burgers vector being correlated to the perfect crystal Σ1(110) θ=0º, i.e., $\vec{b} = \frac{a}{2}\left[\bar{1}\bar{1}0\right]$ and perfect crystal Σ1(100) θ=90º, i.e., $\vec{b} = a\left[100\right]$. Therefore, the intrinsic dislocation core separation distance can be calculated for GB in the tilt angle ranging from 0º to 90º by

$$d = \frac{\vec{b}}{2\sin\left(\frac{\theta}{2}\right)} \tag{5.4}$$

It is worth noting that the transition of Burgers vector direction from [110] to [100] occurs for the tilt angle 36.87° (Σ5). As can be seen in Figure 5.5, when dislocation separation core distance is larger than one primary Burgers vector (i.e., the tilt angle is smaller than 28.07° or larger than 61.93°), hydrogen atom is completely trapped in core region due to the cut-off distance being defined as primary Burgers vector in our simulations. When the tilt angle ranges from 28.07° to 61.93°, continued fast diffusion path can be found because of the overlapped dislocation cores, which corresponds the fast diffusion region (The whole picture regarding GB structure evolution can be seen in Figure 5.6). Therefore, we think 28.07° to 61.93° are the transition points from trapping region to fast diffusion region and the diffusivity as a function of GB angle is represented in Figure 5.7. In Figure 5.7, we selected different *bulk concentration* (i.e., x_b, corresponding to *individual hydrogen concentration* in the bulk lattice, defined in previous section), it is interesting to note that the GBs with the tilt angle being smaller than 28.07° or larger than 61.93°, hydrogen diffusivities along GBs are drastically smaller than the value for hydrogen in the bulk lattice. With the increase of *bulk concentration,* hydrogen diffusivity is ascended. At extremely low *bulk concentration*, hydrogen atoms are completed stuck, which agrees very well with the conclusion in Yao's study that hydrogen is virtually stopped at GBs. At relatively low *bulk concentration*, we find hydrogen diffusivity apparently rises up, but are still lower than that in bulk lattice. As for high angle GBs, the scenario is totally different, fast diffusion dominates hydrogen diffusion behavior. With the increase of *bulk concentration*, the diffusivity goes down, which is opposite in comparison with low angle GBs.

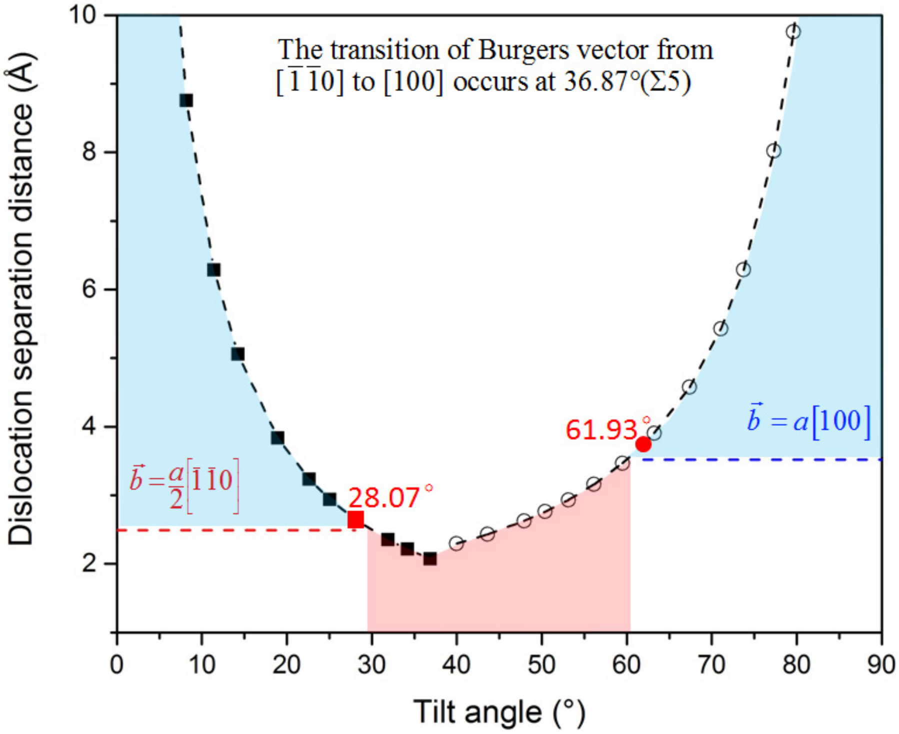

Figure 5.5. Dislocation separation distance as a function of tilt angle calculated by Frank-Bilby equation.

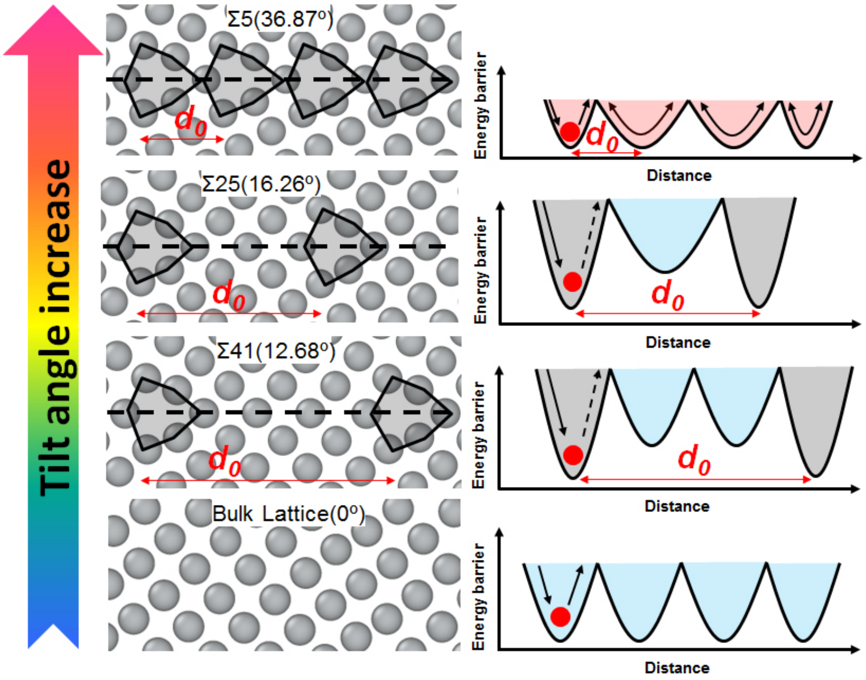

Figure 5.6. Possible hydrogen trap sites at various tilt GBs: Σ41(12.68º) GB; Σ25 (16.26º) GB and Σ5(36.87º) GB; the green ball represents trap site at dislocation core region and red balls are other hydrogen trap sites.

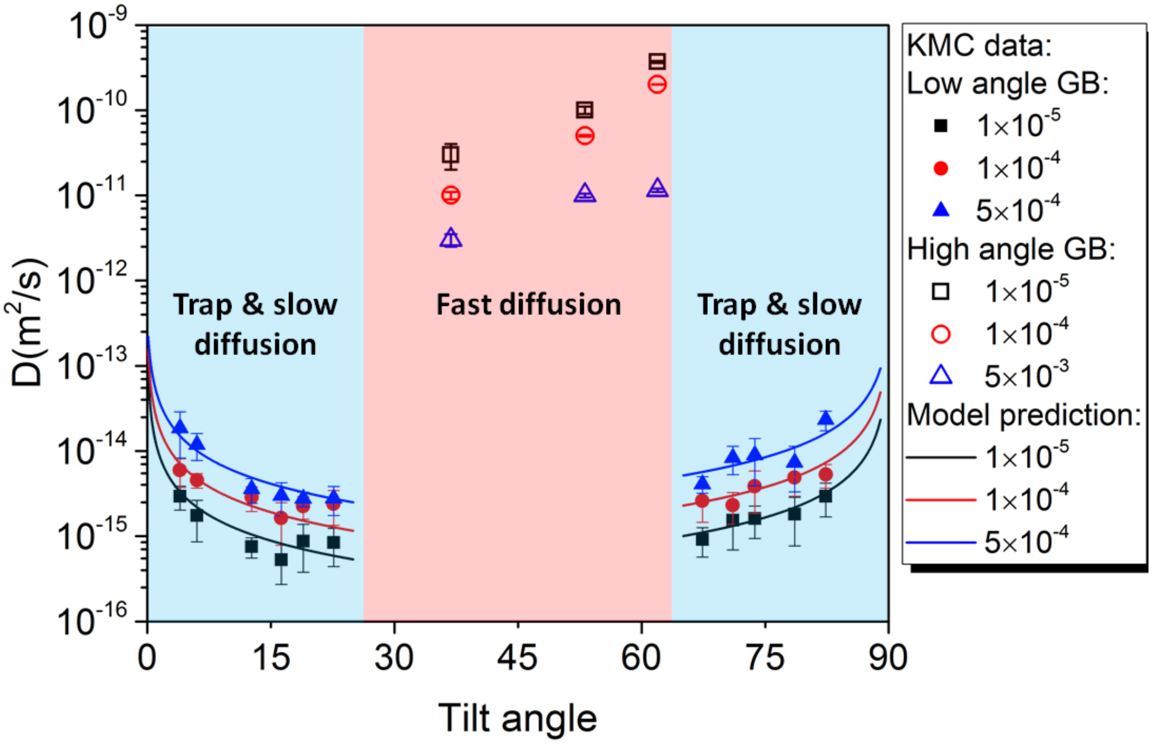

Figure 5.7. Hydrogen diffusivity as a function of tilt angle at 300K for different bulk concentration. Different regions are defined, namely, trap/slow diffusion region and fast diffusion region, depended on tilt angle.

In order to clarify the mechanism underlying our simulation results, we propose a continuum model to evaluate the angle dependent hydrogen diffusion coefficient. As recent reported in [31], the average dislocation density can be evaluated as a function of the tilt angle for low angle GBs, using the following equation:

$$\bar{\rho} = \frac{1}{bd}\sum_{i=1}^{nGB}\left(\frac{\theta_i}{2}\right)f_i \tag{5.5}$$

where n_{GB} is the number of the studied GBs, b is the Burgers vector, f_i is the fraction of tilt angle θ_i and d is the grain size. In our simulations, we use bi-crystal model for each low angle

GB, therefore we can consider f_i is equal to 1 because only one type GB exists in model. Also, n_{GB} is equal to 2 since there are two GBs in model. Therefore, the Eq. 5.5 can be simplified to:

$$\overline{\rho} = \frac{2}{bd} \sin\left(\frac{\theta}{2}\right) \tag{5.6}$$

we also assume that dislocations represent the only trapping sites and we can estimate the density of trapping sites of hydrogen related to the density of dislocations using the following equation extracted from geometrical considerations:

$$\xi_T = \pi \cdot b^2 \cdot \overline{\rho} \cdot N_b \tag{5.7}$$

where N_b is the number of bulk lattice sites per volume. Therefore, the trapping sites can be estimated in our simulations:

$$\xi_T = \frac{2\pi b}{d} \sin\left(\frac{\theta}{2}\right) N_b \tag{5.8}$$

According to classical trapping model, proposed by McNabb and Oriani, the trapping sites can effectively affect hydrogen diffusion coefficient D, which can be calculated as:

$$D = \frac{D_b}{1 + \frac{x_T}{x_b}\left(1 - \frac{x_b}{\xi_T}\right)} \tag{5.9}$$

where x_T is hydrogen concentration in trapping sites and x_b is bulk concentration, D_b is hydrogen diffusion coefficient in bulk lattice. By combining Eq. 5.8-5.9, we can get the final expression:

$$D = \frac{D_b}{1 + \frac{x_T}{x_b}\left(1 - \frac{d x_T}{2\pi b N_b \sin\left(\theta/2\right)}\right)} \tag{5.10}$$

We noted that this equation is completely deduced without any fitting parameter. By using Eq. 5.10, the predicted hydrogen diffusion coefficients as a function of GB angle for tilt angle constrained in low angle region are shown in Figure 5.7. We can see that our predicted values are well in agreement with our KMC data, which confirms the validation of this model.

However, when it comes to high angle GB with overlapped dislocation core structures, it is difficult to predict diffusion behavior due to the quite complex combination of various structure units, which will be undertaken in the future study.

Now we move to compare our results obtained from our model to the experimental data in the literature. Because of the lack of detail information regarding GB misorentations in these experiments, we cannot compare the data quantitatively. But we find all experimental data regarding hydrogen diffusion along GBs can be qualitatively categorized into three regimes defined in our study (i.e., slow diffusion/trapping region, fast diffusion and bulk diffusion). Specifically, the diffusivity along Σ3[110](111) and Σ11[110](113) GBs is very close to the diffusion coefficient in bulk Ni lattice, which are in consistent with experimental values as well [16, 40].

The puzzle of hydrogen diffusion along GBs was systematically investigated. The hydrogen migration behavior along Σ3[110](111) and Σ11[110](113) GBs is in the same order of magnitude as bulk Ni lattice, which originates from the non-distorted polyhedron units that cannot modify migration barriers. In contrast, high-angle GBs such as Σ5[100](210) GB possess the fast diffusion paths with lower migration barriers, suggesting hydrogen can quickly transport along GBs. These paths are consisted of continuous polyhedral structural units with drastic distortion. We think the severe polyhedral distortion plays the dominant role in controlling hydrogen migration barriers. In addition, the diversity of the arrangement of local polyhedral along GB also results in different pathways with different migration barriers. As for low-angle GBs, we discover these GBs are only considered as trapping sites instead of fast diffusion paths in our study. These low-angle GBs are composed of separated dislocation cores and no continuous fast diffusion paths exist in them, which means that hydrogen atoms are apparently retarded and even blocked. The comparison between our calculated data and experimental data in the literature are also discussed here. Our results reveal that hydrogen diffusivities along low-angle GBs are lower than that in bulk Ni lattice due to the trapping effect of dislocation cores which is in agreement with Yao's conclusion [28], suggesting hydrogen diffusion is virtually stopped. Oudriss' study [31, 32] also indicated that GBs with low misorentation angle trap hydrogen and stop hydrogen diffusion. Numerous studies such as Oudriss also suggested high angle GBs can act as fast diffusion paths, which is further confirmed by our results. More recently, Iwaoka et al. [44] investigated diffusion behaviors of hydrogen in fcc Pd, their results illustrated that hydrogen is retarded because of the strong trapping sites in dislocations while GBs are seen as rapid diffusion path, which can be completely explained by our work.

5.5 References

[1] Johnson WH. On some remarkable changes produced in iron and steel by the action of hydrogen and acids. Proceedings of the Royal Society of London 1874;23:168-79.

[2] Troiano AR. The role of hydrogen and other interstitials in the mechanical behavior of metals. trans ASM 1960;52:54-80.

[3] Cotterill P. The hydrogen embrittlement of metals. Progress in Materials Science 1961;9:205-301.

[4] Louthan M, Caskey G, Donovan J, Rawl D. Hydrogen embrittlement of metals. Materials Science and Engineering 1972;10:357-68.

[5] Oriani R. A mechanistic theory of hydrogen embrittlement of steels. Berichte der Bunsengesellschaft für physikalische Chemie 1972;76:848-57.

[6] Johnson H. Hydrogen embrittlement. Science 1973;179:228-30.

[7] Brass AM, Chanfreau A, Chene J. Hydrogen effects on materials behavior. Minerals, Metals, and Materials Society 1990.

[8] Robertson I, Birnbaum H. An HVEM study of hydrogen effects on the deformation and fracture of nickel. Acta Metallurgica 1986;34:353-66.

[9] Birnbaum HK, Sofronis P. Hydrogen-enhanced localized plasticity-a mechanism for hydrogen-related fracture. Materials Science and Engineering A 1994;176:191-202.

[10] Neeraj T, Srinivasan R, Li J. Hydrogen embrittlement of ferritic steels: observations on deformation microstructure, nanoscale dimples and failure by nanovoiding. Acta Materialia 2012;60:5160-71.

[11] Song J, Curtin W. Atomic mechanism and prediction of hydrogen embrittlement in iron. Nature materials 2013;12:145-51.

[12] Oriani RA. The diffusion and trapping of hydrogen in steel. Acta Metallurgica 1970;18:147-57.

[13] Sidorenko VM, Sidorak II. Determination of diffusion characteristics of the volume and boundary components of the flow of hydrogen in polycrystalline metals. Mater Sci 1973;9:50-4.

[14] Völkl J, Alefeld G. Diffusion of hydrogen in metals. In: Alefeld G, Völkl J, editors. Hydrogen in Metals I: Basic Properties. Berlin, Heidelberg: Springer Berlin Heidelberg; 1978. p. 321-48.

[15] Kirchheim R, Sommer F, Schluckebier G. Hydrogen in amorphous metals-I. Acta Metallurgica 1982;30:1059-68.

[16] Ladna B, Birnbaum HK. SIMS study of hydrogen at the surface and grain boundaries of nickel bicrystals. Acta Metallurgica 1987;35:2537-42.

[17] Kimura A, Birnbaum HK. Hydrogen induced grain boundary fracture in high purity nickel and its alloys-Enhanced hydrogen diffusion along grain boundaries. Acta Metallurgica 1988;36:757-66.

[18] Harris TM, Latanision M. Grain boundary diffusion of hydrogen in nickel. Metallurgical Transactions A 1991;22:351-5.

[19] Palumbo G, Doyle DM, El-Sherik AM, Erb U, Aust KT. Intercrystalline hydrogen transport in nanocrystalline nickel. Scripta Metallurgica et Materiala 1991;25:679-84.

[20] Hicks P, Altstetter C. Hydrogen-enhanced cracking of superalloys. Metallurgical Transactions A 1992;23:237-49.

[21] Calder RD, Elleman TS, Verghese K. Grain boundary diffusion of tritium in 304- and 316-stainless steels. Journal of Nuclear Materials 1973;46:46-52.

[22] Tsuru T, Latanision RM. Grain boundary transport of hydrogen in nickel. Scripta Metallurgica 1982;16:575-8.

[23] Lee JY, Lee SM. Hydrogen trapping phenomena in metals with B.C.C. and F.C.C. crystals structures by the desorption thermal analysis technique. Surface and Coatings Technology 1986;28:301-14.

[24] Ichimura M, Sasajima Y, Imabayashi M. Grain boundary effect on diffusion of hydrogen in pure aluminum. Materials Transactions, JIM 1991;32:1109-14.

[25] Stuhr U, Striffler T, Wipf H, Natter H, Wettmann B, Janssen S, et al. An investigation of hydrogen diffusion in nanocrystalline Pd by neutron spectroscopy. Journal of Alloys and Compounds 1997;253-254:393-6.

[26] Brass AM, Chanfreau A. Accelerated diffusion of hydrogen along grain boundaries in nickel. Acta Materialia 1996;44:3823-31.

[27] Latanision RM, Kurkela M. HYDROGEN PERMEABILITY AND DIFFUSIVITY IN NICKEL AND Ni-BASE ALLOYS. Corrosion 1983;39:174-81.

[28] Yao J, Cahoon JR. Experimental studies of grain boundary diffusion of hydrogen in metals. Acta Metallurgica Et Materialia 1991;39:119-26.

[29] Yao J, Cahoon JR. Theoretical modeling of gain boundary diffusion of hydrogen and its effect on permeation curves. Acta Metallurgica Et Materialia 1991;39:111-8.

[30] Pedersen A, Jónsson H. Simulations of hydrogen diffusion at grain boundaries in aluminum. Acta Materialia 2009;57:4036-45.

[31] Oudriss A, Creus J, Bouhattate J, Savall C, Peraudeau B, Feaugas X. The diffusion and trapping of hydrogen along the grain boundaries in polycrystalline nickel. Scripta Materialia 2012;66:37-40.

[32] Oudriss A, Creus J, Bouhattate J, Conforto E, Berziou C, Savall C, et al. Grain size and grain-boundary effects on diffusion and trapping of hydrogen in pure nickel. Acta Materialia 2012;60:6814-28.

[33] Kresse G, Hafner J. Ab initio molecular dynamics for liquid metals. Physical Review B 1993;47:558.

[34] Kresse G, Furthmüller J. Efficient iterative schemes for ab initio total-energy calculations using a plane-wave basis set. Physical Review B 1996;54:11169.

[35] Blöchl PE. Projector augmented-wave method. Physical Review B 1994;50:17953.

[36] Kresse G, Joubert D. From ultrasoft pseudopotentials to the projector augmented-wave method. Physical Review B 1999;59:1758.

[37] Perdew JP, Burke K, Ernzerhof M. Generalized gradient approximation made simple. Physical review letters 1996;77:3865.

[38] Henkelman G, Uberuaga BP, Jónsson H. A climbing image nudged elastic band method for finding saddle points and minimum energy paths. The Journal of Chemical Physics 2000;113:9901-4.

[39] Zhou X, Marchand D, McDowell DL, Zhu T, Song J. Chemomechanical Origin of Hydrogen Trapping at Grain Boundaries in fcc Metals. Physical Review Letters 2016;116:075502.

[40] Di Stefano D, Mrovec M, Elsässer C. First-principles investigation of hydrogen trapping and diffusion at grain boundaries in nickel. Acta Materialia 2015;98:306-12.

[41] Fukai Y. Formation of superabundant vacancies in M–H alloys and some of its consequences: a review. Journal of Alloys and Compounds 2003;356:263-9.

[42] Wang Y, Connétable D, Tanguy D. Influence of trap connectivity on H diffusion: Vacancy trapping. Acta Materialia 2016;103:334-40.

[43] Perkins WG, Begeal DR. Permeation and diffusion of hydrogen in ceramvar, copper, and ceramvar-copper laminates. Berichte der Bunsengesellschaft für physikalische Chemie 1972;76:863-.

[44] Iwaoka H, Arita M, Horita Z. Hydrogen diffusion in ultrafine-grained palladium: Roles of dislocations and grain boundaries. Acta Materialia 2016;107:168-77.

Chapter 6: Atomistic Investigation of the Influence of Hydrogen on Dislocation Nucleation during Nanoindentation in Ni and Pd

In Chapter 5, the kinetics of hydrogen at grain boundaries is thoroughly studied. We note hydrogen diffusion behaviors at grain boundaries exhibit two different types (i.e., fast diffusion and blocking) depending on grain boundaries characteristics. Meanwhile, the proposed micromechanical model can successfully predict the distinct diffusion behaviors at grain boundaries, providing new insights toward kinetics of hydrogen at microstructural heterogeneities. However, apart from grain boundaries, dislocation is another prevailing microstructural heterogeneity, in which the interaction between hydrogen and dislocations significantly affect hydrogen embrittlement. Therefore, this chapter focus on the influence of hydrogen on dislocation nucleation under plastic deform process. Our results reveal that hydrogen can facilitate dislocation nucleation and this effect stems from the local lattice distortion induced by hydrogen.

- This chapter has been published in *Acta Materialia*, shown as: **Atomistic investigation of the influence of hydrogen on dislocation nucleation during nanoindentation in Ni and Pd**, Xiao Zhou, Bin Ouyang, W.A. Curtin, and Jun Song, *Acta Materialia* 2016; 116: 364-369.

6.1 Abstract

The effects of hydrogen charging on the mechanical response of FCC Ni and Pd under nanoindentation are systematically investigated by molecular dynamics simulations. Simulations consider a random H distribution and time scales prevent any diffusion of H during the simulations. Hydrogen charging is then found to reduce the threshold load for dislocation nucleation, i.e., the *pop-in* load, but only to a limited extent. After *pop-in*, the indentation response is largely independent of the presence of H. Furthermore, the influence of hydrogen charging on the *pop-in* load originates only from the hydrogen-induced swelling of the lattice. That is, H does not directly influence dislocation nucleation, either in terms of facilitating initial slip or interacting with the nascent dislocation(s). These findings suggest that rate-dependent processes, either associated with fluctuating nucleation or H transport, are necessary to interpret experimental observations of hydrogen-influenced reductions in the *pop-in* load.

6.2 Introduction

Hydrogen is an impurity often present in structural materials during production and service. The mechanical failure due to the deleterious effect of hydrogen is called hydrogen embrittlement (HE), which is a common problem for various structural metals and alloys [1-6]. It can cause catastrophic failure in load bearing metallic components and poses a serious challenge for material design in industries. Given its significant technological importance and industrial relevance, HE has been extensively studied both theoretically and experimentally. Various models have been proposed in the literature, including H-enhanced decohesion (HEDE) [7-12], H-enhanced local plasticity (HELP) [13-15], hydride formation and cleavage [16-18], and recently a model [19, 20] based on H-induced local "*ductile-to-brittle*" transition at the crack. All of these models have merits, but none fully captures the scope of Hydrogen-induced effects on the mechanical properties of metals. The precise HE mechanism(s) and relevant length and time scales, remain a topic of vigorous discussion [21].

In parallel, enormous efforts have been placed on developing accurate and efficient experimental methods in order to better capture and visualize the material behaviors during HE and other effects of Hydrogen on plastic flow. Besides the conventional HE index approach [22, 23] to examine HE at macroscopic scale, the local examination at the crack tip [14, 24-26] and the *in-situ* transmission electron microscope (TEM) examination of dislocations [27-30] are often used as means to probe the H effects at microscopic level. Another experimental approach to investigate the effects of Hydrogen on plasticity at small scales is instrumented nanoindentation (NI) [31, 32]. NI has the capacity to resolve dislocation nucleation in extremely small volumes [33-39], and has been extended by Barnoush and Vehoff [40] to *in-situ* electrochemical nanoindentation (ECNI).

In the NI/ECNI experiments, the material modulus and *pop-in* load are measured at fixed surface electrochemical potential. The presence of H is often found to reduce the *pop-in* load [40], although different effects are observed in different materials. The reduction has been attributed to reductions in dislocation line tension and/or shear modulus in the presence of H, which facilitate homogeneous dislocation nucleation (HDN). However the *pop-in* event during nanoindentation is a collective behavior corresponding to simultaneous burst of multiple dislocations, and is not directly HDN. Mechanistically, the reduction of line tension is envisioned due to segregation of H to dislocations, which would presumably not occur for HDN since no stable dislocation exists prior to the nucleation event. Thus, the origins of the reduction of *pop-in* load due to H remain unclear.

The role of various “side effects” associated with H charging, such as H-induced lattice swelling and vacancy crowding [41-43], on effecting the pop-in load have not been directly addressed in experiments. In a recent study [44], atomistic simulations studied how other pre-existing defects (vacancies and stacking fault tetrahedra) influence the nanoindentation response of single-crystal copper and showed that those structural defects can cause significant reductions in the *pop-in* load at low temperature. Thus, further investigation is required to elucidate the exact influence of H on nanoindentation response including its role in stabilizing other defects and, in general, understanding the onset of dislocation at more refined length and time scales.

In this paper, we employ molecular dynamics (MD) simulations to probe various direct and indirect effects of H on nanoindentation response at the atomic scale. Specifically, the force-displacement responses of Ni and Pd single crystals of different crystal orientations deformed under a rigid indenter are examined with and without interstitial H. We find very limited effects of H on the *pop-in* load, with the effects entirely explained by lattice dilation introduced by H such that there is no direct H effect on *pop-in*. The response after *pop-in* does not show any distinct role of H. We then discuss the implications of our results for mechanisms of observed effects of H on nanoindentation, pointing toward future directions for research in this area.

6.3 Computational methodology

We utilized large-scale MD simulations to examine the deformation behaviors of two model M-H systems (M=Ni, Pd) during nanoindentation. For each M-H system, two initial rectangular simulation cells, each consisting of a FCC M single crystal, with one oriented as $X = [\bar{1}10]$, $Y = [001]$ and $Z = [110]$, and the other oriented as $X = [\bar{1}10]$, $Y = [\bar{1}\bar{1}2]$ and $Z = [111]$ are created, where Z is the surface that will be indented. Sample dimensions are (L_x, L_y, L_z) being (28.0nm, 28.3nm, 14.5nm) and (28.0nm, 27.7nm, 14.6nm) for Ni-H, and (22.0nm, 20.8nm, 16.0nm) and (22.0nm, 20.9nm, 16.2nm) for Pd-H. Starting from each initial atomic configuration, several systems are created for simulations, as described below. In all case, the simulation cell is periodic along the *X* and *Y* directions, while free boundary condition is applied along *Z* direction, i.e., both top and bottom surfaces along *Z* are traction-free. The center of mass of the material is held fixed during the indentation to prevent rigid translational motions. Below, the *Z* direction is used to represent the crystal orientation.

With the above general information, we consider two types of samples. The first set of samples are metals charged with Hydrogen. H atoms are introduced by randomly inserting them into the octahedral sites in the M lattice to create an M-H system at a desired H concentration. The resultant M-H system is then relaxed within the NPT ensemble (*i.e.*, T = 300K, $\sigma_{xx} = \sigma_{yy} = 0$)

for 1.5 ns. Three M-H systems having 0%, 2% and 4% atomic H per M atom are studied for each crystal orientation, and are referred to as pure M, $MH_{0.02}$ and $MH_{0.04}$ systems, respectively. The second set of samples are Hydrogen-free systems subjected to an in-plane equi-biaxial strain prior to indentation. The initial simulation cell is first relaxed within the NPT ensemble (*i.e.*, $T = 300K$, $\sigma_{xx} = \sigma_{yy} = 0$) for 1.5ns. The simulation cell is then uniformly stretched/compressed along both X and Y directions to lattice strains ε from -0.9% to 1.4%.

All systems are then further relaxed in the NVT ensemble [45, 46] (*i.e.*, $T = 300K$) for 0.5ns to reach an equilibrium state. Nanoindentation is then conducted by moving a virtual spherical indenter with tip radius of 10 nm along the Z direction towards the material at a constant velocity of 10 m/s until the desired indentation depth is reached. The indenter is modeled as a *rigid* indenter using a strongly repulsive potential by Kelchner et al. [47]. During indentation, the linear momentum of the material along Z direction is reset to zero at every timestep and the force on the indenter and evolution of material microstructure is monitored. The lattice defects generated during deformation are quantitatively visualized using the common neighbor analysis (CNA) [48] and and the deformation index (DI) method by Wen et al. [49, 50].

For later reference, we also compute the elastic response of the M-H materials here. The shear modulus $\mu_{\mathrm{M(H)M}}$ associated with (111) shearing [51] as a function of H concentration c_{H} for Ni-H and Pd-H systems are shown in Figure 6.1. In both cases, $\mu_{\mathrm{M(H)M}}$ decreases approximately linearly with increasing H concentration. The decrease is not large, however: at $c_{\mathrm{H}} = 4\%$, the modulus decreases by ~4.5% for Ni and by ~8.5% for Pd.

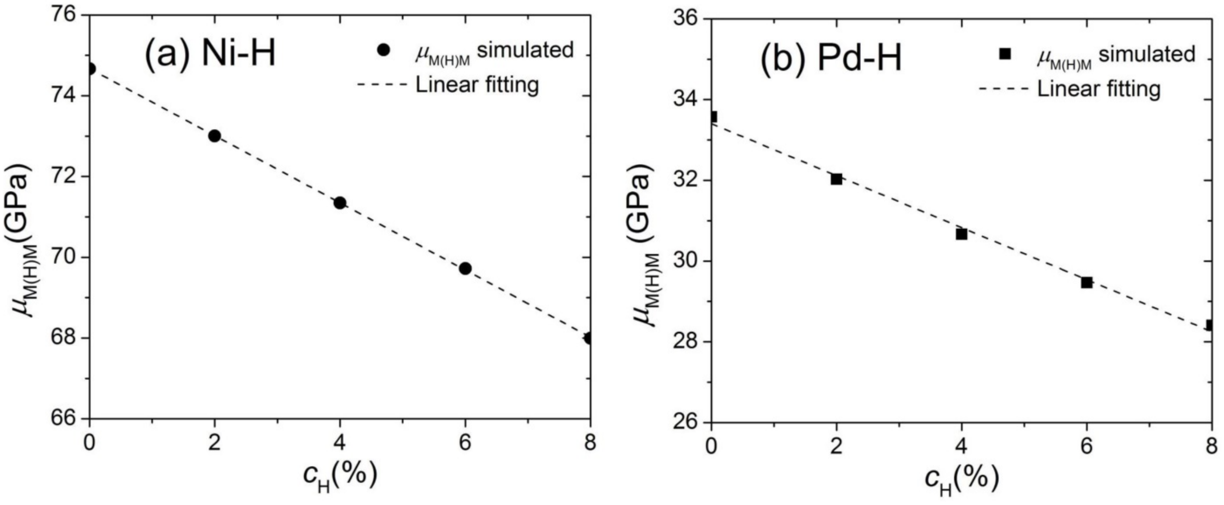

Figure 6.1. Shear modulus $\mu_{M(H)M}$ associated with (111) shearing [51] versus atomic H concentration c_H for (a) Ni-H and (b) Pd-H systems.

The MD simulations are performed using the LAMMPS code [52]. The system evolves using a Nosé–Hoover thermostat [46, 53] and velocity-Verlet algorithm [54] with integration time steps of 1 femtosecond (fs). The interatomic interactions in the Ni-H system are described using an embedded-atom-method (EAM) potential [55, 56] developed by Angelo et al. while the EAM potential developed by Zhou et al. is adopted for the Pd-H system in this study [57].

6.3 Results

6.3.1 Indentation of Ni-H and Pd-H

The load on the indenter F_z versus the indentation depth δ is shown in Figure 6.2 for the pure Ni, $NiH_{0.02}$ and $NiH_{0.04}$ systems, for both crystal orientations. All F_z vs. δ curves exhibit a range of load drops associated with dislocation nucleation, annihilation and exit from the free surface, for which the corresponding dislocation dynamics/reactions are well documented

[58-60]. In particular, the first load drop in F_z vs. δ corresponds to the onset of plasticity, i.e., the first dislocation nucleation event (HDN). We denote the point of the maximum force and displacement just prior to the first load drop as F_z^c and δ^c, which are effectively the *pop-in* load and the threshold indentation depth corresponding to the onset of plasticity in our computational indentation experiments. The insets to Figure 6.2 show the response around F_z^c and δ^c versus H concentration more clearly. In the elastic loading phase, the F_z vs. δ curves overlap, but the *pop-in* load, and thus the threshold indentation depth, decreases with increasing H concentration. After the first load drop, Figure 6.2 shows that the response at larger indentation depths is approximately independent of H concentration; that is, no distinct trend can be found in the magnitude or sequence of subsequent load drops. These results suggests that H facilitates the onset of plasticity (HDN), in agreement with the previous simulations by Wen et al. [49], but does not cause any subsequent softening effect at higher displacements as claimed by Wen et al. We return below to the origin of the apparent H reduction of the *pop-in* load below.

The indentation responses for the pure Pd, $PdH_{0.02}$ and $PdH_{0.04}$ systems are shown in Figure 6.3. Aside from an overall difference in magnitude of the loads at which plastic flow occurs, the general characteristics of the indentation behaviors of Pd and Pd-H systems are similar to the Ni and Ni-H systems. Therefore, the general effect of H among the two materials is solely to reduce the *pop-in* load with increasing H concentration.

The decrease in the *pop-in* load is also much larger than the reduction in shear modulus $\mu_{\mathrm{M(H)M}}$ (see Figure 6.1). Dislocation nucleation is expected to scale with shear modulus, so that the observed H influence on the *pop-in* load is not simply due to a change in elastic response of the material.

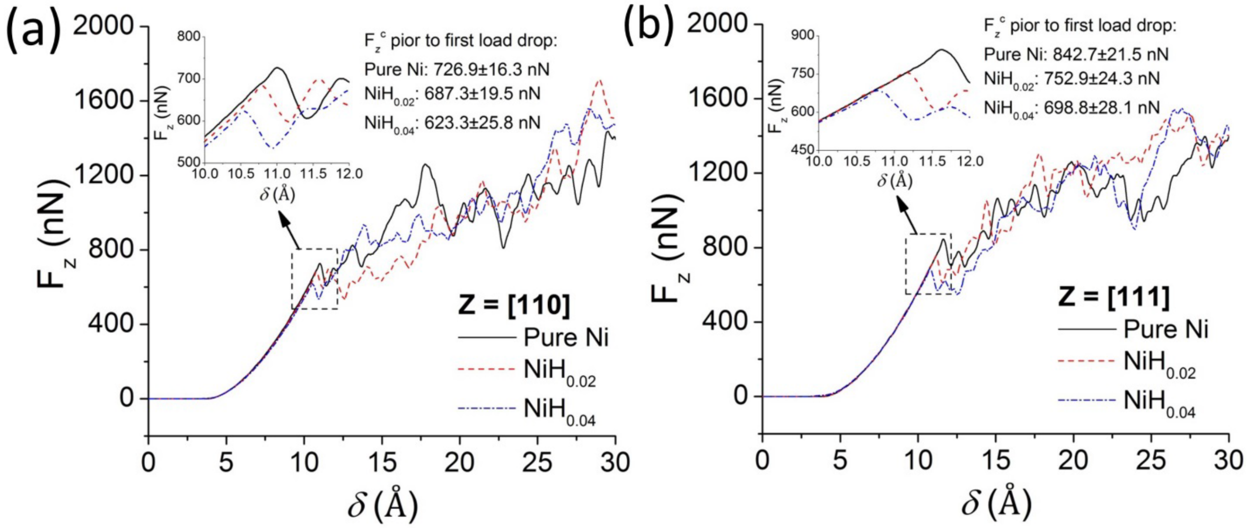

Figure 6.2. The load on indenter (F_z) versus indentation depth (δ) curves for the pure Ni (solid line), NiH$_{0.02}$ (dash line) and NiH$_{0.04}$ (dash dot line) systems with indentation direction (a) Z = [110] and (b) Z = [111]. The inserted figures show the close-up views of the curves around the point where the first load drop occurs.

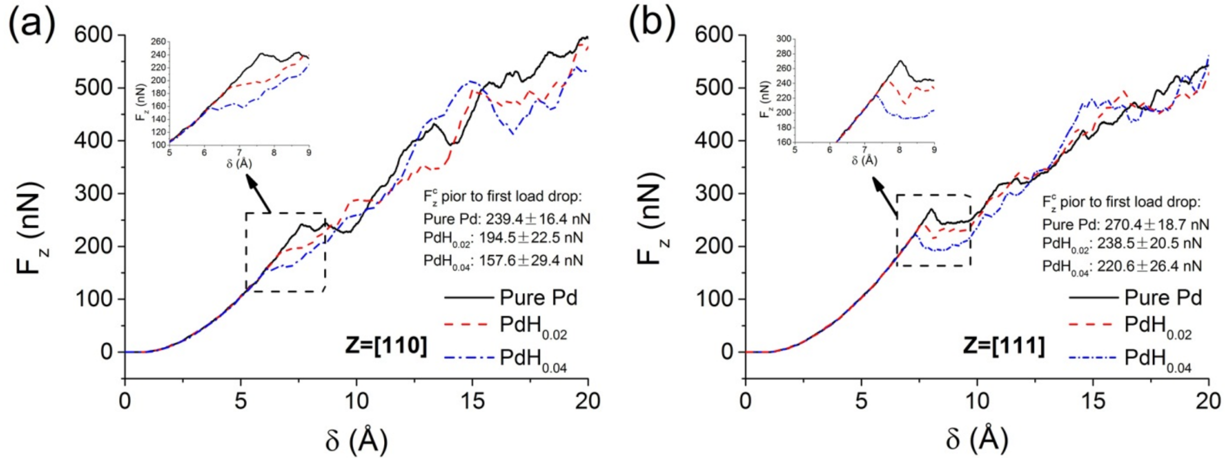

Figure 6.3. The load on indenter (F_z) versus indentation depth (δ) curves for the pure Pd (solid line), PdH$_{0.02}$ (dash line) and PdH$_{0.04}$ (dash dot line) systems with indentation direction (a) Z = [110] and (b) Z = [111]. The inserted figures show the close-up views of the curves around the point where the first load drop occurs.

6.3.2 Indentation of Pre-strained Ni and Pd

One consequence of H charging is an induced swelling of the lattice relative to the pure metal system. For H in octahedral sites of the fcc lattice, the induced swelling is nearly hydrostatic, associated with the misfit volume Ω_H for H in the host lattice. For a stress-free sample of initial volume V_0 and lattice constant a_0, the volume after charging to atomic concentration c_H is $V_0\left(1+\frac{4c_H\Omega_H}{a_0^3}\right)$. The associated hydrostatic misfit strain tensor is diagonal with components $\varepsilon_H = dV/V_0$, where dV is the volume change, so that $\varepsilon_H = \left(1+\frac{4c_H\Omega_H}{a_0^3}\right)^{1/3} - 1$.

For the Ni-H system, the simulation of a single H in a large Ni lattice yields, for the current interatomic potential, $\Omega_H = 0.075a_0^3$ ([56]). The predicted misfit strains are $\varepsilon_H = 0.20\%$ and 0.39% for c_H = 2% and 4%, respectively. The measured volume expansions in the simulations cells studied here correspond to ε_H = 0.18% and 0.37% for the $NiH_{0.02}$ and $NiH_{0.04}$. Similarly, in Pd, the simulation of a single H in a large Pd lattice yields, for the current interatomic potential, $\Omega_H = 0.085a_0^3$. The predicted values of ε_H are then 0.23% and 0.45% for $PdH_{0.02}$ and $PdH_{0.04}$, respectively, which again agree very well with the values measured in the simulation cells used for indentation, which show $\varepsilon_H = 0.21\%$ and 0.49%, respectively. The good agreement in both Ni and Pd shows that the volume expansion is well-understood within basic theory, and that there are no unusual H-H interactions, at low c_H, that might induce additional distortions.

As a consequence of the H-induced swelling, the Ni and Pd lattices are strained relative to the pure material, even in the absence of any applied boundary stresses in the simulations. We speculated that the lattice strains alone may change the *pop-in* load because the *pop-in* load can be interpreted as a measure of the point of absolute instability of the crystal lattice, which in turn is sensitive to the precise lattice constants and to the non-linear response of the crystal at large deformations [61]. To investigate the effects of lattice strain on nanoindentation behavior, entirely separated from any direct effects of H, we measured F_z vs. δ for pre-strained (in plane biaxial strain) Ni systems. The results are shown in Figures 6.4a-b for Ni and in Figures 6.5a-b for Pd. In all cases, a tensile lattice strain (dilation) reduces the *pop-in* load while a compressive lattice strain increases the *pop-in* load. The effect of pre-strain on the subsequent deformation/hardening behavior shows no systematic trends. Thus, the effect of lattice strains in the absence of H is qualitatively identical to the affects found in H-charged materials. Proceeding more quantitatively, Figures 6.4c-d and 6.5c-d show the measured *pop-in* load versus imposed lattice strain for Ni and Pd, respectively. The *pop-in* load is linearly dependent on the initial lattice strain over a wide range, deviating only at large compressive strains for the (111) orientation. Moreover, Figures 6.4c-d and 6.5c-d also show the measured *pop-in* loads for the H-charged samples at the lattice strains (expansions relative to the pure metal) induced by the presence of H. The *pop-in* loads for the H-charged specimens are nearly identical to those of the same samples without H but expanded to the same lattice strain.

The results in Figures 6.4 and 6.5 show that the behavior of Ni and Pd under indentation is determined by the lattice strain, and that the role of H is simply to induce a stress-free lattice strain (relative to the pure material). The presence of H has no further measurable effects, and hence no direct effects on dislocation nucleation or subsequent multiplication and hardening. That is, the effects of (immobile) H are indirect, arising only due to dilation of the lattice. We find no evidence of any direct H-enhanced dislocation nucleation or mobility, as claimed by Wen et al. [49]. The present simulations show that (immobile) H in otherwise defect-free materials does not have any direct influence on H-enhanced plasticity (e.g. the HELP mechanism).

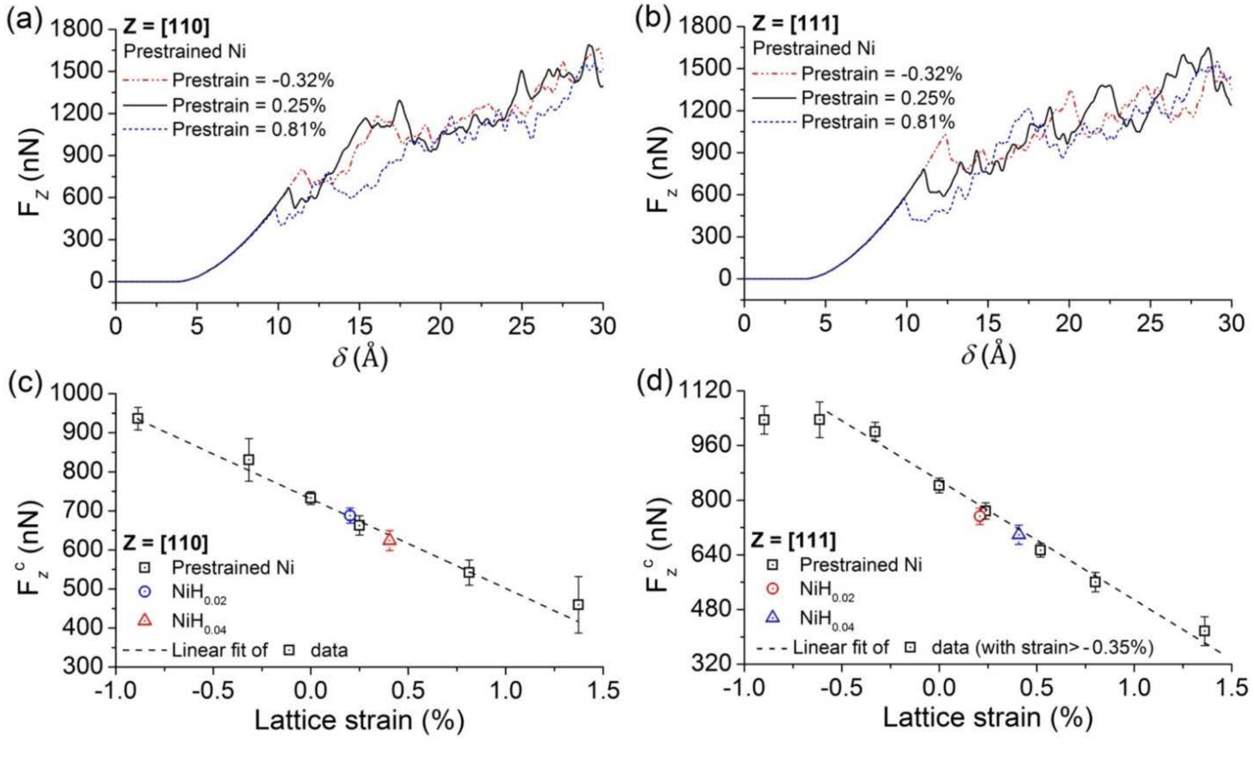

Figure 6.4. The load on indenter (F_z) versus indentation depth (δ) curves for three representative prestrained Ni systems with indentation direction (a) Z = [110] and (b) Z = [111], with (c) and (d) showing the corresponding load at the first load drop, F_z^{c} versus lattice strain plot for the prestrained Ni systems (squares) together with the F_z^{c} versus ε_{H} data for $\mathrm{NiH}_{0.02}$ (circle) and

$NiH_{0.04}$ (triangle), where the dashed line is a linear fitting of the square data (in particular for the case with Z=[111], only data with lattice strain > -0.35% are used in the fitting).

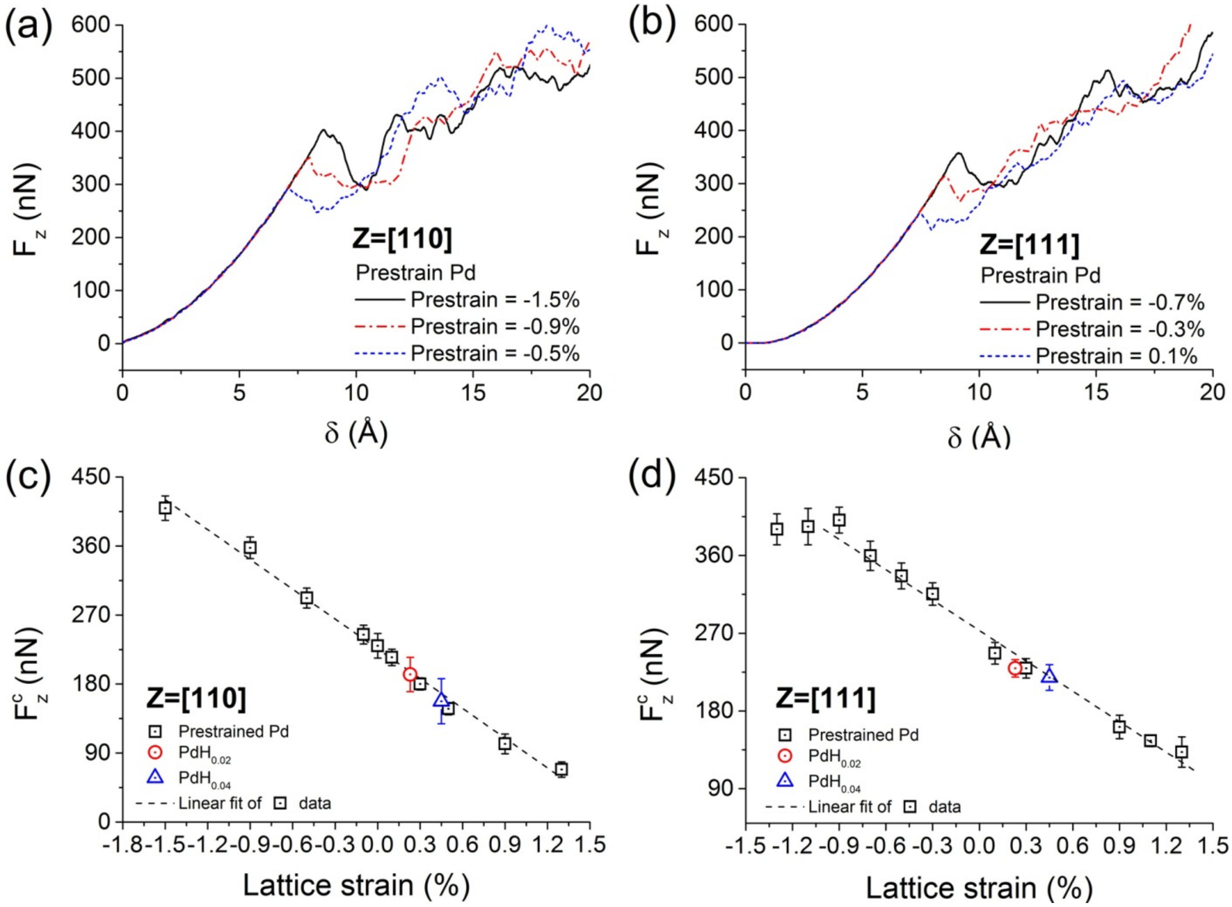

Figure 6.5. The load on indenter (F_z) versus indentation depth (δ) curves for three representative prestrained Pd systems with indentation direction (a) Z = [110] and (b) Z = [111], with (c) and (d) showing the corresponding load at the first load drop, F_z^c versus lattice strain plot for the prestrained Pd systems (squares) together with the F_z^c versus ε_H data for $PdH_{0.02}$ (circle) and $PdH_{0.04}$ (triangle), where the dashed line is a linear fitting of the square data.

6.3 Discussion

In-situ nanoindentation experiments on homogeneous dislocation nucleation (HDN) in Ni [33, 37, 39, 40] show a substantial reduction (e.g., ~51% reduction in the study by Barnoush and Vehoff [40]) in the *pop-in* load following H charging. This is often interpreted as evidence for strong H-dislocation interactions that facilitate the onset of plastic deformation. Our simulations for defect free metals having random H that does not migrate during the duration of the simulation, show that the only effects of H can be attributed to lattice dilation induced by the H. Our results are independent of host metal, for Ni and Pd, and independent of crystal orientation, for [110] and [111] loadings. There is a small reduction in *pop-in* load, but the magnitude is not at all comparable to experiments, and the H concentrations in the simulations and experiments are expected to be comparable. The difference between experiments and simulations indicates that the deformation behavior in experiments involves either rate-dependent processes or processes that involve other defects, or both.

The primary rate-dependent process that could be anticipated is H diffusion during the duration of the experiment. H diffusion in Ni occurs with a migration barrier of ~0.4 eV; this is slow compared to Fe, but yields a mean square diffusion distance at 300K of ~350nm. Thus, it is feasible for H to diffuse in and around the region under stress during nanoindentation. However, if the experiments truly measure HDN in regions of initially dislocation-free material, then there are no initial dislocations toward which H could migrate. At finite temperature, there can be sub-critical dislocation loops that arise as thermal fluctuations, but being fluctuations they do not persist for long periods. Thus, H would have to diffuse sporadically, in response to only the pressure field generated by the fluctuating loops that appear and disappear. Counteracting the possible attraction to such fluctuation loops, however, is the driving force for H diffusion away from regions of high compressive stress. With a positive misfit volume Ω_H, the increase in chemical potential, relative to bulk H, due to a local compressive pressure of p = 2 GPa (the estimated pressure underneath the indenter at the experimentally-measured *pop-in* load) is $d\mu = p\Omega_H = 0.041\ \text{eV}$, which drives H away from the region where dislocation nucleation is expected. Experiments further show that when a sample is loaded first and then subsequently charged with H, the *pop-in* load is again reduced relative to the H-free samples. With an increased chemical potential underneath the loaded indenter, the diffusion of H into this region is delayed and the equilibrium concentration is reduced. Therefore, it is difficult to envision that HDN is caused only by mobile H in the bulk lattice.

As mentioned in the Introduction, the presence of defects can reduce the *pop-in* load. If the *pop-in* load is reduced only in the presence of H, then presumably H must stabilize some defects that would not exist in the absence of H. It is well-established that H can bind to vacancies, so that vacancy clusters are stabilized in the presence of H. It is thus possible, in principle, that the presence of H could allow for the formation of stable V_nH_m complexes that would not exist in the H-free material, and that such complexes could serve as nucleation sites for HDN. Preliminary simulations show that vacancy clusters (with or without H) artificially placed underneath the indenter can indeed reduce the *pop-in* load to ~ 2/3 the value in the pure Ni. However, the actual probability of finding such clusters under thermodynamic equilibrium conditions remains quite small. Taking the Ni system as an example, for the interatomic potential here the formation energy of a VH_6 cluster is 0.51 eV (as compared to 1.59 eV for an isolated V), so that the zero-pressure equilibrium concentration of VH_6 at T=300K is estimated to be only ~2×10^{-9}. Thus, one would expect to find one such cluster in every volume of ~ (175 nm)^3 in Ni, which is much larger than the volume probed underneath the nanoindenter. Furthermore, although the misfit volume for a V is negative, the misfit volume for a VH_6 complex is large and positive. Underneath the high pressure of the indenter, the formation enthalpy of the VH_6 complex is thus much higher than at zero pressure, making such complexes thermodynamically even less likely underneath the indenter. Such complexes would have to form prior to the imposition of the indentation load and then, for kinetic reasons, remain stable against dissociation during loading. Since experiments show reduced *pop-in* when the load is imposed prior to charging, this latter scenario does not seem feasible as an explanation of the observed effects.

The above discussion is meant to highlight the fact that the role of H, its presence underneath the indenter, and its role in possibly stabilizing other defects, involves a complicated consideration of kinetic and thermodynamic effects. Any proposed mechanism to explain the experimentally-observed reduction in *pop-in* load upon H charging cannot simply rely on postulated defects or configurations, but must also consider the thermodynamic and kinetic effects that determine the likelihood/probability of occurrence of such postulated defects. This challenge has yet to be undertaken in this field but appears essential for viable physical explanation of the observed phenomena.

6.4 Acknowledgements

The authors acknowledge support of this work by the NSERC Discovery grant (grant # RGPIN 418469-2012) and by the Swiss National Foundation through a grant for the project entitled "Predictive Mechanisms of Hydrogen Embrittlement" (project # 200021-149207).

6.5 References

[1] Rogers H. Hydrogen Embrittlement of Metals: Atomic hydrogen from a variety of sources reduces the ductility of many metals. Science 1968;159:1057-64.
[2] Merrick R. An overview of hydrogen damage to steels at low temperatures. Mater Performance;(United States) 1989;28.
[3] Figueroa-Gordon DJ. Hydrogen re-embrittlement susceptibility of ultra high strength steels: Cranfield University; 2005.
[4] Rhodes P, Skogsberg L, Tuttle R. Pushing the limits of metals in corrosive oil and gas well environments. Corrosion 2007;63:63-100.
[5] Koyama M, Akiyama E, Tsuzaki K. Hydrogen embrittlement in a Fe–Mn–C ternary twinning-induced plasticity steel. Corrosion Science 2012;54:1-4.
[6] Nagao A, Smith CD, Dadfarnia M, Sofronis P, Robertson IM. The role of hydrogen in hydrogen embrittlement fracture of lath martensitic steel. Acta Materialia 2012;60:5182-9.
[7] Troiano AR. The role of hydrogen and other interstitials in the mechanical behavior of metals. Trans ASM 1960;52:26.
[8] Oriani RA. A mechanistic theory of hydrogen embrittlement of steels. Berichte der Bunsengesellschaft für physikalische Chemie 1972;76:848-57.
[9] Oriani RA, Josephic PH. Equilibrium aspects of hydrogen-induced cracking of steels. Acta Metallurgica 1974;22:1065-74.
[10] Gerberich W, Foecke T. Hydrogen Enhanced Decohesion in Fe--Si Single Crystals: Implications to Modeling of Thresholds. Hydrogen Effects on Material Behavior 1989:687-702.
[11] Rice JR, Wang J-S. Embrittlement of interfaces by solute segregation. Materials Science and Engineering: A 1989;107:23-40.
[12] Gerberich W, Marsh P, Hoehn J. Hydrogen induced cracking mechanisms—are there critical experiments? Hydrogen effects in materials 1996:539-54.
[13] Beachem CD. A new model for hydrogen-assisted cracking (hydrogen “embrittlement”). MT 1972;3:441-55.
[14] Birnbaum HK, Sofronis P. Hydrogen-enhanced localized plasticity—a mechanism for hydrogen-related fracture. Materials Science and Engineering: A 1994;176:191-202.

[15] Robertson IM. The effect of hydrogen on dislocation dynamics. Engineering Fracture Mechanics 2001;68:671-92.

[16] Hohenberg P, Kohn W. Inhomogeneous electron gas. Physical review 1964;136:B864.

[17] Gahr S, Grossbeck ML, Birnbaum HK. Hydrogen embrittlement of Nb I—Macroscopic behavior at low temperatures. Acta Metallurgica 1977;25:125-34.

[18] Shih DS, Robertson IM, Birnbaum HK. Hydrogen embrittlement of α titanium: In situ tem studies. Acta Metallurgica 1988;36:111-24.

[19] Song J, Curtin WA, Bhandakkar TK, Gao HJ. Dislocation shielding and crack tip decohesion at the atomic scale. Acta Materialia 2010;58:5933-40.

[20] Song J, Curtin WA. Atomic mechanism and prediction of hydrogen embrittlement in iron. Nat Mater 2013;12:145-51.

[21] Gangloff RP, Somerday BP. Gaseous hydrogen embrittlement of materials in energy technologies: mechanisms, modelling and future developments: Elsevier; 2012.

[22] Zmudzinski C, Blondeau R, Bretin L, Toitot M. The Influence of a Hydrogen Atmosphere on the Metallurigcal Behaviour of Steels Used in Pressure Vessels. Mem Sci Rev Metall 1978;75:571-80.

[23] Zmudzinski C, Pressouyre G, Bretin L. Optimization of steels likely to be subjected to hydrogen action. Commission of the European Communities, Synopsis of Results of the First Programme on the Production and Utilization of Hydrogen 1982:525-47.

[24] Vehoff H, Neumann P. Crack propagation and cleavage initiation in Fe-2.6%-Si single crystals under controlled plastic crack tip opening rate in various gaseous environments. Acta Metallurgica 1980;28:265-72.

[25] Vehoff H, Klameth H-K. Hydrogen embrittlement and trapping at crack tips in Ni-single crystals. Perspectives in Hydrogen in Metals: Elsevier; 1986. p. 661-8.

[26] Vehoff H, Rothe W. Gaseous hydrogen embrittlement in FeSi-and Ni-single crystals. Perspectives in Hydrogen in Metals: Elsevier; 1986. p. 647-59.

[27] Teter D, Ferreira P, Robertson I, Birnbaum H. An environmental cell TEM for studies of gas-solid interactions. New techniques for characterizing corrosion and stress corrosion Clevland, Ohio: TMS, Warrendale, Pa 1995:53-72.

[28] Ferreira P, Robertson IM, Birnbaum H. Influence of hydrogen on the stacking-fault energy of an austenitic stainless steel. Materials Science Forum: Trans Tech Publ; 1996. p. 93-6.

[29] Ferreira PJ, Robertson IM, Birnbaum HK. Hydrogen effects on the interaction between dislocations. Acta Materialia 1998;46:1749-57.

[30] Ferreira PJ, Robertson IM, Birnbaum HK. Hydrogen effects on the character of dislocations in high-purity aluminum. Acta Materialia 1999;47:2991-8.

[31] Katz Y, Tymiak N, Gerberich WW. Nanomechanical probes as new approaches to hydrogen/deformation interaction studies. Engineering Fracture Mechanics 2001;68:619-46.

[32] Golovin YI. Nanoindentation and mechanical properties of solids in submicrovolumes, thin near-surface layers, and films: a review. Physics of the solid State 2008;50:2205-36.

[33] Bahr D, Field D, Nibur K, Morasch K. Hydrogen and deformation: Nano-and microindentation studies. JOM 2003;55:47-50.

[34] Glowacka A, Wozniak MJ, Swiatnicki W. Nanoindentation measurements of austeno-ferritic stainless steel submitted to hydrogen charging. Reviews on Advanced Materials Science 2004;8:66-8.

[35] Gao X. Displacement burst and hydrogen effect during loading and holding in nanoindentation of an iron single crystal. Scripta materialia 2005;53:1315-20.

[36] Durst K, Backes B, Franke O, Göken M. Indentation size effect in metallic materials: Modeling strength from pop-in to macroscopic hardness using geometrically necessary dislocations. Acta Materialia 2006;54:2547-55.

[37] Nibur KA, Bahr DF, Somerday BP. Hydrogen effects on dislocation activity in austenitic stainless steel. Acta Materialia 2006;54:2677-84.

[38] Barnoush A, Yang B, Vehoff H. Effect of hydrogen and grain boundaries on dislocation nucleation and multiplication examined with a NI-AFM. Advances in Solid State Physics: Springer; 2008. p. 253-69.

[39] Zhang L, An B, Fukuyama S, Yokogawa K. Hydrogen effects on localized plasticity in SUS310S stainless steel investigated by nanoindentation and atomic force microscopy. Japanese Journal of Applied Physics 2009;48:08JB.

[40] Barnoush A, Vehoff H. Recent developments in the study of hydrogen embrittlement: Hydrogen effect on dislocation nucleation. Acta Materialia 2010;58:5274-85.

[41] Fukai Y, Shizuku Y, Kurokawa Y. Superabundant vacancy formation in Ni–H alloys. Journal of alloys and compounds 2001;329:195-201.

[42] Zhang C, Alavi A. First-principles study of superabundant vacancy formation in metal hydrides. Journal of the American Chemical Society 2005;127:9808-17.

[43] Fukai Y. The metal-hydrogen system: basic bulk properties: Springer Science & Business Media; 2006.

[44] Salehinia I, Bahr D. The impact of a variety of point defects on the inception of plastic deformation in dislocation-free metals. Scripta Materialia 2012;66:339-42.

[45] Nosé S. A molecular dynamics method for simulations in the canonical ensemble. Molecular physics 1984;52:255-68.

[46] Nosé S. A unified formulation of the constant temperature molecular dynamics methods. The Journal of chemical physics 1984;81:511-9.

[47] Kelchner CL, Plimpton S, Hamilton J. Dislocation nucleation and defect structure during surface indentation. Physical review B 1998;58:11085.

[48] Honeycutt JD, Andersen HC. Molecular dynamics study of melting and freezing of small Lennard-Jones clusters. Journal of Physical Chemistry 1987;91:4950-63.

[49] Wen M, Zhang L, An B, Fukuyama S, Yokogawa K. Hydrogen-enhanced dislocation activity and vacancy formation during nanoindentation of nickel. Physical Review B 2009;80:094113.

[50] Wen M, Li Z. Thermally activated process of homogeneous dislocation nucleation and hydrogen effects: An atomistic study. Computational Materials Science 2012;54:28-31.

[51] Zimmerman JA, Gao H, Abraham FF. Generalized stacking fault energies for embedded atom FCC metals. Modelling and Simulation in Materials Science and Engineering 2000;8:103.

[52] Plimpton S. Fast parallel algorithms for short-range molecular dynamics. Journal of computational physics 1995;117:1-19.

[53] Hoover WG. Canonical dynamics: equilibrium phase-space distributions. Physical review A 1985;31:1695.

[54] Swope WC, Andersen HC, Berens PH, Wilson KR. A computer simulation method for the calculation of equilibrium constants for the formation of physical clusters of molecules: Application to small water clusters. The Journal of Chemical Physics 1982;76:637-49.

[55] Daw MS, Baskes MI. Embedded-atom method: Derivation and application to impurities, surfaces, and other defects in metals. Physical Review B 1984;29:6443.

[56] Angelo JE, Moody NR, Baskes MI. Trapping of hydrogen to lattice defects in nickel. Modelling and Simulation in Materials Science and Engineering 1995;3:289.

[57] Zhou X, Zimmerman JA, Wong BM, Hoyt JJ. An embedded-atom method interatomic potential for Pd–H alloys. Journal of Materials Research 2008;23:704-18.

[58] Cha P-R, Srolovitz DJ, Vanderlick TK. Molecular dynamics simulation of single asperity contact. Acta Materialia 2004;52:3983-96.

[59] Song J, Srolovitz D. Adhesion effects in material transfer in mechanical contacts. Acta materialia 2006;54:5305-12.

[60] Song J, Srolovitz DJ. Atomistic simulation of multicycle asperity contact. Acta Materialia 2007;55:4759-68.

[61] Zhu T, Li J, Van Vliet KJ, Ogata S, Yip S, Suresh S. Predictive modeling of nanoindentation-induced homogeneous dislocation nucleation in copper. Journal of the Mechanics and Physics of Solids 2004;52:691-724.

Chapter 7: Atomistic Investigation of Hydrogen Diffusion at Dislocations in Structural Metals

In Chapter 6, the influence of hydrogen on mechanical response of metals was examined by molecular dynamics simulations. Our results discovered hydrogen can facilitate dislocation nucleation, reflected by the reduction of *pop-in* load in nanoindentation process, which originates from the lattice dilation caused by hydrogen. However, another unsolved issue is how hydrogen interplays with dislocations at the atomic scale when dislocation pre-existed in metals. Therefore, this chapter quantitatively evaluated the energetics and kinetics of hydrogen in the vicinity of dislocations using molecular statics simulations and kinetic activation-relaxation technique. Hydrogen segregation and diffusion behaviors at dislocations were systematically studied. The possibility of short-circuit and pipe diffusion at dislocations was clarified finally.

This chapter shall be submitted as: **Atomistic investigation of hydrogen diffusion at dislocations in structural metals**, Xiao Zhou, Normand Mousseau, W.A. Curtin, Jun Song

7.1 Abstract

The energetics and kinetics of hydrogen at dislocations in structural metals were systematically investigated by molecular static (MS) simulations and the kinetic Activation-Relaxation Technique (k-ART) simulations over long timescale. It was found both edge and screw dislocations in examined fcc Ni and bcc Fe are treated as strong trapping sites for hydrogen. Moreover, our results suggested hydrogen can only transport within short range over short timescale (i.e., short circuit diffusion) and cannot diffuse along dislocation line direction over long timescale (i.e., pipe diffusion). This constraint of hydrogen diffusion and the vanishment of pipe diffusion are attributed to the fact that there is no continue fast diffusion pathway at dislocations, confirmed by both k-ART simulations and nudged elastic band (NEB) calculations. The present study clarified short circuit and pipe diffusion of hydrogen at dislocations, providing some new insights towards better understanding hydrogen kinetics in microstructural heterogeneities.

7.2 Introduction

The interaction between hydrogen (H) and microstructures is a key aspect in understanding hydrogen embrittlement (HE), a phenomenon where H presence renders ductile metals and alloys prone to premature and brittle failure [1-5]. Microstructures provide interstitial sites of low-energy states for H, thus favoring local H segregation and accumulation [6-12]. Meanwhile, it has been long postulated that microstructures, such as dislocations and grain boundaries, can provide fast diffusion pathways to accelerate H transport. In particular, for dislocations, the main microstructural entities responsible for plastic deformation, it is suggested by many studies that H would enjoy fast diffusion along the dislocation line direction, called dislocation pipe diffusion, regarded as one mechanism responsible for enhanced H diffusivity in deformed metal samples [13-16]. For instance, the occurrence of pipe diffusion in deformed Pd was observed in experiment by Heuser [17]. Tang et al. performed molecular static (MS) simulations and indicated the migration barrier of H along dislocation line is relatively low in Ni, meaning that pipe diffusion would take place [18]. Schiavone et al. did *ab-initio* calculations and demonstrated that there exist fast diffusion tunnels with low energy barriers in dislocation core in Pd [19].

However, the controversial results still exist in the literature where some studies asserted that H atoms would be blocked rather than fast diffusion [20, 21]. For instance, Iwaoka et al. noted H diffusion at dislocation region in ultrafine-grained Pd is strongly retarded due to the strong trapping effect [22]. Kimizuka et al. carried out molecular dynamics (MD) simulations and discovered that both screw and edge dislocation in α-iron resist H pipe diffusion [23]. Therefore, better understanding of H kinetics in dislocations necessitates more studies to clarify H-dislocation interactions at the atomic scale. In this regard, atomistic simulations are performed to investigate H diffusion behaviors at dislocations in metals (i.e., fcc Ni and bcc Fe). Firstly, H energetics and trapping tendency in the vicinity of dislocations are examined. Meanwhile, H kinetics within the region of dislocation is studied. Distinct mechanisms and migration pathways of H are identified within dislocation cores. In the end, the effect of dislocation core structure on H diffusion behaviors is discussed.

7.3 Computational methodology

In our study, fcc Ni and bcc Fe were chose as two representative modeling systems. As for Ni-H system, the simulation box composed of fcc Ni crystal orientated as $x=[110]$, $y=[1\bar{1}1]$ and $z=[1\overline{12}]$ was built up and the dimensions of edge and screw dislocation were 102×121×51 Å and 50×122×130 Å respectively. For Fe-H system, we construct the rectangular simulation box consisted of bcc Fe crystal oriented as $x=[111]$, $y=[1\bar{1}0]$ and $z=[11\bar{2}]$, with dimensions of edge and screw dislocation being 129×113×56 Å and 54×121×126 Å. All edge and screw dislocations were introduced at the center of simulation boxes by means of anisotropic elastic displacement fields [24]. In particular, the simulation box with perfect lattice was fist created, after which the extra displacement based anisotropic elastic displacement fields was added in each atom. Periodic boundary conditions were used along dislocation line direction and dislocation slip direction. Free boundary conditions were employed along the direction that is perpendicular to both dislocation line and slip directions. The schematic illustration of simulation cells can be seen in Figure 7.1.

It should be noted that the high fidelity interatomic potentials play the dominant role in determining the accuracy and reliability of atomic simulations. In this work, we employed the interatomic potentials using embedded-atom method (EAM) to describe H-metal interaction. In particular, the EAM potential developed by Baskes et al. was used for the Ni-H system where this potential gives a good description of many properties of the Ni-H system and has been successfully applied to H-dislocation interaction [25]. For Fe-H system, the atomic interplays are described by means of the EAM potential developed by Ramasubramaniam et al. [26]. This potential shows high agreement with the results of Fe-H interaction calculated by *ab-initio* calculations. In addition, this potential can correctly characterize the dislocation core structure without and with the presence of H.

H kinetics and diffusion behaviors in the vicinity of dislocations in both Ni and Fe were studied by Kinetic Monte Carlo (KMC) simulations. In particular, we adopted the versatile on-the-fly off-lattice KMC method (i.e., k-ART) in this study. k-ART is a powerful technique that has the capability of dealing with complex material systems and long-range elastic deformation effect [27, 28]. Furthermore, k-ART has been demonstrated to give us sufficient atomic details regarding kinetic process over long time evolution, which is a nuisance in standard atomistic simulations (i.e., MD simulation) because of the limitation in timescale. In k-ART simulations, the threshold for force convergence was set to 0.05 eV/Å. The topological radius of cluster searching was set to 6.0 Å. The maximum and minimum cut-off distance used when searching the secondary topologies was 2.6 Å and 2.2 Å respectively. In the end, MS simulations with nudged elastic band (NEB) [29, 30] method was employed to study the energy landscapes and barriers of H transporting at dislocations, so as to provide atomic details aside from k-ART simulations. The combination of k-ART and MS simulations would help us reveal the mechanisms of H diffusion at dislocations at the atomic scale.

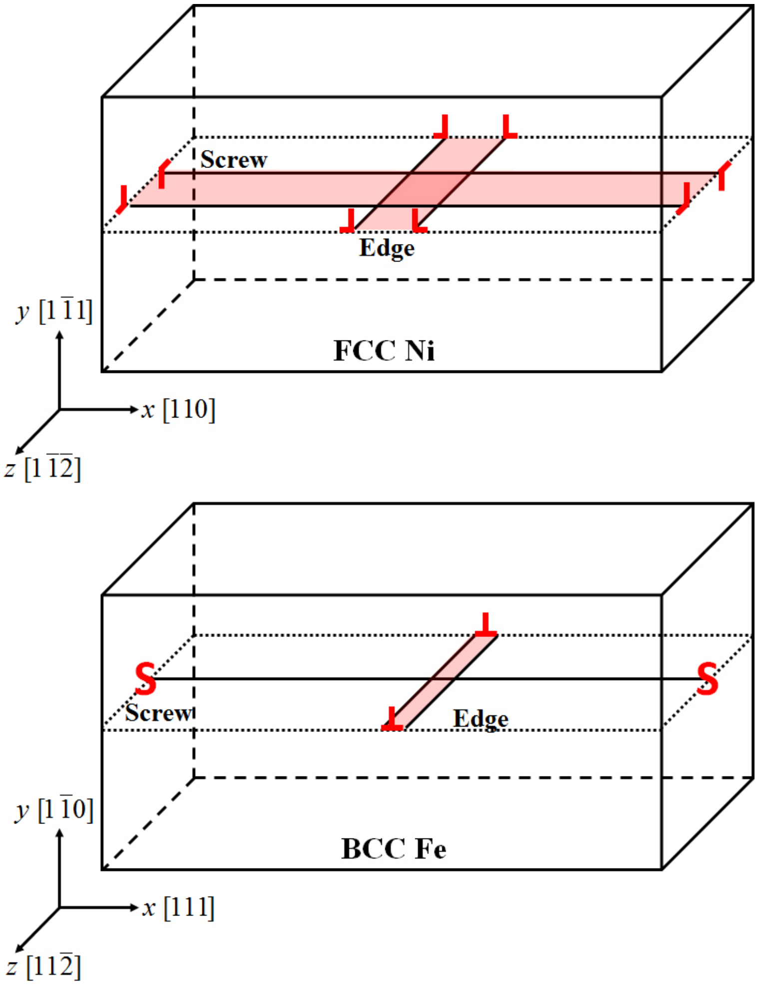

Figure 7.1. Schematic illustration of the simulation cells containing edge and screw dislocations in fcc Ni and bcc Fe.

7.4 Results and discussion

7.4.1 H-dislocation interactions

In this part, we first carried out MS simulations to examine the H energetics trapped around dislocations in selected metal systems. The trapping state of H around dislocations can be quantitatively assessed by binding energy, defined as:

$$E_b = E_H^{dis} - E^{dis} - E_H^{bulk} + E^{bulk} \tag{7.1}$$

where E_H^{dis} is the total energy of the system with dislocation and a H atom residing in the region of dislocation, E^{dis} is the total energy of the pristine dislocation system without H atom. E_H^{bulk} is the total energy of the reference bulk system with a H atom occupying at octahedral site for Ni and tetrahedral site for Fe respectively, and E^{bulk} is the total energy of pure bulk system without H atom. In this definition, the positive and negative value of binding energy suggests repulsion and attraction between H and dislocation, respectively. In our MS simulations, we selected hydrogen atom as probe and used the three dimensional mesh with the node of mesh being initial hydrogen trapping position (the separated distance between two adjacent nodes was set to 0.2 Å). Then we performed energy minimization and calculated the binding energy based on three dimensional mesh. Finally we can obtain and plot the binding energy map in space.

- *H trapping around dislocations in fcc Ni*

With regard to edge dislocation in fcc Ni, the local atomic structure and potential trapping sites of H around edge dislocation are shown in Figure 7.2. It is well expected that the edge dislocation in fcc Ni has a dissociated core structure where the dissociated edge dislocation contains the stacking fault region and the Shockley partial dislocation. Due to the variety of local atomic structure, the potential trapping sites of H are located in three different areas of edge dislocation, marked by top layer, middle layer and bottom layer in Figure 7.2a. The binding energy spectrum of H trapped around edge dislocation is shown in Figure 7.2b. We find that the strong trapping sites of H mainly stay in the middle layer (stacking fault region) and bottom layer (tension region below Shockley partial core) due to the negative binding energies. However, considering other positions in the top layer, the calculated binding energies are positive, indicating H atom is energetically unfavorable in those sites and no trapping propensity. In addition, the binding energies as a function of H position along dislocation slip direction in the bottom layer and along the direction normal to dislocation slip plane are also calculated, as illustrated in Figure 7.2b. It is found when H atom resides in the bottom layer and is far from Shockley partial dislocation, the binding energy is -0.05 eV, indicative of weak trapping effect. With H atom moves towards Shockley partial dislocation, the binding energy gradually decreases and then reaches the lowest value (i.e., -0.15 eV). Our calculated results are in well agreement with other work in the literature [18].

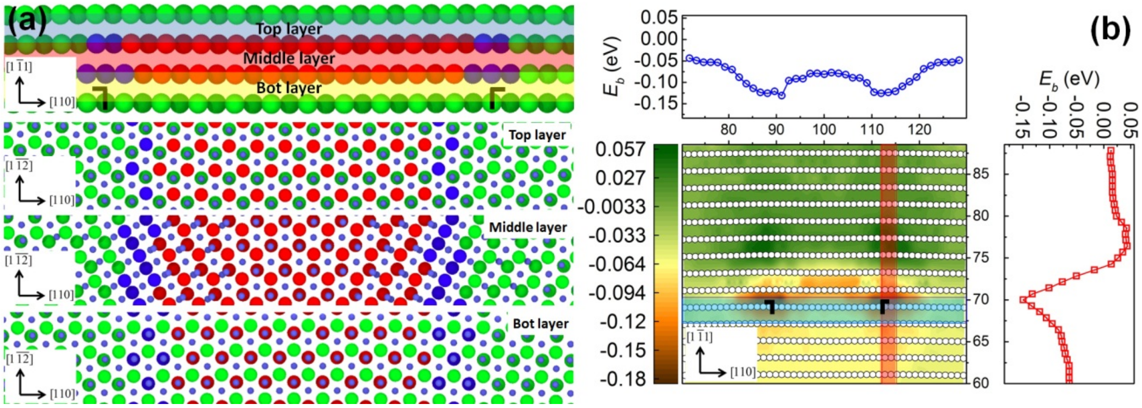

Figure 7.2. (a) Atomic configuration of edge dislocation and possible H trapping site. The big green ball shows perfect fcc bulk lattice, the big blue ball represents Shockley partial core and the big red ball shows stacking fault region. The small blue ball represents H trapping site. (b) Binding energy map of H at edge dislocation in fcc Ni. Top curve in (b) is the binding energy profile along the dislocation slip direction in bottom layer, as illustrated by blue strip in the map. Right curve in (b) is the binding energy of H along the direction normal to dislocation slip direction, as marked by red strip in the map.

As for screw dislocation in fcc Ni, the core structure is also dissociated and comprised of stacking fault region and Shockley partial dislocation, which is similar to edge dislocation (see Figure 7.3). In Figure 7.3a, three different regions (i.e., top layer, middle layer and bottom layer) with respect to the possible H trapping positions are well defined. The binding energy map of H at screw dislocation is illustrated in Figure 7.3b. It is easy to note that the most energetically preferable site for H is located in the region of stacking fault in the middle layer and in the tension region of Shockley partial dislocation (i.e., bottom layer in left partial core and top layer in right partial core due to the fact that two Shockley partial cores have opposite sign). For H atom in the middle layer along dislocation slip direction, the binding energy gradually decreases and finally descends to the lowest value (~ -0.07 eV). Meanwhile, as for the tension region of Shockley partial core, the lowest binding energy is ~ -0.08 eV. Therefore, our results demonstrate Shockley partial cores at both edge and screw dislocations can be seen as strong trapping sites.

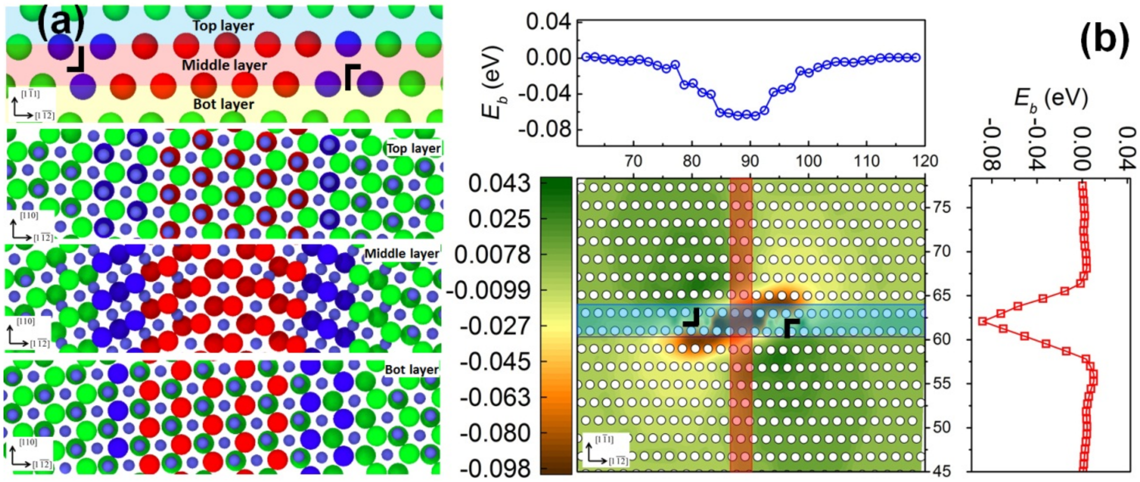

Figure 7.3. (a) Atomic configuration of screw dislocation and H trapping sites. (b) Binding energy map of H at screw dislocation in fcc Ni. Top subfigure in (b) is the binding energy as a function of H position in middle layer along slip direction, as demonstrated by blue strip in the map. Right subfigure in (b) is the binding energy profile of H along the direction normal to dislocation slip direction, as highlighted by red strip in the map.

- *H trapping around dislocations in bcc Fe*

Aside from H-Ni system, the interactions between H and dislocations in bcc Fe were studied in this section. The local atomic arrangement of edge dislocation, potential trapping sites and binding energies of H at edge dislocation of bcc Fe are shown in Figure 7.4. Unlike the edge dislocation of Ni, H atom only prefers to stay in the middle and bottom layer defined in Figure 7.4a. The binding energy of H in the middle layer and bottom layer exhibits negative value, with the minimum one being -0.36 eV. However, for the sites above the glide plane (glide plane is middle layer in Figure 7.4a), the binding energy exhibits positive 0.038 eV, indicative of it being energetically unfavorable .

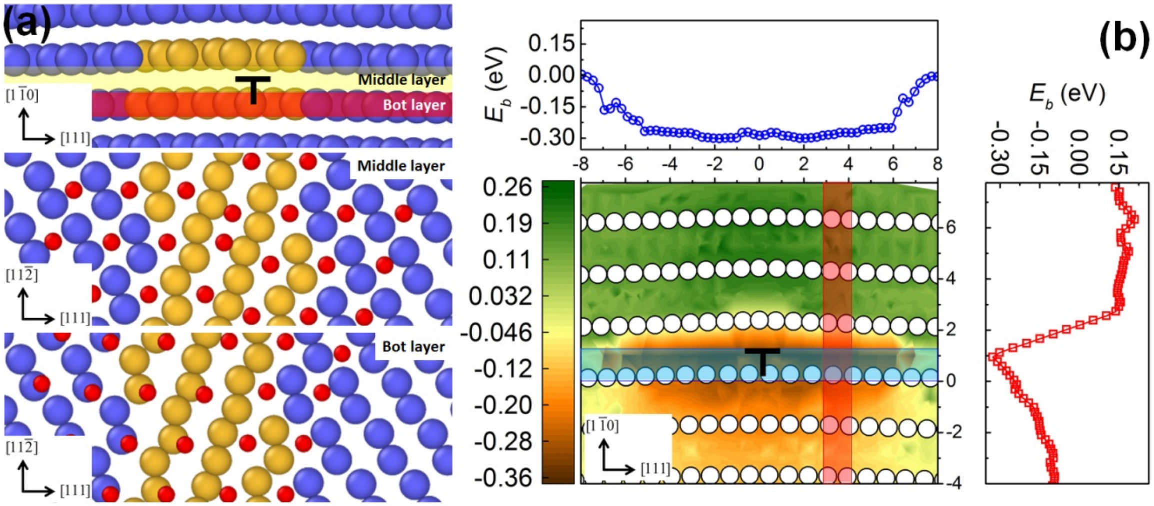

Figure 7.4. (a) Atomic configuration of edge dislocation and H trapping site in bcc Fe. The big blue balls are bcc bulk-like Fe atoms, big brown balls are non bulk-like Fe atoms at dislocation core region and small red balls are H trapping sites. (b) Binding energy map of H at edge dislocation in bcc Fe. Top subfigure in (b) describes the binding energy as a function of H position in bottom layer along glide direction, as demonstrated by blue strip in the map. Right subfigure in (b) is the binding energy profile of H along the direction normal to dislocation slip direction, as illustrated by red strip in the map.

With regard to screw dislocation of bcc Fe, the local atomic structure, possible trapping sites and calculated binding energies of H at core region are depicted in Figure 7.5. It is worth emphasizing that the core structure in bcc Fe is correctly predicted using EAM potential where the screw dislocation maintains sixfold symmetry even in the presence of H atoms. We also noted the trapping sites of H are not located exactly in the center of core region (small red balls in Figure 7.5a). Instead, the energetically preferable sites are located near the dislocation core center, which are marked by small green balls in Figure 7.5a. The binding energy map of H at screw dislocation is demonstrated in Figure 7.5b. where the strongest trapping site exhibits the minimum binding energy of -0.25 eV, which is consistent with other simulated results in the literature [23]. In addition, There still exits weak trapping sites around screw dislocation core, with binding energy being -0.10 eV. Therefore, in light of our calculated binding energies of H, both edge and screw dislocations in bcc Fe also have the capability to attract H atoms.

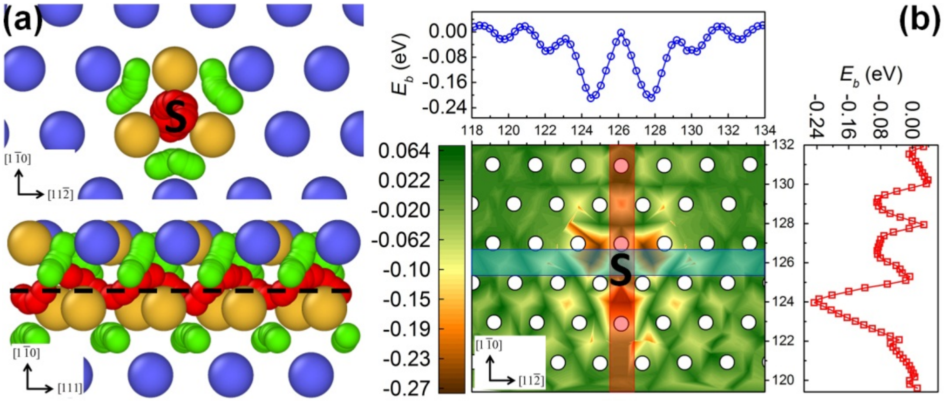

Figure 7.5. (a) Atomic configuration of screw dislocation and H trapping site in bcc Fe. The big blue balls are bcc bulk-like Fe atoms. The big brown balls are non bulk-like Fe atoms at dislocation core. The small balls (red and green color) are H trapping sites at core region. (b) Binding energy map of H at screw dislocation in bcc Fe. Top subfigure in (b) is the binding energy as a function of H position along glide direction, as demonstrated by blue strip in the map. Right subfigure in (b) is the binding energy profile of H along the direction normal to dislocation slip direction, as illustrated by red strip in the map.

7.4.2 k-ART simulations

In order to assess the kinetics of H in the vicinity of dislocations over long timescale, the diffusion properties of H atom in various dislocation core structure in fcc Ni and bcc Fe are comprehensively studied.

- *Kinetics of H at dislocations in fcc Ni*

As for edge dislocation in fcc Ni, the binding energy landscape, square displacement (*SD*) and diffusion barrier of each selected event at 300 K during k-ART simulations are shown in Figure 7.6a. The timescale in our simulation can be expanded to 250 microseconds (μs), which is much longer than traditional MD simulations. As can be seen in the top panel of Figure 7.6a, the binding energy landscape produced in our study mainly ranged from 0 eV to -0.17 eV for H atom at edge dislocation. This result agrees well with our previous MS simulations, indicative of the validation of k-ART simulations. This binding energy spectrum (i.e., 0 eV~ -0.17 eV) corresponds to the fact that H atom occupies the stable trapping site at edge dislocation core. However, we also discover some states have higher binding energies. These high energy values presumably correspond to the unstable state or transition state of H atom during diffusion process. The *SD* profile is also illustrated in Figure 7.6a where the *SD* in the bottom panel of Figure 7.6a does not increase simultaneously with the increase of simulation time. Instead, the *SD* shows periodicity in which the *SD* initially goes up and then decreases as the time increases from 0 to 150 μs. After that, it repeats again from 150 to 250 μs. In addition, the barrier of each selected hopping event of H atom is illustrated in the bottom panel of Figure 7.6a as well. According to our simulated *SD*, it is apparent to see that H atom does not effectively transport within edge dislocation core. In order to better understand this case, the trajectory of H within edge dislocation core is plotted in Figure 7.6b. H atom only moves back and forth within specific pathways around Shockley partial core (marked by red line in Figure 7.6b) and is not able to move forward along dislocation line direction freely. In addition, it is difficult for H atom hopping across two paralleled pathways and H atom only diffuses along pathway for short range, which cannot contribute to long range pipe diffusion process.

Aside from edge dislocation, we turn to the characterization of kinetics of H at screw dislocation. In Figure 7.7, binding energy of H, the *SD* profile and migration energy as a function of simulation time are both plotted. The binding energies are mainly ranged from 0 to -0.1eV(Figure 7.7a), which is in agreement well with previous MS simulations. The *SD* profile in Figure 7.7a shows oscillation without effective increase as simulation time goes on, suggesting that H atom is restrained within screw dislocation core region. It is noteworthy that the migration barriers are mainly ranged from 0.04~0.29 eV, being lower than the barrier of H hopping in Ni bulk lattice (0.4 eV). From energetic aspect, it is generally assumed that H should fast diffuse with in dislocation core region due to the relative low migration barriers. However, we clearly see that the *SD* doesn’t increase over simulation time. As for clarifying this unusual scenario, we plot the trajectory of H atom migrating in screw dislocation, as illustrated in Figure 7.7b. We can definitely see that H transport within short range, which is similar to the case of edge dislocation. That means H cannot fast diffuse along dislocation line direction. Instead, H atoms are evidently trapped within dislocation core region.

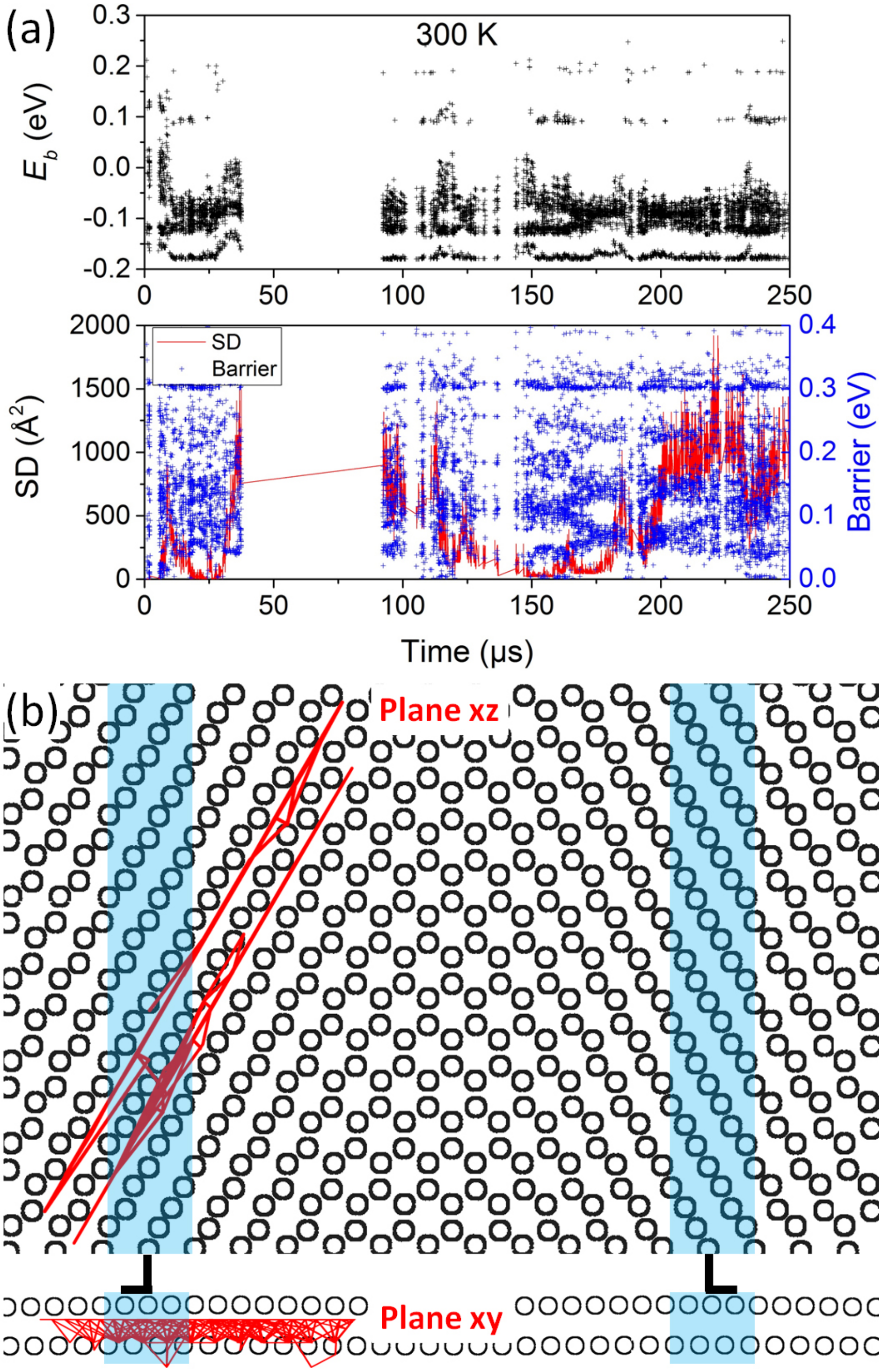

Figure 7.6. (a) Top panel: binding energies of H at edge dislocation. Bottom panel: The *SD* and migration barriers as a function of simulation time. (b) H trajectory at edge dislocation. Red line represents H trajectory. Blue strip illustrates partial core region. Open black circles are host Ni atoms.

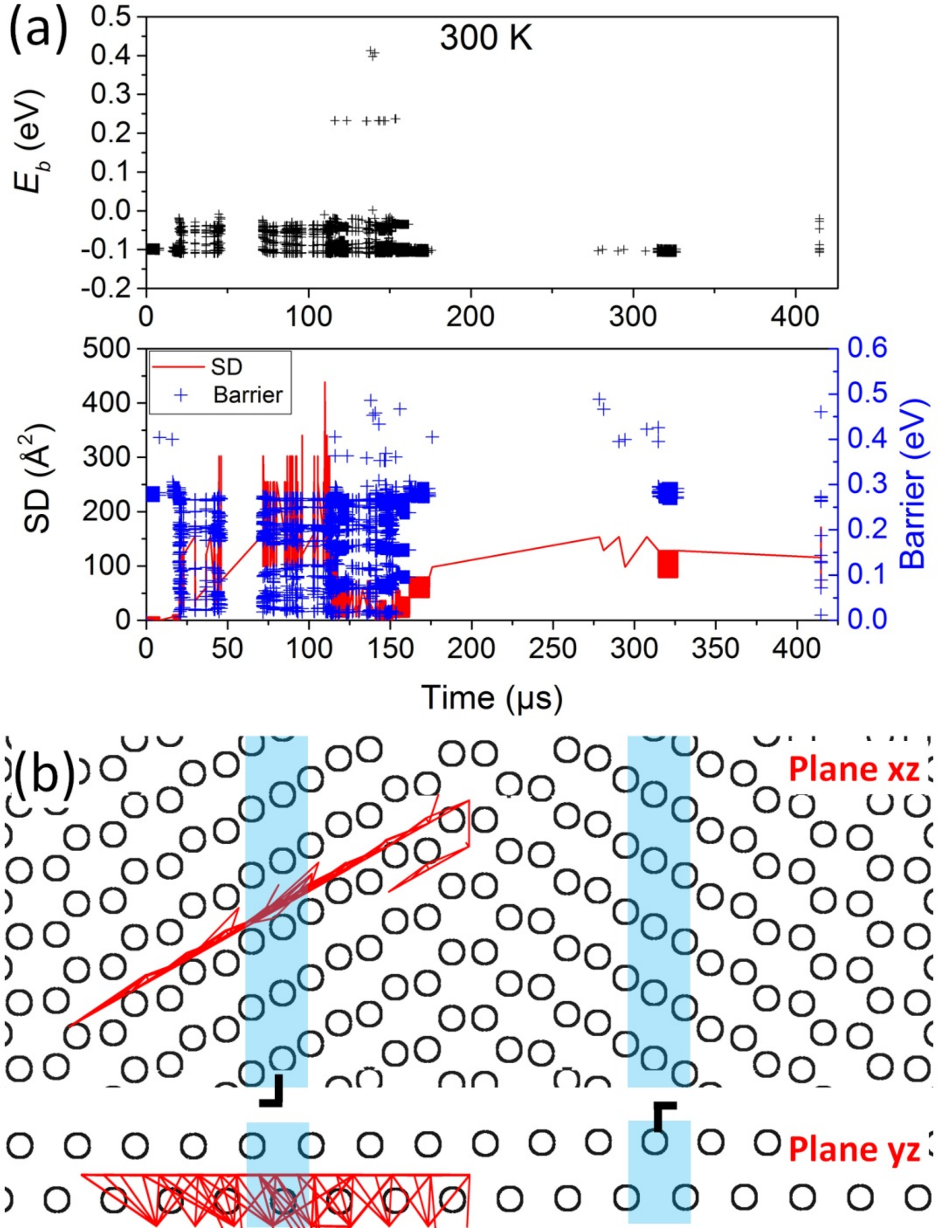

Figure 7.7. (a) Top panel: binding energies of H at screw dislocation. Bottom panel: The *SD* and migration barriers as a function of time. (b) H trajectory in screw dislocation. Red line represents H trajectory. Blue region illustrates partial core. Open black circles are host Ni atoms.

- *Kinetics of H at dislocations in bcc Fe*

Having successfully clarified that H atom will be blocked in the region of dislocation core region rather than fast diffusion over long timescale in k-ART simulations for fcc Ni system. In this section, we examine the kinetics of H at edge dislocation of bcc Fe. As demonstrated in Figure 7.8, multiple various states with different binding energies are detected and the lowest binding energy is approximately -0.31 eV. This value is very close to the calculated result in our MS simulations and suggests the validation of k-ART simulation in bcc Fe system with the selected EAM potential. The *SD* profile has been described in the bottom subfigure of Figure 7.8a. We can clearly note that the *SD* keeps almost constant without significant increase as simulation time goes on, meaning that H atom is also blocked in the region of edge dislocation core of bcc Fe. H atom only transports in specific paths along dislocation line direction within short range and cannot move forward freely in long distance, which can be reflected by the H trajectory in Figure 7.8b.

Considering the kinetics of a single H atom at screw dislocation, we first ascertained that H atom is deeply trapped at the screw dislocation core region, with the lowest binding energy being -0.31 eV, as shown in the top panel of Figure 7.9a. In addition, the *SD* information and migration barriers during k-ART simulation are described in the bottom panel of Figure 7.9a. The *SD* profile has the characterization that it first keeps oscillation and then suddenly jumps to a high value as simulation time increases. If we look at the migration barriers in the bottom figure of Figure 7.9a, we find that the oscillation regions in the *SD* profile have relative low barriers (0.01~0.1 eV). However, the sudden jumping points in *SD* profile have large barriers (0.29~0.36 eV). Interestingly, the H trajectory at screw dislocation indicates strong constraint to the vicinity of dislocation core due to strong trapping tendency. This constraint is directly reflected by the oscillation in *SD* profile without apparent increase over simulation time.

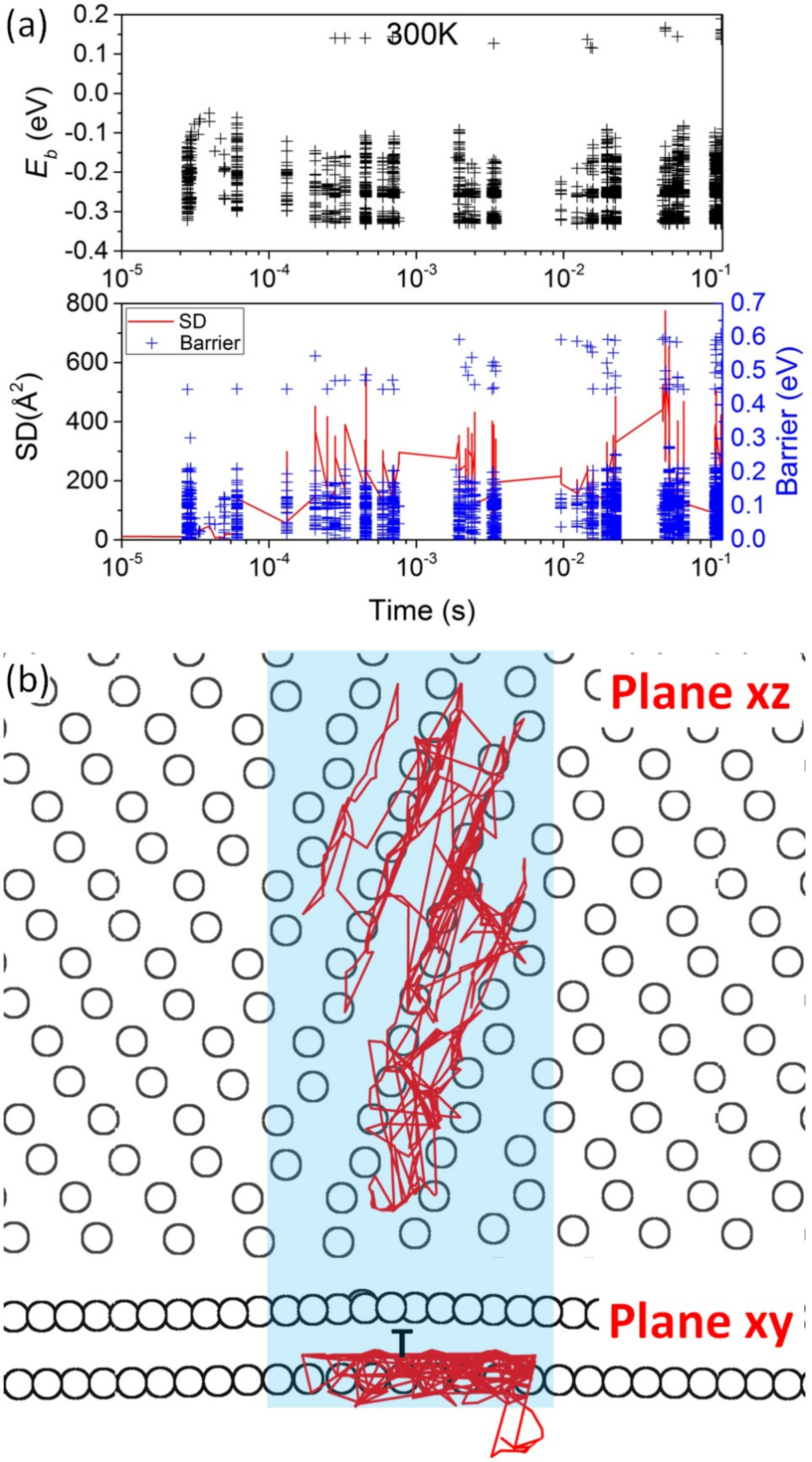

Figure 7.8. (a) Top figure: binding energies of H at edge dislocation. Bottom figure: The *SD* and migration barriers as a function of simulation time. (b) H trajectory at edge dislocation of bcc Fe. Red line represents H trajectory. Blue region illustrates edge dislocation core. Open black circles are host Fe atoms.

In addition, we also find that H atom can jump out of deep trapping regions and move along dislocation line direction with very low probability, as indicated in Figure 7.9b. This hopping state corresponds to the sudden jumping point in *SD* profile with relative high migration barriers.

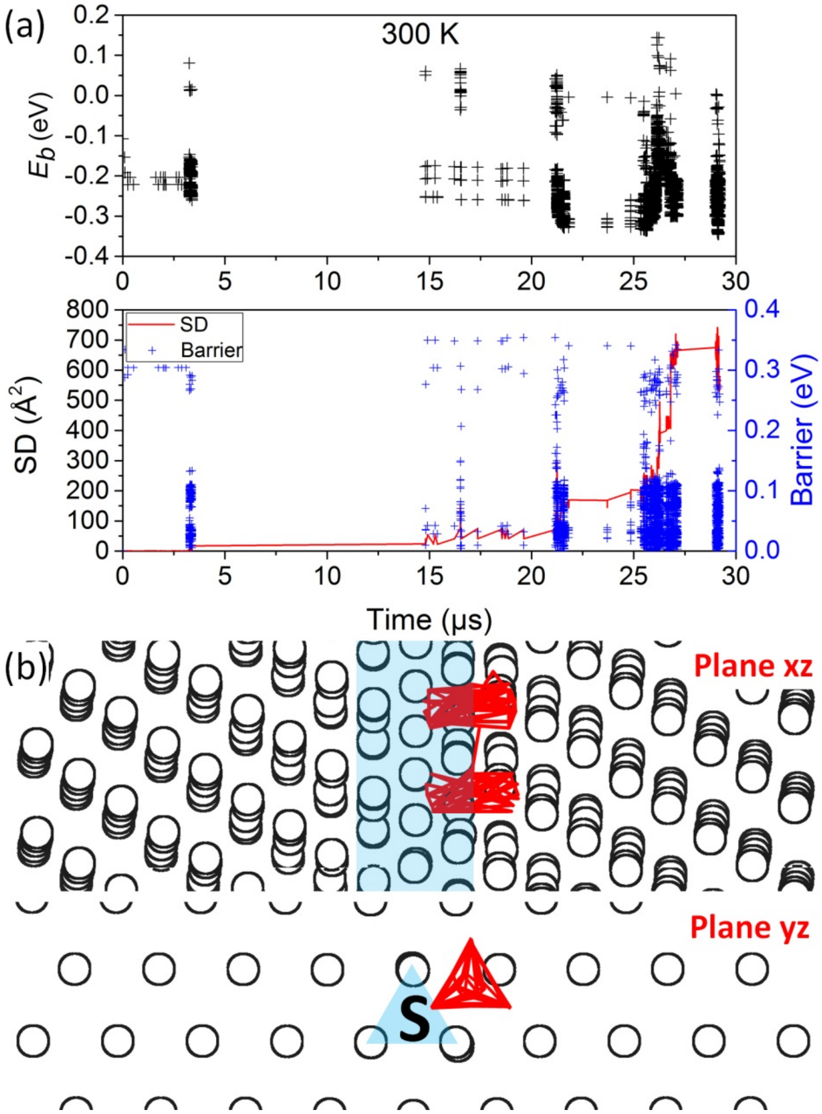

Figure 7.9. (a) Top figure: binding energies of H at screw dislocation. Bottom figure: The *SD* and migration barriers as a function of simulation time. (b) H trajectory at screw dislocation. Red line represents H trajectory. Blue region illustrates screw dislocation core. Open black circles are host Fe atoms.

7.4.3 NEB calculations and identification of migration paths

In previous section, we have successfully established the picture of H transportation at dislocations for fcc Ni and bcc Fe systems over long timescale. To further reveal the atomic mechanisms of H diffusion at dislocations, we complementally performed NEB calculations for various possible states and identified the H migration paths in this part.

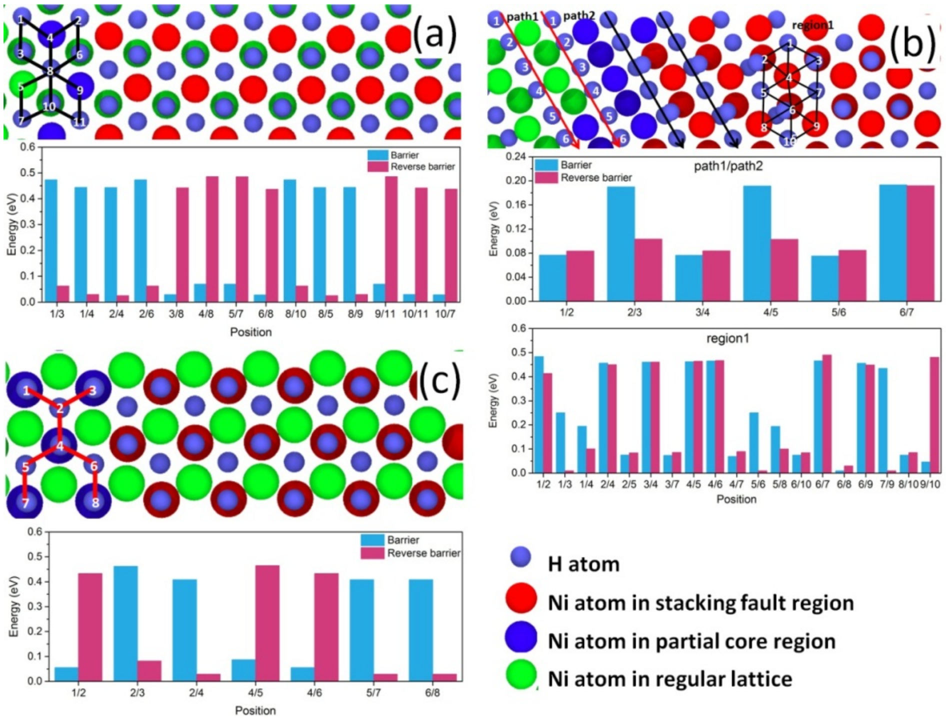

Figure 7.10. H trapping site, possible migration path and migration barrier for H in different layer of edge dislocation in fcc Ni. (a) Bottom layer (b) Middle layer and (c) Top layer. The small blue balls are H trapping sites. Big red balls show stacking fault region. Big blue balls indicate Shockley partial core region. Big green balls show Ni atoms with fcc Ni lattice.

- *Edge and screw dislocation in fcc Ni*

With respect to edge dislocation in fcc Ni, the migration barriers obtained from NEB calculations are presented in Figure 7.10 in detail. Specifically, there are three categories of barriers for H, which is depended on H trapping positions at dislocation (namely, top, middle and bottom layer of edge dislocation defined previously). It is worth noting that the migration barriers in top (Figure 7.10a) and bottom layers (Figure 7.10c) are larger than that in fcc bulk Ni lattice (~0.4 eV), suggesting no pathways with low energy barriers in top and bottom layers. It is also pointed out with emphasis that the *x* axis of bar chart in Figure 7.10 means the hopping direction. For instance, in the bottom subfigure of Figure 7.10a, “1/2” in *x* axis means H migration barrier from position “1” to position “2”, and the reverse barrier corresponds to the hopping state from position “2” to position “1”. Without other mention, the same criterion would be used in the following parts. Now we turn to look at the middle layer of edge dislocation. As can be seen in the top panel of Figure 7.10b, several different paths and regions are defined on the basis of the diversity of local atomic structure in middle layer. Taking two representative pathways, namely, “path1” and “path2” at Shockley partial core and “region1” in stacking fault region for consideration, we find path1 and path2 have low migration barriers, as shown in the middle panel of Figure 7.10b. However, there are several positions owing higher migration barriers in comparison with bulk lattice, as indicated in the bottom panel of Figure 7.10b. For instance, “2/4”, “4/6” and “6/9” have very high barriers, with value being 0.48 eV approximately.

As for screw dislocation in fcc Ni, we find that only middle layer exists pathway with low migration barriers, as shown in Figure 7.11. In the pathway marked in Figure 7.11, we discover that some positions (i.e., “2/3”, “4/5”, “6/7” and “8/9”) have extremely low barrier (0.05 eV) compared with other positions (0.24 eV). That means H atom will be trapped in these positions with low barriers and these positions have no contribution to long range diffusion. This fact can be also confirmed by the oscillation in the *SD* profile in Figure 7.7. Therefore, although there are some paths containing continuous positions with low migration barriers, we believe H cannot effectively move in long range due to the “*short circuit*” oscillation can strongly trap H atom in these positions.

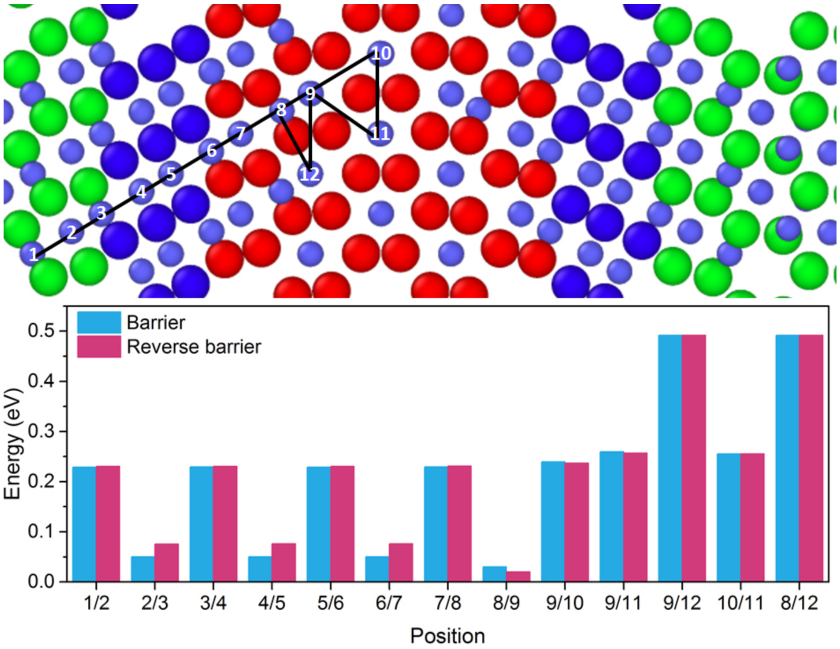

Figure 7.11. H trapping site, possible migration path and migration barrier for H in the middle layer of screw dislocation in fcc Ni. The small blue balls are H trapping sites. Big

red balls show stacking fault region. Big blue balls indicate Shockley partial core region. Big green balls show Ni atoms with regular fcc crystal structure.

- *Edge and screw dislocation in bcc Fe*

In this section, we turn to investigate minimum energy path for H diffusion in edge and screw dislocation in bcc Fe system. In terms of edge dislocation in bcc Fe, we have defined two different layers, i.e., middle and bottom layer. H occupying sites and migration barriers for H in middle layer are shown in Figure 7.12. Three representative paths, "path1", "path2" and "path3" can be clearly seen at the bottom right corner in Figure 7.12.

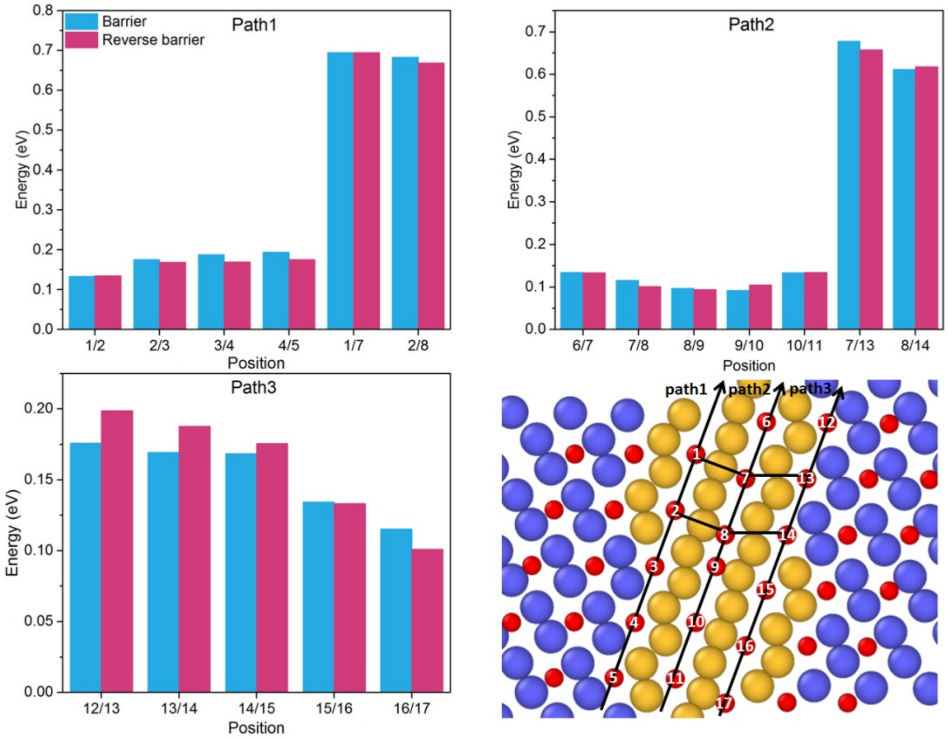

Figure 7.12. H occupying site, possible migration path and migration barrier in the middle layer of edge dislocation in bcc Fe. The small red balls are H occupying sites. Big brown balls show edge dislocation core region and big blue balls indicate Fe atoms with regular bcc crystal structure.

The migration barriers for H transporting *along* the pathway (e.g. “1/2”, “2/3” and “3/4” in “path1”) are lower than the barriers for H hopping *between* two parallel pathways (e.g. “1/7” and “7/13”). However, these barriers at dislocation are still higher than that in bcc Fe bulk lattice (~0.04 eV). When it comes to the bottom layer of edge dislocation, most positions have relative higher migration barriers except for several positions with lower values (e.g., “7/8”, “8/9” etc. in “path2”), as seen in Figure 7.13. For hopping between two parallel paths, it is very difficult for H freely transporting between two paths due to the higher barrier (e.g., 0.29 eV for “2/7”). Therefore, according to our calculations, edge dislocation in bcc Fe can strongly retard H diffusion rather than enhance diffusion.

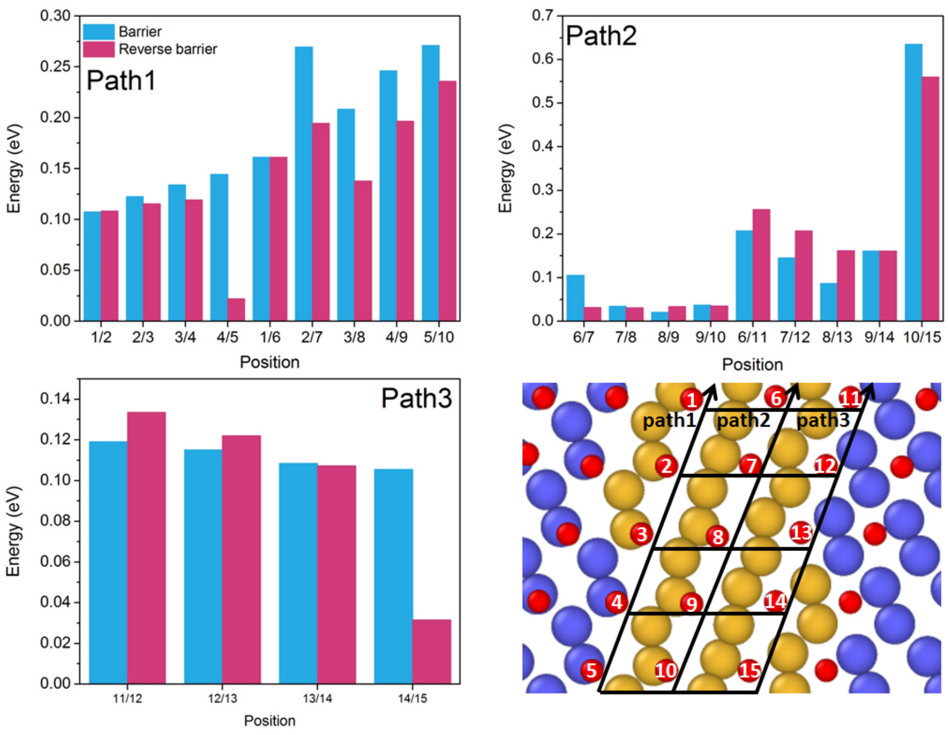

Figure 7.13. H trapping site, possible migration path and migration barrier in the bottom layer of edge dislocation in bcc Fe. The small red balls are H occupying sites. Big brown

balls show edge dislocation core region and big blue balls indicate Fe atoms with bcc Fe lattice.

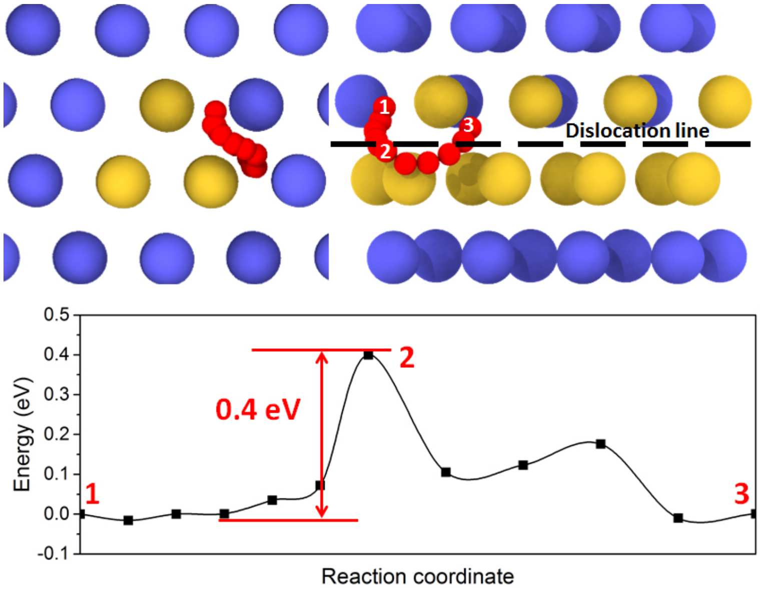

Figure 7.14. Migration barriers of H diffusion along dislocation line direction near screw core. The big brown balls show screw dislocation core and the big blue balls represent Fe atoms with bcc crystal structure, the small red balls represent H position in migration path.

With regard to screw dislocation in bcc Fe, we only involve the trapping sites near dislocation core as we confirmed that H in the core region is not energetically favorable and it can jump from the core region to the nearest trapping sites. The minimum energy path and migration barriers through the trapping sites along dislocation line direction are shown in Figure 7.14. It is evident that the migration barrier is much higher than that in bcc bulk lattice (i.e., 0.4 eV near screw dislocation core), as indicated in Figure 7.14. Therefore, our results ascertain that screw dislocation will retard H atom to transport along dislocation line in bcc Fe.

The joint analysis of H migration along edge and screw dislocations in fcc Ni and bcc Fe by means of long timescale k-ART simulations and NEB calculations, demonstrate that there are no pathways for H pipe diffusion along dislocation lines. As explained previously, even though low barrier states exist in the vicinity of dislocations, we find that H positions with low barriers are not successively linked. Instead, the paths with low barrier at edge dislocation in fcc Ni are truncated at the border between partial core region and stacking fault region as well as between partial core region and bulk lattice region. For further clarification, the schematic illustration of H trapping sites and migration barrier profiles for edge and screw dislocations in fcc Ni are presented in Figure 7.15. Regarding edge dislocation, we can clearly note that the paths with low barriers are terminated at the borders we defined previously due to the high migration barrier for H occupying at borders, indicating that H can only move back and forth along the path with low barriers between two borders. This short range fast diffusion cannot attribute to long range pipe diffusion over long timescale.

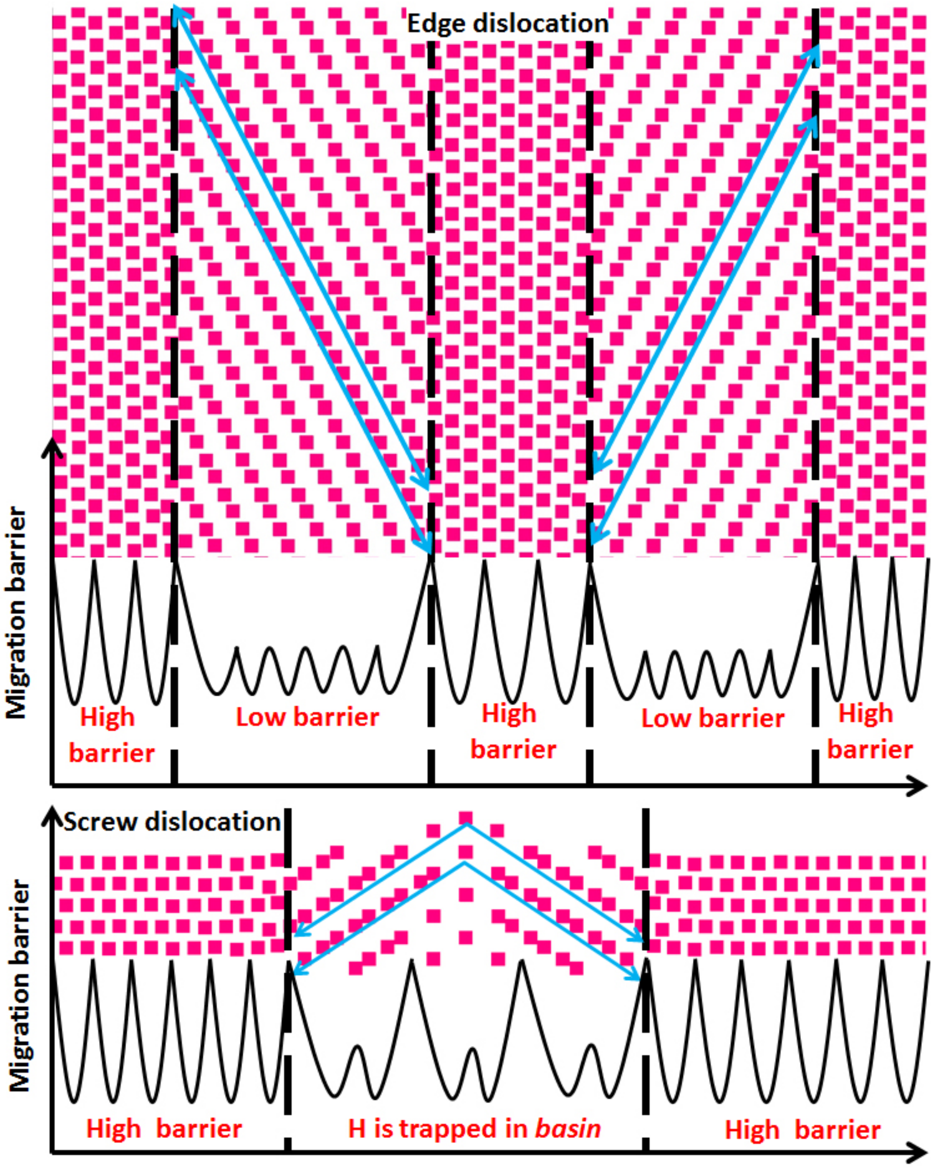

Figure 7.15. Possible H trapping sites in the middle layer of edge and screw dislocation and schematic illustration of migration barriers in fcc Ni. The solid red squares are H trapping sites, the black dash lines show the borders. The blue lines with arrows show the pathways with low migration barriers.

In addition, as for screw dislocation in fcc Ni, the low barrier states are located at *basin* in which H atoms are strongly trapped and difficult to escape the *basin*, as shown in Figure 7.15. Hence, H atoms can only oscillate within the *basin* and no fast pipe diffusion can occur. Contrastively, H migration at edge and screw dislocations in bcc Fe is different from the case in fcc Ni. That is to say, we find that the migration barriers of H at dislocations are apparently larger than that in bcc bulk Fe lattice. So H atom can only be trapped and dislocations hinder H transportation.

7.5 Conclusions

In summary, we have comprehensively investigated the kinetics of H in the proximity of edge and screw dislocations in both fcc Ni and bcc Fe systems. By combining long timescale k-ART simulations with NEB calculations, we discovered fast pipe diffusion in fcc Ni and bcc Fe cannot occur over long timescale. Our results for fcc Ni system is in contradiction with Tang's work [18]. In Tang's work, the author only examined the migration barriers of very limited two short paths within Shockley partial core, which is insufficient to give the final conclusion that pipe diffusion can occur in fcc Ni. Similarly, as for fcc Pd system, Schiavone et al. [19] only scrutinized very limited positions near partial core region without considering the migration energy profiles of the whole region of dislocation. As interpreted in our study, the pathways with lower barriers are not continuous for H to move freely along dislocation line direction due to the hindrance at borders. Therefore, despite of low barriers at dislocation, H atoms are still blocked and only fast diffuse in short range. When it comes to bcc Fe, no pathways with low barriers appear in the region of dislocation and H atoms are blocked at dislocation without pipe diffusion. Our results are in well agreement with other theoretical works where slow diffusion of H at both edge and screw dislocation happens in bcc Fe [23]. In addition, recent work regarding carbon diffusion in screw dislocation in bcc Fe also revealed that carbon fast pipe diffusion is unlikely, which can support our results indirectly [31]. Hence, the present study clarified H pipe diffusion in fcc Ni and bcc Fe at atomic scale and can further provide some important hints for investigating kinetics of other interstitial impurities in microstructural heterogeneities.

7.6 References

[1] Johnson WH. On Some Remarkable Changes Produced in Iron and Steel by the Action of Hydrogen and Acids Proceedings of the Royal Society of London 1874;23:12.
[2] Pfeil L. The effect of occluded hydrogen on the tensile strength of iron. Proceedings of the Royal Society of London Series A, Containing Papers of a Mathematical and Physical Character 1926;112:182-95.
[3] Ainslie NG, Hoffman RE, Seybolt AU. Sulfur segregation at α-iron grain boundaries—I. Acta Metallurgica 1960;8:523-7.
[4] Troiano AR. The role of hydrogen and other interstitials in the mechanical behavior of metals. Trans ASM 1960;52:26.
[5] Hohenberg P, Kohn W. Inhomogeneous electron gas. Physical review 1964;136:B864.
[6] Rogers H. Hydrogen Embrittlement of Metals: Atomic hydrogen from a variety of sources reduces the ductility of many metals. Science 1968;159:1057-64.
[7] Oriani RA. Hydrogen Embrittlement of Steels. Annual review of materials research 1978;8:30.
[8] Hirth JP. Effects of hydrogen on the properties of iron and steel. MTA 1980;11:861-90.
[9] Tabata T, Birnbaum HK. Direct observations of the effect of hydrogen on the behavior of dislocations in iron. Scripta Metallurgica 1983;17:947-50.
[10] Baskes MI, Vitek V. Trapping of hydrogen and helium at grain boundaries in nickel: An atomistic study. MTA 1985;16:1625-31.
[11] Mütschele T, Kirchheim R. Segregation and diffusion of hydrogen in grain boundaries of palladium. Scripta Metallurgica 1987;21:135-40.

[12] Myers SM, Baskes M, Birnbaum H, Corbett JW, DeLeo G, Estreicher S, et al. Hydrogen interactions with defects in crystalline solids. Reviews of Modern Physics 1992;64:559.

[13] Itoh G, Koyama K, Kanno M. Evidence for the transport of impurity hydrogen with gliding dislocations in aluminum. Scripta Materialia 1996;35:695-8.

[14] Kirchheim R. Interaction of hydrogen with dislocation in palladium—I. activity and diffusivity and their phenomenological interpretation. In: Hirth JP, editor. Perspectives in Hydrogen in Metals: Pergamon; 1986. p. 355-63.

[15] Tien J, Thompson AW, Bernstein IM, Richards RJ. Hydrogen transport by dislocations. MTA 1976;7:821-9.

[16] Albrecht J, Bernstein IM, Thompson AW. Evidence for Dislocation Transport of Hydrogen in Aluminum. MTA 1982;13:811-20.

[17] Heuser BJ, Trinkle DR, Jalarvo N, Serio J, Schiavone EJ, Mamontov E, et al. Direct Measurement of Hydrogen Dislocation Pipe Diffusion in Deformed Polycrystalline Pd Using Quasielastic Neutron Scattering. Physical review letters 2014;113:025504.

[18] Tang Y, El-Awady JA. Atomistic simulations of the interactions of hydrogen with dislocations in fcc metals. Physical Review B 2012;86:174102.

[19] Schiavone EJ, Trinkle DR. Ab initio modeling of quasielastic neutron scattering of hydrogen pipe diffusion in palladium. Physical Review B 2016;94:054114.

[20] Ogawa H. Atomistic simulation of hydrogen dynamics near dislocations in vanadium hydrides. Journal of Alloys and Compounds 2015;645:S205-S8.

[21] Bombac D, Katzarov I, Pashov D, Paxton A. Theoretical evaluation of the role of crystal defects on local equilibrium and effective diffusivity of hydrogen in iron. Materials Science and Technology 2017;33:1505-14.

[22] Iwaoka H, Arita M, Horita Z. Hydrogen diffusion in ultrafine-grained palladium: Roles of dislocations and grain boundaries. Acta Materialia 2016;107:168-77.

[23] Kimizuka H, Ogata S. Slow diffusion of hydrogen at a screw dislocation core in α-iron. Physical Review B 2011;84:024116.

[24] Hirth JP, Lothe J. Theory of dislocations. 1982.

[25] Angelo JE, Moody NR, Baskes MI. Trapping of hydrogen to lattice defects in nickel. Modelling and Simulation in Materials Science and Engineering 1995;3:289.

[26] Ramasubramaniam A, Itakura M, Carter EA. Interatomic potentials for hydrogen in α–iron based on density functional theory. Physical Review B 2009;79:174101.

[27] El-Mellouhi F, Mousseau N, Lewis LJ. Kinetic activation-relaxation technique: An off-lattice self-learning kinetic Monte Carlo algorithm. Physical Review B 2008;78:153202.

[28] Trochet M, Béland LK, Joly J-F, Brommer P, Mousseau N. Diffusion of point defects in crystalline silicon using the kinetic activation-relaxation technique method. Physical Review B 2015;91:224106.

[29] Plimpton S. Fast parallel algorithms for short-range molecular dynamics. Journal of computational physics 1995;117:1-19.

[30] Henkelman G, Jónsson H. Improved tangent estimate in the nudged elastic band method for finding minimum energy paths and saddle points. The Journal of chemical physics 2000;113:9978-85.

[31] Nematollahi GA, Grabowski B, Raabe D, Neugebauer J. Multiscale description of carbon-supersaturated ferrite in severely drawn pearlitic wires. Acta Materialia 2016;111:321-34.

Chapter 8: Conclusions

8.1 Final conclusions

The main goal of this PhD dissertation is to provide key atomistic insights toward understanding mutual interactions between hydrogen and microstructures in metals, with particular focus on two defect types, grain boundary and dislocation. Employing state-of-the-art computational techniques, comprehensive studies were performed to reveal the structure-property relationships prescribing thermodynamics and kinetics of hydrogen at dislocations and grain boundaries. The main conclusions are summarized as follows:

- The energetics of hydrogen and segregation tendency at various types of grain boundaries in Ni were systematically studied. It was found the segregation tendency is strongly dependent on the local atomic arrangements of grain boundaries, in which hydrogen induced local atomic distortion at grain boundary plays the dominant role in determining hydrogen trapping. Meanwhile, one chemomechanical model was proposed to quantitatively assess the influence of local distortion caused by hydrogen on segregation tendency, indicating hydrogen segregation energy can be predicted by particular volumetric distortion of structural units identified at grain boundaries.
- The kinetics of hydrogen at various types of grain boundaries in Ni were carefully examined. Similar to hydrogen segregation, hydrogen diffusion behaviors along grain boundaries are also evidently impacted by local atomic configurations of grain

boundaries. We noted grain boundaries play the dual role in hydrogen diffusion (i.e., fast diffusion or retardation), depending on grain boundary structure and grain boundary angle. For grain boundary with high boundary angle, fast diffusion occurs while trapping/blocking takes place for grain boundary with low boundary angle. Meanwhile, a micromechanical model was developed to successfully predict this boundary angle-dependent diffusion behaviors, suggesting the transition between fast diffusion and trapping is controlled by the dislocation arrays existed in grain boundary.

- The influences of hydrogen on dislocation nucleation in Ni and Pd were studied in detail. Our results demonstrated hydrogen atoms can facilitate dislocation nucleation (reflected by the reduction of *pop-in* load in nanoindentation), which derives from the local atomic distortion (i.e., lattice dilation) introduced by hydrogen. However, this effect of hydrogen on promoting the onset of plasticity is limited and is insensitive to lattice orientation and the type of metal.
- The energetics and kinetics of hydrogen at dislocations in metals were systematically investigated. It was found hydrogen atoms are energetically preferable at Shockley partial core region for both edge and screw dislocation. For kinetics of hydrogen in the proximity of dislocations, Long time Kinetic Monte Carlo simulations suggested hydrogen atoms are strongly constrained within dislocation core region and no pipe

diffusion occurs for both tested metal system. Complement NEB calculations further confirm there is no continuous pathway with low migration barriers for hydrogen.

8.2 Contributions to original knowledge

The contributions to original knowledge established in this thesis are summarized as follows:

- One novel algorithm on the basis of space tessellation was first developed to effectively characterize grain boundary structure by polyhedral structure units.
- The correlation between hydrogen segregation and local lattice distortion at grain boundary was discovered. A novel physics-based model was developed, which, for the first time, enable the predictive assessment of hydrogen segregation energies at grain boundaries as functions of the local volumetric distortion.
- For the first time, the dual role of grain boundaries in hydrogen diffusion, namely fast diffusion or trapping, was demonstrated using systematic atomistic simulations. The explicit dependence of hydrogen diffusion on local atomic arrangements and tilt angles of grain boundaries was revealed. Hydrogen diffusion behaviors at grain boundaries can be successfully predicted by one micromechanical model, which was first developed in this study.
- The effect of hydrogen on reducing the threshold of dislocation nucleation was found to be only correlated to lattice dilation induced by hydrogen. Meanwhile, we

also noted the presence of hydrogen has no direct effects on dislocation nucleation or subsequent multiplication and hardening, for the first time.

- For the first time, second-long hydrogen diffusion along edge and screw dislocation lines in structural metals (i.e., fcc Ni and bcc Fe) were simulated, confirming that pipe diffusion of hydrogen along dislocation lines is not occurring.

8.3 Future work

Although this thesis sheds some lights on better understanding the interplays of hydrogen with microstructural heterogeneities in metals at the atomic scale, there still exist many unsolved issues and unexplored area in hydrogen embrittlement due to its complexity and diversity. Some interesting topics excluded in this thesis are list as follows:

- *Dislocation-Grain boundary interaction with hydrogen*: The effect of hydrogen on dislocations interacting with grain boundaries plays the vital role in plasticity of metals under hydrogen charging, which need further clarification.
- *Interaction of hydrogen with precipitations*: Aside from grain boundaries and dislocations, precipitations and interfaces are of particular interest. The complicated trapping state of hydrogen in precipitations and corresponding interface between matrix and precipitation need further investigations.
- *Kinetics of hydrogen in precipitations*: Convincing experimental evidence suggested hydrogen atoms can be trapped within precipitations and carbides. However, current

theoretical calculations indicated it is impossible for hydrogen jumping into the precipitations due to the extremely high migration barriers. Therefore, there must be some other mechanisms regarding this migration process of hydrogen, which necessities further studies.

- *Effect of alloying elements on energetics and kinetics of hydrogen at grain boundaries*: Another important aspect that is not considered in this thesis is alloying element on hydrogen segregation and diffusion at grain boundaries. However, few studies have focused on the complicated interactions between hydrogen and alloying elements at grain boundaries.